HUGO ANDERSSON DANTAS MEDEIROS

STUDY OF THE MULTIPHASE EQUILIBRIA OF RESERVOIR FLUIDS
UNDER HIGH-PRESSURE AND HIGH-TEMPERATURE CONDITIONS

FORTALEZA (BRAZIL) / PAU (FRANCE)

2024

HUGO ANDERSSON DANTAS MEDEIROS

**STUDY OF THE MULTIPHASE EQUILIBRIA OF RESERVOIR FLUIDS
UNDER HIGH PRESSURE AND HIGH TEMPERATURE CONDITIONS**

Thesis submitted to the Graduate Program in Chemical Engineering at the Federal University of Ceará (UFC), in collaboration with the Université de Pau et des Pays de l'Adour (UPPA) as a partial requirement for obtaining a Doctorate in Chemical Engineering, in the area of concentration of Chemical and Biochemical Processes from UFC, and a Doctorate in Petroleum Engineering from UPPA.

Advisors:
Prof. Dr. Hosiberto Batista de Sant'Ana.
Prof. Dr. Jean-Luc Daridon.

FORTALEZA (BRAZIL) / PAU (FRANCE)

2024

HUGO ANDERSSON DANTAS MEDEIROS

STUDY OF THE MULTIPHASE EQUILIBRIA OF RESERVOIR FLUIDS UNDER HIGH PRESSURE AND HIGH TEMPERATURE CONDITIONS

Thesis presented to the Post-Graduation Program in Chemical Engineering at the Federal University of Ceará, in cotutelle with Université de Pau et des Pays de l'Adour as a partial requirement to obtain the degree of Doctor in Science.

Advisors:
Prof. Dr. Hosiberto Batista de Sant'Ana.
Prof. Dr. Jean-Luc Daridon

Date : 27/05/2025

EXAMINATION BOARD

Prof. Dr. Hosiberto Batista de Sant'Ana (Advisor)

Universidade Federal do Ceará - UFC

Prof. Dr. Jean-Luc Daridon (Advisor)

Université de Pau et des Pays de l'Adour - UPPA

Prof. Dr. Jean-Charles de Hemptinne (Reviewer)

Institut Français du Pétrole et des Energies Nouvelles – IFPEN

Prof. Dr. Papa Matar Ndiaye (Reviewer)

Universidade Federal do Rio de Janeiro – UFRJ

Prof. Dr. Guillaume Galliero (Jury)

Université de Pau et des Pays de l'Adour - UPPA

Dr. Felipe Mauro Rena Cardoso (Jury)

Petróleo Brasileiro S.A. - PETROBRAS

Dedicated to my family, especially to my grandmother, Hozana Dantas Cortez Pereira (*in memorian)*

ACKNOWLEDGMENTS

ABSTRACT

Phase behavior study is crucial for designing and optimizing separation processes, especially for industries that deal with high pressure, such as the oil industry. Due to the multicomponent nature of crude oil, the experimentally observed phase equilibrium goes beyond the liquid-vapor biphasic equilibrium commonly found in simpler systems. Reservoir fluids produced from Brazil's pre-salt fields exhibit a high gas content, particularly carbon dioxide. This factor, combined with the high opacity of crude oil, poses significant challenges to the experimental study of the phase behavior of these fluids. Recently, some studies have reported the occurrence of immiscibility between liquid phases over a wide range of pressures and temperatures, particularly at temperatures well above the critical temperature of carbon dioxide. This liquid-liquid equilibrium exhibits specific characteristics that make it difficult to precisely detect the conditions under which the transition occurs, mainly due to the high opacity of the fluid and the low-density contrast between the liquid phases. This Thesis studied the phase behavior of various pre-salt crude oil samples recombined with carbon dioxide, methane, and mixtures of these two gases. The investigated crude oil samples differ primarily in terms of their S.A.R.A. distributions. To advance this research, indirect techniques, such as light scattering, p-V, and Y-factor curves, were used alongside direct observation techniques of the investigated fluid. A direct observation technique based on an infrared camera was applied due to its ability to investigate opaque fluids. The results demonstrated that the occurrence of a liquid-liquid transition is not exclusive to a single pre-salt crude oil sample. However, this type of transition was only observed in mixtures with a high gas content ($z_{gas} > 70$ mol %) and were not restricted to the type of gas added. Furthermore, in some cases, the liquid-liquid equilibrium evolved into a liquid-liquid-vapor three-phase equilibrium, even under atypical pressure and temperature conditions. The results suggest that a liquid-liquid equilibrium is related to the high asymmetry of the system, particularly between the excess gas and the heavier fraction of the crude oil, such as asphaltenes. The modeling supports the hypothesis that the formation of the second liquid phase results from the limited solubility of the heavy fraction of the crude oil in systems with high gas content. Furthermore, the thermodynamic modeling approach indicates that the non-segregative nature between the liquid phases is due to the close density values of the phases. Finally, a synthetic system was investigated to reproduce the liquid-liquid equilibrium observed in pre-salt fluids.

However, the chosen system could not produce the atypical behavior of the pre-salt fluids, probably due to the occurrence of a solid-liquid locus that overlapped a possible liquid-liquid locus in the phase diagram.

RESUMÉ

L'étude du comportement des phases des fluides est une étape cruciale dans la conception et l'optimisation des processus de séparation, en particulier pour les industries opérant à haute pression, comme l'industrie pétrolière. En raison de la nature multi-constituants des effluents pétroliers, les équilibres de phase observés expérimentalement dans les fluides de réservoir dépassent le simple comportement biphasique liquide-vapeur communément rencontré à l'équilibre dans les systèmes plus simples. En particulier, les fluides de réservoir produits dans les champs pré-salifères brésiliens présentent une teneur élevée en gaz, notamment en dioxyde de carbone, qui génère des comportements de phase complexes. Ce facteur, associé à la grande opacité de ces huiles brutes, pose d'importants défis pour l'étude expérimentale du comportement des phases de ces fluides. Récemment, certaines études ont rapporté l'existence d'une immiscibilité entre phases liquides sur une large plage de pression et de température, en particulier à des températures bien supérieures à la température critique du dioxyde de carbone. Ces équilibres liquide-liquide, liquide-liquide-vapeur ou parfois même liquide-liquide-liquide présentent certaines caractéristiques qui compliquent la détection précise des conditions de transition, principalement en raison du faible contraste de densité et, plus généralement, des propriétés thermophysiques similaires entre les phases condensées en équilibre, ainsi que de la forte opacité du fluide dans les conditions de réservoir. Cette thèse a pour objectif d'étudier expérimentalement les transitions de phase dans plusieurs échantillons de pétrole brut du pré-sel brésilien recombinés avec du dioxyde de carbone, du méthane et des mélanges de ces deux gaz dans différentes proportions afin de déterminer les paramètres qui influencent le comportement de phase de ces fluides. Les échantillons de pétrole brut étudiés diffèrent principalement par leurs distributions S.A.R.A. (saturés / aromatiques / résines / asphaltènes). Pour mener à bien cette recherche, une combinaison de techniques indirectes, telles que la diffusion de lumière, le comportement p-V ou le facteur-Y, a été employée, associée à des techniques d'observation directe du fluide étudié. En particulier, une technique d'observation directe basée sur l'utilisation d'une caméra infrarouge (SWIR) a été appliquée en raison de sa capacité à examiner des fluides opaques dans un domaine spécifique de longueur d'onde où l'absorbance des asphaltènes est minimale. Les résultats ont montré l'apparition d'une transition de type liquide hydrocarboné-liquide hydrocarboné. Cependant, ce type de transition n'a été observé que dans des mélanges contenant une forte teneur en gaz ($z_{gaz} > 70$ mol%) et n'était pas limité

au type de gaz ajouté, en particulier au CO_2. De plus, dans certains cas, l'équilibre liquide-liquide a évolué vers un équilibre triphasique liquide-liquide-vapeur, même dans des conditions atypiques de pression et de température. Les résultats suggèrent que l'apparition d'un équilibre liquide-liquide est liée à la forte asymétrie du système, notamment entre l'excès de gaz et la fraction lourde du pétrole brut, comme les asphaltènes. La modélisation réalisée soutient l'hypothèse selon laquelle la formation de la deuxième phase liquide est une conséquence de la solubilité limitée de la fraction lourde du pétrole brut dans des systèmes à haute teneur en gaz. En outre, l'approche de modélisation thermodynamique indique que le caractère non ségrégatif entre les phases liquides est dû à une grande proximité des densités des phases. Enfin, un système synthétique visant à reproduire l'équilibre liquide-liquide observé dans les fluides du pré-sel a été proposé puis étudié dans les mêmes conditions que les fluides de réservoir. Cependant, le système choisi n'a pas pu reproduire le comportement atypique des fluides du pré-sel, probablement en raison de l'apparition d'un locus solide-liquide, qui c'est superposé à un éventuel locus liquide-liquide dans le diagramme de phases.

RESUMO

O estudo do comportamento de fases é uma etapa crucial para o projeto e otimização de processos de separação, sobretudo para indústrias de alta pressão, como a indústria petrolífera. Devido ao caráter multicomponente do petróleo, o equilíbrio de fases experimentalmente observado vai além do equilíbrio bifásico líquido-vapor comumente encontrado em sistemas mais simples. Os fluidos de reservatório produzidos no pré-sal brasileiro apresentam um alto teor de gás associado, especialmente dióxido de carbono. Esse fator, somado à alta opacidade do petróleo, acarreta uma série de dificuldades no estudo experimental do comportamento de fases desses fluidos. Recentemente, alguns estudos reportaram a ocorrência de imiscibilidade entre fases líquidas em um amplo domínio de pressão e temperatura, sobretudo em condições de temperatura bem acima da temperatura crítica do dióxido de carbono. Esse equilíbrio líquido-líquido apresenta algumas características que dificultam uma detecção precisa das condições em que a transição ocorre, devido principalmente à alta opacidade do fluido e ao baixo contraste de densidade entre as fases líquidas. Dessa forma, esta tese apresenta um estudo do comportamento de fases de diversas amostras de petróleo do pré-sal brasileiro recombinadas com dióxido de carbono, metano e misturas entre esses dois gases. As amostras de petróleo investigadas diferem-se principalmente em termos das distribuições S.A.R.A. Para desenvolver melhor esta pesquisa, foi utilizada uma combinação de técnicas indiretas, como espalhamento de luz, curva *p-V* e curva *fator-Y,* juntamente com técnicas de observação direta do fluido investigado. Em especial, uma técnica de observação direta baseada na utilização de uma câmera infravermelha foi aplicada devido à sua capacidade de investigar fluidos opacos. Os resultados demonstraram que a ocorrência de uma transição líquido-líquido não é exclusiva de apenas uma amostra de petróleo do pré-sal brasileiro. No entanto, esse tipo de transição só foi observado em misturas com alto teor de gás ($z_{gás} > 70$ mol%), não sendo restrita ao tipo de gás adicionado. Além disso, em alguns casos, o equilíbrio líquido-líquido evoluiu para um equilíbrio trifásico líquido-líquido-vapor, mesmo em condições atípicas de pressão e temperatura. Os resultados sugerem que a ocorrência de um equilíbrio líquido-líquido está relacionada à alta assimetria do sistema, sobretudo entre o gás em excesso e a fração mais pesada do petróleo, como os asfaltenos. A modelagem realizada suporta a hipótese de que a segunda fase líquida formada é uma consequência da limitação da solubilidade da fração pesada do petróleo em sistemas com alto teor de gás adicionado. Ademais, a

abordagem utilizada para modelagem termodinâmica indica que o caráter não segregativo entre as fases líquidas se deve à grande proximidade na densidade das fases. Por fim, um sistema sintético, com o objetivo de reproduzir o equilíbrio líquido-líquido observado nos fluidos do pré-sal, foi investigado. No entanto, o sistema escolhido não foi capaz de reproduzir o comportamento atípico dos fluidos do pré-sal, provavelmente devido à ocorrência de um loci sólido-líquido, que sobrepôs um possível loci líquido-líquido no diagrama de fases.

Palavras-chave: comportamento de fases; alta pressão; pré-sal; líquido-líquido; dióxido de carbono; metano; modelagem termodinâmica; sistema sintético.

FIGURE LIST

TABLE LIST

SUMMARY

1   THESIS STRUCTURE

To ensure better understanding and organization, this Thesis was divided into five chapters, covering theoretical concepts, literature review, and experimental results, as follows:

Chapter 1 addresses fundamental theoretical and experimental aspects of high-pressure phase behavior in asymmetric systems. It also presents various experimental techniques, emphasizing their advantages and disadvantages in the context of reservoir fluid phase behavior studies. Additionally, the chapter reviews relevant literature for each topic.

Chapter 2 presents the experimental results of a fundamental study on Brazilian pre-salt crude oils from different fields, recombined with carbon dioxide. The study employs a combination of classical PVT methods and a high-pressure microscopy technique working with a SWIR camera. These techniques are compared, highlighting certain limitations in detecting specific types of phase transitions.

Chapter 3 presents a study of two distinct Brazilian pre-salt crude oils combined with carbon dioxide, using the same experimental setup as in Chapter 2. This part of the Thesis investigates the occurrence of liquid to liquid-liquid phase transitions and correlates them with S.A.R.A analysis, with a particular focus on the resins and asphaltene content.

Chapter 4 describes a series of systematic phase behavior experiments conducted using a full-visibility PVT equilibrium cell coupled with a SWIR camera. These experiments were performed on three different crude oil samples from the same field, with the addition of carbon dioxide and methane. Additionally, a thermodynamic modeling study was conducted to describe the experimentally observed phase transitions.

Chapter 5 presents a fundamental study of the fluid phase behavior of a model system composed of *o*-terphenyl, 2,2,4,4,6,8,8-heptamethylnonane, and dodecylcyclohexane, with a gas mixture of methane, ethane, propane, and carbon dioxide. The aim of this study was to identify a synthetic system capable of reproducing the complex phase equilibria observed in the crude oil systems studied in Chapters 2, 3, and 4, in order to better understand them.

2 CHAPTER I: INTRODUCTION

The variations in pressure, temperature, and composition during the production of reservoir fluids can cause complex phase transitions, leading to changes in fluid properties and multiphase flow. For this reason, understanding the phase behavior of reservoir fluids is crucial for designing and optimizing oil production (Mancilla-Polanco et al., 2019), especially for enhanced oil recovery (EOR) based on light solvent injection methods. Carbon dioxide (CO_2) is a typical solvent used for this purpose, so knowing its solubility in crude oil at reservoir operational conditions and understanding its effects on oil properties are fundamental for planning oil recovery processes (Araújo et al., 2016). One practical application of this understanding is the development of primary separation strategies based on knowledge of the vapor-liquid equilibrium (VLE) region in the phase diagram. Because of the complexity of reservoir fluids, phase transitions beyond simple biphasic vapor-liquid (VL) equilibria can be observed with some live oils. These include liquid-liquid (LL), liquid-liquid-vapor (LLV), solid-liquid-vapor (SLV), and solid-liquid-liquid (SLL) equilibria (Al Ghafri; Maitland; Trusler, 2014; Amani; Gray; Shaw, 2013; Borges et al., 2015; Cardoso et al., 2015; Daridon et al., 2001, 2020; Dini; Becerra; Shaw, 2016; Eghbali; Dehghanpour, 2017; Ferreira et al., 2018; Johnston et al., 2017; Ma; Chen; Abedi, 2016; Orr; Yu; Lien, 1981; Romero Yanes et al., 2021b) with different types of solid phases, including waxes and asphaltenes. Therefore, understanding the operational conditions, specifically the pressure and temperature at which multiphase equilibrium occurs, is crucial for mitigating or preventing issues related to multiphase flow involving or not a solid appearance. Typically, for a mixture with carbon dioxide, the LLE related to crude oil samples is associated with low-temperature conditions (Larson et al., 1989; Orr; Jensen, 1984; Orr; Yu; Lien, 1981; Turek; Metcalfe; Fishback, 1988a), especially at a temperature near to CO_2 critical temperature, where CO_2 miscibility is limited. However, recent studies have reported a liquid-liquid equilibrium (LLE) in Brazilian pre-salt crude oil samples (Daridon et al., 2020; Romero Yanes et al., 2021b), which presents a high gas-oil ratio (GOR)(Cardoso et al., 2015; Da Costa Fraga et al., 2015). These LLE have been observed as a dispersed phase in a continuous oil phase at temperatures significantly exceeding the critical temperature of CO_2. Briefly, liquid phase splitting manifests as highly dispersed phases that do not segregate due to gravity, posing fluid sampling and phase

characterization challenges. Nevertheless, the primary factor responsible for these non-conventional phase transitions is not fully understood.

The inherent opacity of crude oil samples necessitates specific methods for accurately measuring fluid phase transitions. However, no ideal method can observe all phase transitions related to crude oil samples. For this reason, a comprehensive understanding can only be achieved by combining different techniques. In the literature, several methods were used to measure phase transitions in crude oil + gas mixtures, either through direct observation (Araújo et al., 2016) or by mapping physical properties changes, such as compressibility (Agrawal et al., 2012; Johnston et al., 2017; Mancilla-Polanco et al., 2019; Romero Yanes et al., 2019a) and viscosity (Shadman et al., 2012) or even by calorimetry methods (Andersen; Birdi, 1991; Juyal et al., 2011). However, the conventional PVT techniques are less sensitive to the L→LL transitions observed in these pre-salt reservoir fluids.

Considering the complexity regarding the phase equilibria studies of the Brazilian pre-salt oils along with the high gas content associated with these fluids, the main goal of this Thesis was to investigate the fluid phase behavior of different pre-salt reservoir fluids samples by adding another type of gases, such as: i) pure carbon dioxide (CO_2); ii) methane (CH_4); as well by adding gas mixtures, to reproduce live oil behavior. To achieve this, a combination of several experimental techniques was applied to better characterize phase diagrams found in such recombined oil + gas systems.

2.1 Fundamental aspects of fluid phase equilibria

Fluid phase behavior describes how a system changes or remains in its phase when varying thermodynamic conditions such as pressure, temperature, and composition. In a closed multiphase system, thermodynamic equilibrium can be attributed to the absence of thermal pressure and mass gradients. In general, these conditions are achieved by the equality of temperature (T), pressure (p), and chemical potential (μ) in each phase that composes the system. For instance, the following equations present these conditions for a simple two-phases equilibrium system:

$$T^\alpha = T^\beta \tag{1.1}$$

$$p^\alpha = p^\beta \tag{1.2}$$

$$\mu^\alpha_{(i=1,N)} = \mu^\beta_{(i=1,N)} \tag{1.3}$$

where the superscript α and β denotes the phases in equilibrium, and the subscript i and N represents the specific component and the number of components in the mixture, respectively.

Fluid phase equilibria are usually represented in a *pressure-temperature* (*p-T*) projection, called a phase diagram, which delimits the domain of pressure and temperature conditions in which the phases can coexist. The Gibbs phase rule (Prausnitz; Lichtenhaler; De Azevedo, 1999) is used to determine the number of the intensive properties needed to describe any system and can be given by the following relation:

$$F = N - \pi + 2 \tag{1.4}$$

where F, N, and π denotes the number of degrees of freedom (intensive properties), the number of components present in the system, and the number of phases in equilibrium, respectively. For a pure component, it can be seen from the Gibbs phase rule that the two-phase equilibrium (liquid-vapor, solid-liquid or solid-vapor) can be determined by changing just one property. However, as the number of components increases, for example, in a binary mixture, the two-phase equilibrium can be observed in a *p-T* domain. The shape and complexity of the phase diagram increases as the number of components in the mixture increases and the difference (asymmetry) between the molecules that comprise the mixture increases. As a result of the increased number of components in reservoir fluids, regions of multiphasic equilibria emerge in these multicomponent systems. However, for a simplification purpose, it is common to study this multicomponent system as a pseudo-binary system formed by a gas with an oil.

A systematic fluid phase behavior classification proposed by van Konynenburg and Scott (1980) for binary mixtures suggests that the phase diagram of such a mixture can present six main types of fluid. This classification involves different fluid-fluid phase equilibria in binary mixtures and is based on a topological analysis of the phase regions and the critical lines that delimit each region. Figure 1 shows van Konynenburg and Scott's classification for binary organic mixtures. The simplest phase

diagram is represented by Type I, which features a continuous liquid-vapor (LV) critical line that links the critical point of the lightest compound (C_1) to those of the heaviest compound (C_2). This type of phase diagram can be observed in mixtures of molecules with similar size, shape, and properties, such as a mixture of CO_2 + light *n*-alkanes (Brown; Kidnay; Sloan, 1988; Li; Dillard; Robinson, 1981). Type II phase diagram also presents a continuous liquid-vapor critical line between the critical points of the components. However, due to the chemical difference between the compounds, liquid-liquid (LL) immiscibility starts to be observed at low temperatures. This means that at certain conditions, the liquid separates into two distinct liquid phases. The LL critical line associated to this transition present a high slope in the pressure-temperature graph. It intercepts at the upper critical endpoint (*UCEP*) the three-phase liquid-liquid-vapor (LLV) line where liquid, liquid and vapor coexist. . The *UCEP* ends the three-phase equilibrium line at temperature lower than the critical temperature of the C_1 (Hottovy; Luks; Kohn, 1981). Type II is observed for CO_2 + *n*-alkanes mixture up to dodecane (Enick; Holder; Morsi, 1985).
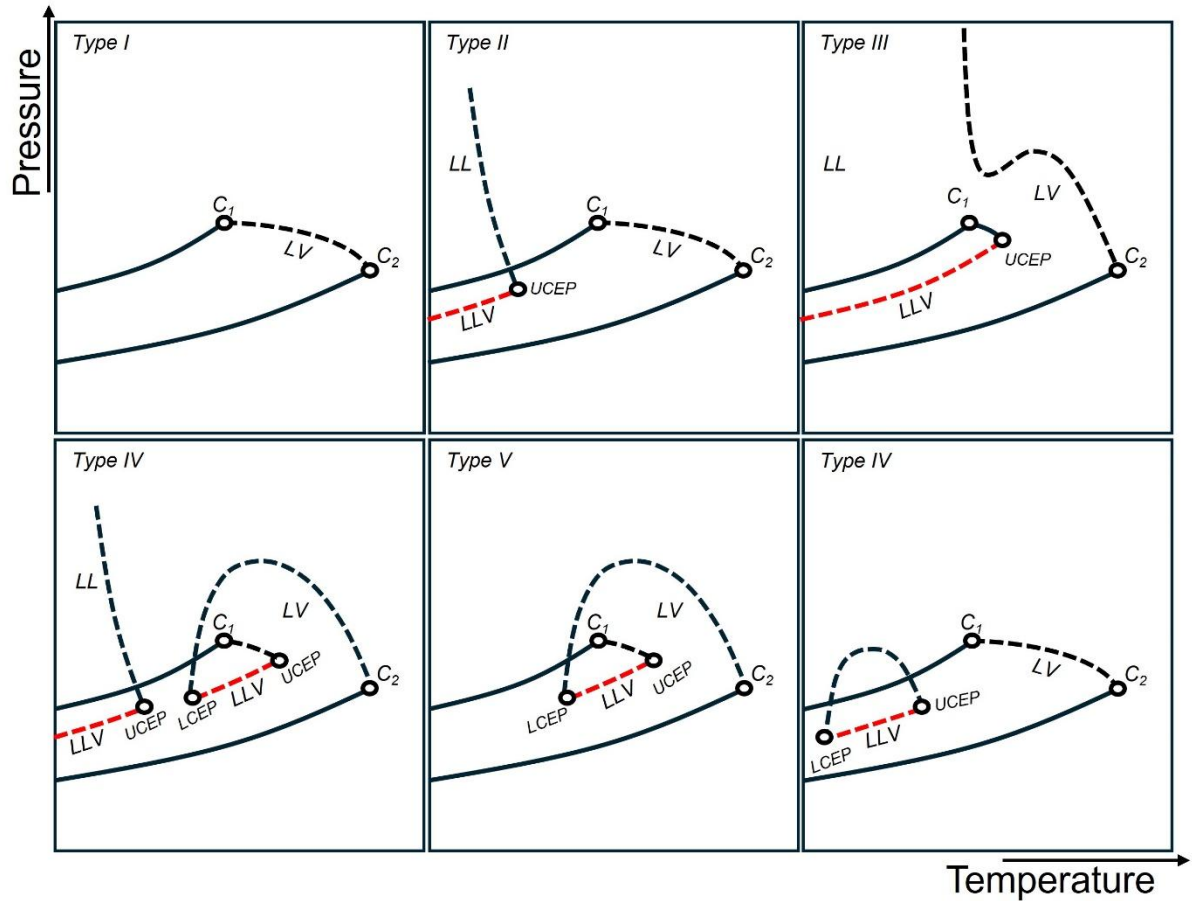
Figure 1. Phase diagram types according to van Konynenburg and Scott's (1980) classification for organic binary mixtures. Adapted from de Hemptinne et al. (2012)

As the liquid-liquid critical loci moves towards the higher temperatures, the continuous liquid-vapor critical line is interrupted, and two critical lines are observed. The first connects the critical point of C_1 to the three-phase liquid-liquid-vapor equilibrium at the *UCEP*. The second starts at the critical point of C_2 and runs towards high-pressure conditions. If one of the components has a lower solidification temperature line, the liquid-liquid region can remain up to infinite pressures. This phase diagram shape is classified as Type III. It is commonly observed in highly asymmetric mixtures (Daridon et al., 2021; Schneider et al., 1967; Vitu et al., 2008b; Yanes; Montel; Daridon, 2022a). In the Type IV diagram, the critical point C_1 is linked to a *UCEP* and the critical point C_2 is linked to a lower critical endpoint (*LCEP)* so that both *UCEP* and *LCEP* are connected, forming a liquid-liquid-vapor line. A second three-phase LLV appears in Type IV diagram from low temperature to a second *UCEP*. Therefore, Type IV diagram exhibits three critical lines and two three-phase lines ended by two *UCEP*s and one *LCEP*.

The Type V diagram has a shape similar to Type IV but it does not have a liquid-liquid critical line and a second LLV three-phase domain. The projection of the phase diagram in the *p-T* plane shows two critical lines and a liquid-liquid-vapor (LLV) line that extends between a *LCEP* and a *UCEP*.

Type VI systems are relatively rare compared to the other types. The pressure-temperature (p,T) phase diagram of such systems is characterized by a continuous liquid-vapor (LV) critical line that extends between the critical points of the two pure components, similar to type I. However, it also includes a liquid-liquid critical curve that begins at a lower critical endpoint and concludes at an upper critical endpoint. Both of these critical endpoints are also connected by a three-phase liquid-liquid-vapor (LLV) equilibrium line.

The classification of van Konynenburg and Scott (1980) is limited to fluid-fluid phase transitions. However, if the molecules of at least one component in the mixture can order themselves into a solid phase, the type of phase diagram can change smoothly with the addition of a solid region, primarily resembling variations of the Type II and Type III shapes shown in Figure 1 (Quinzio et al., 2023). Typically, in binary mixtures of CO_2 and high molecular weight *n*-alkanes, the occurrence of the solid phase slightly alters the overall shape of the phase diagram (Braga; Tavares; Ndiaye, 2022; Daridon et al., 2021). In addition, depending on the melting temperatures, the solid phase limits the occurrence of the high-pressure liquid-liquid equilibrium observed in the Type III diagram (Yanes; Montel; Daridon, 2022a); however, under specific conditions, the solid-liquid line intersects the liquid-liquid-vapor three-phase line, forming a quadruple point (*Q*-point). In complex systems, such as reservoir fluids, the occurrence of a solid phase cannot be negligible, as its occurrence is strongly related to flow assurance problems, such as asphaltene and wax precipitation (Daridon et al., 2001). Various approaches have been developed to include the occurrence of a solid phase and its influence on the phase diagram of complex mixtures (Benelli; Pisoni; Cismondi-Duarte, 2023; Da Silva et al., 2018; Daridon et al., 2001; Pauly et al., 2000; Quinzio et al., 2023).

2.2 High-pressure fluid phase equilibria

2.2.1 High-Pressure Phase Behavior of Hydrocarbon systems

Experimental data for the fluid phase equilibrium of multicomponent systems is scarce in literature but is fundamental for reservoir engineering. In this context, several studies with binary or ternary model systems have been carried out to understand and provide phase equilibrium data to understand the multicomponent behavior of studies.

Several studies of asymmetric mixtures composed of a low molecular weight gas (e.g. methane, ethane, propane, and CO_2 ...) and heavy liquid or solid *n*-alkanes, mainly linear n-alkanes, have been reported (Chen; Chappelear; Kobayashi, 1976; Dohrn et al., 2024; Fonseca; Dohrn; Peper, 2011; Hottovy; Kohn; Luks, 1982; Pauly; Coutinho; Daridon, 2007; Peper; Fonseca; Dohrn, 2019). Typically, in terms of the type of phase equilibrium observed experimentally, all these systems present a simple two-phase liquid-vapor equilibrium, with a liquid-liquid and liquid-liquid-vapor domain at low temperatures, describing a Type II or III form, depending on the compositions studied. For example, the partial miscibility of ethane is greater than that of methane, resulting in the formation of a liquid-liquid region observed in mixtures of *n*-alkanes with a carbon chain number of up to 20 (Estrera; Arbuckle; Luks, 1987; Kohn; Kim; Pan, 1966; Peters; De Roo; Lichtenthaler, 1991). The same trend remains if the mixture is made with the addition of propane, especially at temperature conditions lower than the critical temperatures of propane (Ma; Chen; Abedi, 2016; Peters et al., 1989; Peters; De Roo; De Swaan Arons, 1993).

Most studies reported in the literature on this scenario aim to understand the behavior of hydrocarbon phases with the addition of CO_2 (Dohrn et al., 2024). Depending on the composition of the mixture, the miscibility of CO_2 is limited in *n*-alkanes, especially at temperatures lower than the critical temperature of CO_2. For example, a Type II phase diagram is related to linear carbon chains up to 12 (Fall; Fall; Luks, 1985), whereas for linear carbon number 13 and beyond, a Type III phase diagram is observed for this type of mixture (Daridon et al., 2021; Fall; Fall; Luks, 1985; Fall; Luks, 1985; Hottovy; Luks; Kohn, 1981; Huie; Luks; Kohn, 1973; Kordikowski; Schneider, 1993; Poettmann; Katz, 1945; Rodriguez-reartes et al., 2009; Schneider et al., 1967; Sebastian et al., 1980; Vitu et al., 2008b), and this trend remains for CO_2 + aromatic mixtures (YANES; MONTEL; DARIDON, 2022). Nevertheless, the liquid-liquid immiscibility is

not observed for mixtures with branched alkanes, for example, 2,2,4,4,6,8,8-heptamethylnonane (Yanes; Montel; Daridon, 2022b), methyl cyclopentane, isopropyl cyclohexane (Vitu et al., 2008a), 2,4 dimethyl pentane (Ioniţă et al., 2023), 2,3 dimethyl butane (Zid et al., 2022a), cycloheptane (Zid et al., 2022b), and cyclooctane (Vitu et al., 2021). A Type I or II phase diagram is commonly observed for branched alkanes with an uninterrupted liquid-vapor critical line.

As previously mentioned, if the crystallization temperature of the alkanes is high enough, a solid phase is observed in the phase diagram at temperature close to liquid-liquid phase separation. Consequently, liquid to liquid-liquid phase transitions can interfere with the solid-appearance, as is the case for mixtures with CO_2 + docosane (Fall; Fall; Luks, 1985), CH_4 + heptadecane (Pauly; Coutinho; Daridon, 2007), or even for multicomponent mixtures such as CH_4 + waxes (Pauly; Coutinho; Daridon, 2010, 2012). The complexity of the phase equilibria observed experimentally is usually expected to increase with the number of components, especially for three-phase equilibria, since these are no longer monovariant and occupy an area of the phase diagram (p-T) limited by the type of phases that surround it. However, when considering multicomponent mixtures such as reservoir fluids as pseudo-binary oil-plus-gas systems, the complexity of fluid phase equilibria does not necessarily increase significantly in most cases. The phase behavior generally remains relatively straightforward. Nevertheless, a notable exception arises in certain conditions where the coexistence of three distinct hydrocarbon liquid phases can be observed. This phenomenon has been identified in some pre-salt reservoir fluids (Romero Yanes et al., 2021b), adding an extra layer of complexity to their phase behavior and requiring specific attention in experimental and modeling approaches.

All these fundamental studies are motivated by understanding the complex behavior of the fluid phase of the reservoir fluids. Knowledge of the binary or ternary phase diagrams across the global composition can help understand the reservoir fluids' phase diagrams. As the compositional character of reservoir fluids is a difficult task to measure, an interesting approach is to study multicomponent mixtures with known composition, providing valuable experimental data (Al Ghafri; Maitland; Trusler, 2014; Gui et al., 2017; Regueira et al., 2017; Shariati; Peters; Moshfeghian, 1998a; Shaw; Béhar, 2003; Vitu et al., 2007).

2.2.2   Multiphasic Phase Behavior of Reservoir Fluids

Despite all the efforts to describe the fluid phase behavior observed in reservoir oil fluids through binary or multicomponent synthetic mixtures, the most reliable approach remains the direct analysis of samples obtained from the reservoir through downhole sampling. This method allows for the collection of representative fluid samples under in-situ conditions, capturing the true composition and phase behavior of the reservoir fluids. Downhole sampling ensures that the fluid sample called live oil reflects the actual conditions within the reservoir. By analyzing these samples in the laboratory, researchers can gain valuable insights into the fluid properties, phase equilibria, and potential challenges related to production, such as asphaltene precipitation or wax deposition.

However, live oil samples can be costly due to various difficulties involved in sampling under the reservoir's pressure and temperature conditions. These challenges include the need for specialized equipment and the potential for sample contamination or alteration during sampling. To address this issue, it is common practice to use the oil collected under separator conditions, referred to as dead oil, and recombine it with a gas of similar composition to the gas obtained in the separator. This recombination allows for the creation of a mixture that approximates the live oil's properties, enabling researchers to study the fluid behavior and phase equilibria more effectively. While this method may not fully replicate the complexities of live oil, it provides a practical and cost-effective alternative for conducting experiments and gaining insights into reservoir fluid behavior.

Due to the natural complexity of reservoir fluids, many studies are available in the literature to investigate the phase behavior of different reservoir fluids. The type of gas added in the recombination to reproduce the live oil is determined by the reservoir fluid's characteristics, impacting the phase equilibria observed in each system. For instance, in the case of bitumen fluids, liquid-vapor (LV), liquid-liquid (LL), and liquid-liquid-vapor (LLV) equilibria can be observed when mixed with propane (Badamchi-Zadeh et al., 2009a, 2009b; Dini; Becerra; Shaw, 2016), butane (Perez Claro et al., 2019) or pentane (Johnston et al., 2017). Since most of these low molecular weight gases or liquids can act as asphaltene precipitants, liquid-asphaltene (LA) regions can be observed, especially in bitumen fluids, which have a considerable amount of asphaltene

(AGRAWAL et al., 2012); for this type of reservoir fluid, mapping the phase boundaries can provide valuable information to mitigate flow assurance problems.

Investigating the fluid phase behavior for the enhanced oil recovery (EOR) process through solvent addition can help observe whether solvent injection may promote a single-phase or multiphase flow during production. Carbon dioxide (CO_2) is the most common solvent tested in the literature for EOR purposes. Similar to binary mixtures, multiphasic equilibria can be observed by mixing CO_2 and crude oil samples, depending on the global composition of the gas in the mixtures. For instance, multiphasic equilibria such as liquid-liquid, solid-liquid-vapor, and/or liquid-liquid-vapor occur typically only when the gas composition exceeds 50 mol% in the mixture (Agrawal et al., 2012; Amani; Gray; Shaw, 2013; Badamchi-Zadeh et al., 2009b; Bryant; Monger, 1988; Cardoso et al., 2015; Coutinho; Jørgensen; Stenby, 1995; Daridon et al., 2001, 2020; Dini; Becerra; Shaw, 2016; Eghbali; Dehghanpour, 2017; Johnston et al., 2017; Keyvani; Qajar; Amani, 2023; Khan; Pope; Sepehrnoori, 1992; Kokal; Sayegh, 1993; Larson et al., 1989; Mancilla-Polanco et al., 2019; Orr; Jensen, 1984; Orr; Yu; Lien, 1981; Perez Claro et al., 2019; Romero Yanes et al., 2020a; Turek; Metcalfe; Fishback, 1988b; Zuo et al., 2023). Generally, these liquid-liquid phase equilibria are characterized by a hydrocarbon-rich phase (L1) and a CO_2-rich phase (L2). Under these conditions, the CO_2-rich phase is expected to extract some hydrocarbons from the oily phase, promoting a similar density between the phases, which can hinder phase segregation (Al Ghafri; Maitland; Trusler, 2014).

Figure 2 illustrates a qualitative comparison between the experimental data at $T = 305.15$ K for CO_2 + Maljamar oil (MW = 183.7 g·mol^{-1}) and CO_2 + diphenylmethane (MW = 168.23 g·mol^{-1}) at $T = 308.15$ K. The phase behavior regarding the type of phase equilibrium (i.e. LV, LL or LLV) observed for Maljamar oil is similar to that reported for the asymmetric binary mixture. All the data reported above show liquid-liquid and liquid-liquid-vapor transitions at temperatures below the critical temperature of CO_2, which in some cases extends to just 6 K above the critical temperature of CO_2. However, the asymmetry of the system is not a negligible factor in splitting two liquid phases. For crude oil samples, this asymmetry may be related to the heavy fraction of the crude oil, especially the heavier fraction, such as C_{7+} or resins and asphaltenes.
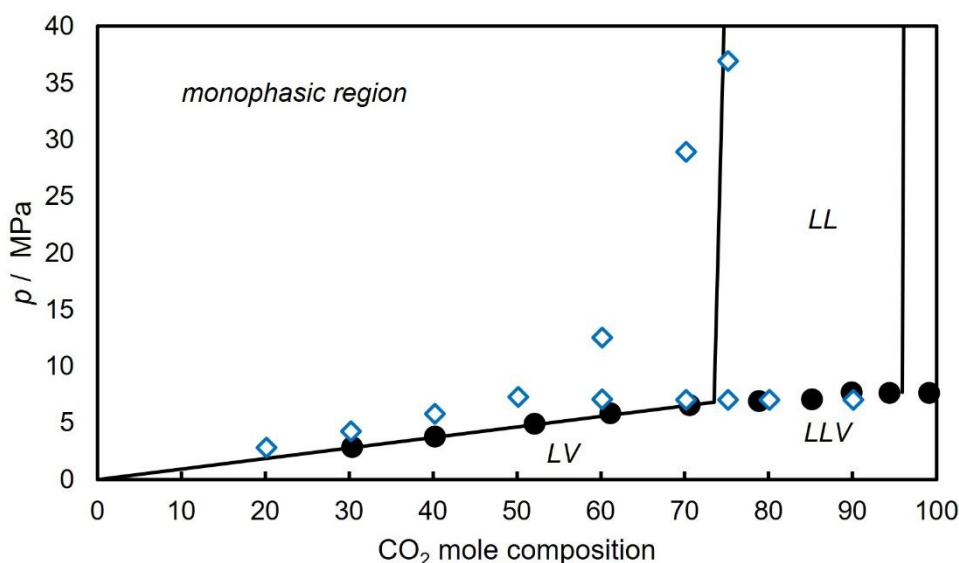
Figure 2. Isothermal pressure-composition diagram comparison between CO_2 + Maljamar oil reported by Orr *et al*. (1984) (black circle and line, —●—); and CO_2 + diphenylmethane reported by Yanes *et al*. (2022) (blue diamonds ◊).

Recently, some phase behavior studies of Brazilian pre-salt samples have shown a series of complex phase equilibria. Typically, pre-salt reservoir fluids have a high gas content, especially related to carbon dioxide (Da Costa Fraga et al., 2015). Cardoso *et al.* (2015) reported a study of the phase behavior of pre-salt live oils under high-pressure conditions that present a liquid-liquid equilibrium at $T = 339.15$ K, in which the second liquid phase was reported as a droplet phase that hardly coalesces. This temperature significantly exceeds the critical temperature of carbon dioxide and also surpasses the upper critical endpoints found in the phase diagrams of CO_2 and heavy hydrocarbon binary systems.

Following the findings of Cardoso *et al*., a series of studies were reported to investigate the fluid phase behavior of pre-salt fluids, especially to understand and show the presence of an unusually high-temperature liquid-liquid equilibrium. Daridon *et al.* (2020) studied a sample from the Brazilian pre-salt at reservoir temperature ($T = 358.00$ K). In their study, they added gas to the dead oil to replicate the behavior of live oil. They found that when the gas content exceeded 70 mol%, a liquid-liquid equilibrium appears This equilibrium was characterized by a mist-like liquid phase dispersed within a continuous phase of liquid oil, exhibiting no phase segregation even after extended periods of equilibrium. In addition, Yanes *et al.* (2022) also reported a liquid-liquid

equilibrium that did not segregate in pre-salt samples mixed with carbon dioxide and methane. A liquid-liquid equilibrium was observed at high temperature conditions, along with a liquid-liquid-vapor equilibrium at conditions close to the critical temperature of CO_2. However, the three-phase liquid-liquid-vapor loci extended to very high pressures and temperatures for mixtures with a high methane content. Similar to the results reported by Daridon *et al.* (2020), this liquid-liquid equilibrium appeared as a dispersed phase in a continuous liquid phase by adding carbon dioxide or methane in dead crude oil. Figure 3 illustrates the high-pressure, high-temperature liquid-liquid equilibrium observed by Daridon *et al.* (2020).

Figure 3. Liquid-liquid equilibrium at $T = 358.00$ K reported by Daridon *et al.* (2020) for a synthetic Brazilian pre-salt live oil. Adapted from Daridon *et al.* (2020).

This high-temperature phase transition from liquid to liquid-liquid presents several challenges from an experimental perspective. No interface is observed since liquid phases do not separate into distinct phases with different densities (Daridon et al., 2020). Additionally, due to the complexity of the transitions involved and the high opacity of the medium, it is plausible that this type of phase equilibrium has been overlooked in many past high-temperature and high-pressure (HT-HP) reservoir fluid studies. Therefore, a combination of experimental PVT techniques with high accuracy must be employed to better characterize the phase transition, ideally including at least one visual technique as proposed by DARIDON et al., 2020.

2.2.3   Asphaltene and wax precipitation in reservoir fluids

Flow assurance issues related to reservoir fluid production extend beyond multiphase flow. One significant concern is the potential formation of hydrocarbon solid phases within the reservoir fluids, which can partially or entirely block a production pipeline. Typically, these flow assurance challenges involving a hydrocarbon solid phase are associated with asphaltene destabilization or wax precipitation. Asphaltene destabilization can lead to the formation of asphaltene aggregates at different stages of aggregation that may accumulate and block flow pathways, while wax precipitation can create wax solid deposition or gel-like formation that restricts fluid movement. Both phenomena can appear due to change in either pressure, temperature or fluid composition. Understanding the conditions that promote solid phase formation is crucial for developing effective flow assurance solutions, ensuring uninterrupted production, and minimizing operational disruptions.

Asphaltenes are the heaviest and most polar fraction present in petroleum. This fraction consists of polyaromatic compounds containing heteroatoms attached to carbon chains. Asphaltenes can destabilize from reservoir fluids as a solid or liquid viscous material (bitumen), which can cause blockages in wells or pipeline production (Pedersen; Christensen; Shaikh, 2015). Due to the complexity of asphaltene's molecular structure, each oil has different characteristics. Therefore, it is reasonable to define it as a class of complex organic compounds of reservoir fluids insoluble in linear *n*-alkanes, such as *n*-pentane or *n*-heptane, but soluble in aromatic compounds, such as toluene. Asphaltenes in reservoir fluids are typically stabilized as nanoaggregates under reservoir conditions (high pressure and temperature). These nanoaggregates are small (~2-5 nm) dispersed entities that remain suspended in the crude oil due to solvent property of reservoir fluid.

Nevertheless, because of the natural depletion during oil production, pressure, temperature, or local composition changes can reduce the solvent power of the crude oil, making it less effective at stabilizing nanoaggregate asphaltenes that undergo a multistage aggregation process (Chen et al., 2020; Eyssautier; Frot; Barré, 2012; Goual et al., 2011) cause asphaltene destabilization. In this process, nanoaggregates begin to aggregate, forming larger clusters. These clusters are still small enough (~10 nm) to remain suspended but are about to be destabilized. Clusters of nanoaggregates themselves

aggregate forming larger structures called clusters of clusters. At this stage, the clusters become more unstable and may start to precipitate. They grow further, forming flocs, which are large (>500nm), porous, and loosely bound aggregates. They are no longer stable in the crude oil and separate from the fluid phase.

It was observed that the asphaltenes can precipitate even under high-temperature conditions (Espinoza Mejia; Li, 2023). Asphaltene precipitation can also occur during gas injection of the EOR process. The content of light compounds in oil plays an important role in asphaltenes stability (Cardoso et al., 2015). The stability of asphaltene is commonly assessed at atmospheric pressure by titrating the crude oil sample with light *n*-alkanes and by microscopic inspection (Alboudwarej et al., 2002; Alves et al., 2019; Romero Yanes et al., 2021c; Saidoun et al., 2019). The results obtained from these tests are extrapolated to high pressures to understand the destabilization of asphaltenes caused by fluid depletion and the release of light components (Duran; Schoeggl; Yarranton, 2019).

At high pressure, it is expected that the solubility parameter of the liquid phase will be close to that of asphaltenes, keeping them in solution (Romero Yanes et al., 2021a; Verdier; Duong; Andersen, 2005). However, as pressure and temperature change during oil production, the solubility parameter of the fluid also changes, causing asphaltenes to precipitate. Typically, the boundaries of asphaltene precipitation are depicted on a pressure-temperature diagram alongside the fluid-fluid transitions described in the previous section. The effect of temperature on asphaltene precipitation is not yet well understood, and phase behavior studies are the most common type of research conducted to investigate it. Several experiments have been carried out to better characterize the boundaries of asphaltene precipitation, with some showing an increase in asphaltene solubility with rising temperature (Daridon et al., 2020; Kabir; Jamaluddin, 2002; Kokal et al., 1992), while others report the opposite trend (Daridon; Carrier, 2017; Idem; Ibrahim, 2002; Verdier et al., 2006). As asphaltenes can be observed in a large domain of the *p-T* diagram, they are expected to be in equilibrium with other phases. For instance, in heavy oil such as bitumen, which contains a high amount of asphaltenes, a liquid-liquid equilibrium is observed (Johnston et al., 2017; Mancilla-Polanco et al., 2019; Perez Claro et al., 2019), characterized by an oil-rich phase and a viscous asphaltenic phase. Additionally, depending on the solvent mixed with the crude oil, a vapor phase rich in light components can be observed along with the two liquid phases (Zhang et al., 2019). In contrast, for Brazilian pre-salt reservoir fluids, asphaltene

precipitation typically appears as a solid phase, distinct from the liquid-liquid or liquid-liquid-vapor equilibria (Cardoso et al., 2015; Daridon et al., 2020). This asphaltenic phase may or may not interact with the fluid phases. Experimental data on multiphase equilibria involving asphaltenes remains scarce in the literature. For fluids other than those from Brazilian pre-salt reservoirs, Shelton and Yarborough (1977) reported a four-phase liquid-liquid-vapor-solid equilibrium for a crude oil + CO_2 mixture, featuring a solid asphaltene phase, albeit at a lower temperature ($T = 307.59$ K).

Unlike asphaltene, wax precipitation corresponds to a phase transition of type fluid→fluid+solid that typically occurs at low temperature. Waxes are primarily composed of long-chain hydrocarbons (typically C_{18} - C_{80+}), including paraffins (alkanes) and, to a lesser extent, naphthenes and aromatics. In reservoir conditions, molecules of wax are fully dissolved in the crude oil, forming a homogeneous solution. Waxes precipitate when the temperature of the crude oil drops below the Wax Appearance Temperature (WAT). This temperature drop can occur during production, transportation, or storage, especially in cold environments. As the temperature drops below the WAT, small, waxy nucleus begin to form and then grow in size as more long-chain hydrocarbons attach to the existing crystals. This growth phase is generally restricted by the presence of natural surfactants in crude oils, which limit the size of the wax crystals formed within the fluid to approximately one to a few microns.

During production, precipitated waxes diffuse toward cold wall surfaces and accumulate, reducing the effective diameter of the tubing and thereby restricting multiphase flow. The primary factor driving this wax deposition is the thermal gradient between the oil and the surface temperature when it falls below the WAT.

Wax deposition is certainly the major flow assurance challenge in the oil and gas industry. To prevent it, it is essential to know the WAT of a reservoir fluid as a function of pressure and to represent in a pressure-temperature diagram. A limited amount of complete phase diagrams in the literature present fluid-fluid transitions along with asphaltene and wax precipitation (Daridon et al., 2020). For this type of phase transition, some research groups try to study multicomponent systems to investigate the influence of gas in the liquid-to-solid-liquid phase transitions (Shaw; Béhar, 2003). For simple binary mixtures, a typical Q-point (precise Q) can be observed at a specific pressure and temperature in the phase diagram, whereas for multicomponent systems, four-phase equilibria begin to appear within a narrow region of the p-T diagram (Daridon; Pauly; Milhet, 2002; Pauly; Coutinho; Daridon, 2010).

The simultaneous precipitation of asphaltenes and waxes is challenging for industry and academic researchers. In mixtures with high gas content, the asphaltene instability curve and the wax precipitation curve can intersect at low temperature and high pressure, leading to the observation of Wax-Asphaltene-Liquid-Liquid or even Wax-Asphaltene-Liquid phase equilibrium. This type of complex equilibrium is scarcely addressed in the literature, likely due to the lack of analytical techniques capable of detecting and distinguishing between the different solid phases (Li et al., 2019; Schabron et al., 2012), particularly under high-pressure and opaque conditions.

No single experimental method can determine and characterize all phase transitions in complex fluids like crude oil. For this reason, it is reasonable to use a combination of several direct and indirect experimental techniques better to understand the true nature of the observed phase transitions. The following section lists all experimental techniques used in the development of this study, highlighting their advantages and disadvantages.

2.3   Experimental techniques

In studies of fluid phase equilibria under high-pressure conditions, the selection of the experimental setup largely depends on the system being investigated (Dohrn et al., 2024; Fonseca; Dohrn; Peper, 2011; Peper; Fonseca; Dohrn, 2019). Typically, multiple methods are employed to avoid misinterpretation of phase transitions. Experimental techniques are generally classified into two categories: i) Analytical methods, where the compositions of the phases in equilibrium are measured, and ii) Synthetic methods, where the global composition of the mixture is precisely controlled and phase transitions are detected by systematically varying pressure or temperature conditions.

Analytical methods aim to achieve a biphasic equilibrium state to determine phase composition, either with or without sampling. This approach is commonly used for binary or ternary mixtures. For high-pressure measurements, phase composition is often determined indirectly, for instance, through spectroscopic techniques (Dohrn et al., 2024). However, several non-trivial challenges are associated with phase sampling, especially maintaining constant pressure and temperature conditions.

On the other hand, synthetic methods determine phase transitions by adjusting pressure, temperature, or even composition until a new phase is observed, requiring only a small amount of the mixture. However, synthetic methods are highly dependent on the preparation and accuracy of the mixture, as phase boundaries can vary based on the global composition of the mixture. Typically, synthetic methods are used for multicomponent complex systems such as reservoir fluids and the phase boundaries of these systems are determined by isothermal experiments, most of the cases at reservoir temperature. Due to the opaque nature of crude oil samples, various techniques have been developed over time to characterize the experimental phase boundaries more and more accurately.

The simplest and most common technique involves direct fluid inspection using sapphire windows coupled to equilibrium cells. This approach is generally sufficient for measuring liquid-vapor, solid-liquid, and solid-liquid-vapor transitions in clear fluids (Daridon et al., 2001) in synthetic mixtures. However, direct observation may miss the onset of phase transitions for darker fluids. This leads to their determination at conditions significantly below the actual transition point: liquid-vapor transition or asphaltene and wax precipitation. For this reason, it is common to monitor fluid properties to detect phase transitions indirectly. For example, liquid-vapor transitions are typically detected using a *pressure-volume* (*p-V*) plot, where a change in the slope of the curve indicates the formation of the vapor phase (Agrawal et al., 2012; Daridon et al., 2020; Johnston et al., 2017; Mancilla-Polanco et al., 2019; Perez Claro et al., 2019; Romero Yanes et al., 2019b, 2019a). Figure 4 illustrates a classical *p-V* plot for a live North Sea fluid reported by Daridon and Carrier (2017). This method allows for monitoring changes in fluid compressibility, revealing an increase in mixture volume due to forming a more compressible phase (vapor phase).
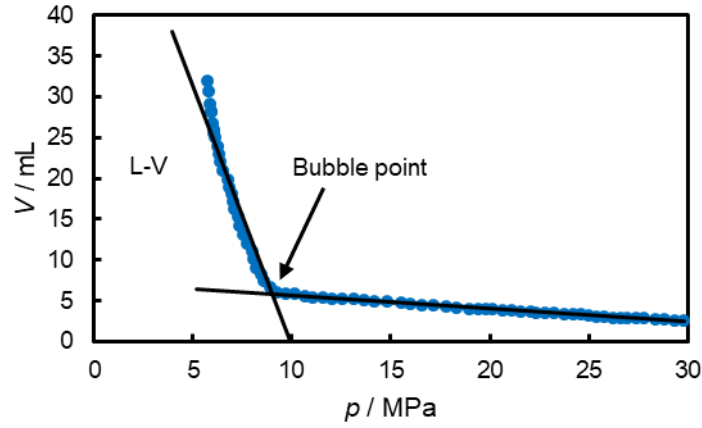
Figure 4. Bubble point pressure determined by *pressure-volume* (*p-V*) plot for a North Sea reservoir fluid at $T = 368.00$ K. Adapted from Daridon and Carrier (2017).

However, for fluids with a high gas content, it is possible that the fluid properties just below the phase transition do not show significant contrast. Under these conditions, the *p-V* plot may exhibit an almost continuous shape. For this reason, it is preferable to use the *Y*-factor (Hosein; Mayrhoo; McCain, 2014; Williams, 2011) curve (Daridon; Orlandi; Carrier, 2016), as described by the following equation:

$$Y_{factor} = -\frac{V_{inital}}{P_{inital}} \cdot \frac{\Delta P}{\Delta V} \qquad (1.5)$$

where V_{inital} and P_{inital} denotes the volume and pressure of the initial condition of the experiment, respectively; $\Delta P = P - P_{inital}$ and $\Delta V = V - V_{inital}$. The bubble point pressure is determined by a regime change in the *Y*-factor against pressure. The *Y*-factor reflects the increase in mixture volume as the system enters the two-phase region due to pressure changes. The *Y*-factor is expected to present small values for fluids with a high gas volume below the bubble point pressure. In contrast, the *Y*-factor may show larger values for fluids with minimal gas formation as pressure decreases (Pedersen; Christensen; Shaikh, 2015). This approach can be used when direct visual methods and the *p-V* curve are less accurate or inoperative.

The experimental work conducted for this Thesis, as presented in Chapters II, III, IV, and V utilized conventional procedures and techniques to gather data on phase behavior when these techniques were functioning under operating conditions. Specifically, methods such as pressure-volume (*p-V*) plots and the *Y*-factor method were

employed to obtain experimental data on liquid-vapor phase transitions. However, when the phase transitions became more complex, such as in the case of liquid-liquid equilibria, additional techniques were required to accurately capture the behavior of the system. These alternative methods, which are essential for understanding the intricacies of liquid-liquid phase behavior, are described in the following sections.

2.3.1 Light Scattering Technique

For dark samples like crude oil, it is common to use indirect techniques to determine phase boundaries. The most common method is light scattering. Due to heavy aromatic compounds, crude oil appears dark because it absorbs most visible light. However, most crude oil samples exhibit minimal absorbance in the near-infrared wavelength range ($\cong 1.5$ μm)(Hammami et al., 2000; Jamaluddin et al., 2002). This technique involves emitting light and detecting the transmitted light through the fluid while monitoring light transmittance as pressure, temperature, or composition changes. Light scattering occurs when a new phase forms in the bulk fluid, and the transmitted light through the fluid decreases.

This technique is well established in the literature and has been applied to the simple liquid to liquid-vapor transition in different crude oil samples (Borges et al., 2015; Cardoso et al., 2015; Jamaluddin et al., 2002; Kabir; Jamaluddin, 2002; Romero Yanes et al., 2019b), as well for wax precipitation (Paso; Kallevik; Sjöblom, 2009). Typically, the light transmittance against the pressure plot presents a well-known pattern for bubble point detection, showing a sharp drop, usually leading the transmitted signal power to zero. However, for solid phases such as asphaltenes, a gradual decrease in light transmission is observed as the pressure decreases due to the aggregation of asphaltene particles (Hammami et al., 2000; Jamaluddin et al., 2002; Yonebayashi et al., 2018).

Since the light scattering technique is an indirect method, this approach is expected to fail in multiphase equilibrium studies, e.g., liquid-liquid-vapor, solid-liquid-vapor, and solid-liquid-liquid. Once total light dispersion occurs, it becomes difficult to determine which phases are in equilibrium. Cardoso et al. (2015) reported that relying solely on light scattering techniques for studying phase behavior in reservoir fluids may lead to erroneous results regarding phase transitions, particularly in cases involving liquid-liquid immiscibility above bubble pressure. Furthermore, the light scattering

method allows investigation only in a specific region of the fluids, providing information on how light transmittance changes from a reference point, usually the initial monophasic state.

2.3.2 *High-pressure microscope inspection*

A standard visual inspection method used in fluid phase behavior studies is microscopy. This approach involves filling a small measurement cell with the fluid sample and closely observing phase transitions that occur within the sample. Microscopy allows for the identification in micrometer range of distinct phases, such as liquid-liquid or liquid-vapor interfaces, and provides insights into the morphology and dynamics of phase transitions. This technique is particularly valuable for studying complex fluid systems, as it enables real-time observation of phenomena that may not be easily captured by other methods.

The use of microscopy inspection has been applied in the literature to determine wax precipitation in crude oils at atmospheric (Li et al., 2019; Paiva et al., 2017; Paso; Kallevik; Sjöblom, 2009; Soedarmo et al., 2016) and high-pressure conditions (Mmata; Onyekonwu, 2018). Furthermore, it was employed to determine the asphaltene phase envelope (Cardoso et al., 2015). To perform these high-pressure measurements, the microscope setup typically consists of a stainless-steel block with two sapphire windows opposite each other, commonly called a high-pressure microscope (HPM) cell. A light source is usually placed on one side while a camera is mounted on the opposite side, aligned with the microscope's objective lens. This arrangement facilitates the acquisition of high-quality photographs or videos, enabling researchers to capture detailed images of phase transitions and other dynamic behaviors occurring within the fluid sample.

The use of sapphire windows is particularly advantageous, as they provide excellent optical clarity and can withstand the high pressures involved in the experiments. Additionally, sapphire allows for the use of a broad spectrum of light, which is beneficial for observing various phases, including asphaltenes under infrared light. The ability to work with polarized light further enhances the setup, enabling the use of cross-polarization techniques that facilitate the observation of birefringent materials, such as waxy crystals. HPM apparatus has been widely used for different phase transition

measurements by visual inspection, such as solid-liquid, liquid-vapor, and liquid-liquid transitions (Daridon; Pauly; Milhet, 2002; Johnston A, 2017; Johnston et al., 2017; Mancilla-Polanco et al., 2019; Pauly; Coutinho; Daridon, 2010, 2012, 2007). Typically, HPM utilizes objectives with magnifications ranging from ×5 to ×50. This level of magnification enables visual inspection and the detection of particles on the order of a few micrometers. Such resolution is essential for observing the morphology of solid phases, including waxes and asphaltenes, within the fluid sample.

Some limitations of the light scattering technique are addressed using HPM fluid inspection. For example, it is possible to determine if the system is monophasic under high-pressure conditions, especially in cases where the mixture contains a high gas content. This type of information is very useful for minimum miscibility pressure tests. Nevertheless, the results obtained from the HPM fluid inspection have some limitations. For example, since only a small part of the fluid sample is observed, all the results are based on the assumption that the inspected fluid is representative of the rest of the fluid located in the high-pressure volumetric cell, even though the system may be heterogeneous. Furthermore, the fluid analyses from microscopic methods are typically static, without fluid homogenization. To address the challenge posed by the natural dark color of some reservoir fluids, certain spectrometric methods can be employed alongside those previously mentioned. At first, it is evident that methods such as light scattering, monitoring volumetric properties, and microscopic fluid inspection are complementary, as using them individually may be insufficient in some cases. Efforts have been made to achieve visibility of the dark fluid under investigation by irradiating and detecting the fluid using a light source in a range where heavy hydrocarbons exhibit low absorption. This approach enhances the clarity of the observations, allowing for better detection and analysis of the fluid's properties. By selecting wavelengths that minimize absorption by the heavy components, researchers can obtain clearer images and more accurate data regarding the fluid's phase behavior and morphology. This technique is particularly valuable in studying complex mixtures, as it facilitates the observation of liquid-liquid dispersions and the presence of small solid particles dispersed in oil.

For instance, the use of X-ray monitoring through fluid during high-pressure measurements is useful for studying the fluid phase behavior of bitumen samples (Dini; Becerra; Shaw, 2016; Zou; Shaw, 2004; Zou; Zhang; Shaw, 2007), helping to detect multiphase equilibria, such as liquid-liquid-vapor, or even dispersed phases rich in asphaltene. X-ray analysis helps to observe heavy, viscous phases formed in bitumen

systems, due to the asphaltene content, which can be confirmed through microscopic observations and compositional analysis (Dini; Becerra; Shaw, 2016).

In this same context, a visual approach was reported by Daridon et al. (2020) to investigate dark fluids. This method is based on irradiating the fluid with a light source at a wavelength in the short-wave infrared (SWIR) range and capturing the image using a specific camera that works in the same spectral range (900 to 1,700 nm). As mentioned above, heavy oils have minimal light absorption in infrared wavelengths above 1,000 nm. This approach has enabled successful observations of multiphase equilibria, including liquid-liquid, liquid-liquid-asphalt and liquid-liquid-vapor equilibria (Daridon et al., 2020; Romero Yanes et al., 2020a). One significant advantage of using the SWIR camera is their compatibility with both microscopic investigations and full-view PVT equilibrium cells. This capability allows for full visibility of the bulk fluid during classical experiments, enhancing the overall understanding of phase behavior. This visual method can improve microscopic observation or even overcome some problems with static microscope observation.

To better understand and characterize the phase transitions measured experimentally in this Thesis, a combination of all the analytical methods listed above was used to develop the experiments. In particular, light scattering techniques were applied to carry out the experiments in Chapters II and III, and the results were integrated with experimental observations using a SWIR camera coupled to a high-pressure microscope. In addition, integrating the SWIR camera into a full visibility PVT cell was used in chapters IV and V. Monitoring of volumetric behavior, i.e. p-V plots and/or Y-factor, was applied in all chapters. Combining and contrasting each method's results made constructing isopleth diagrams or *pressure-compositions* isothermal possible.

2.4   Thesis objectives

Given the high complexity of fluid phase equilibria in asymmetric mixtures such as petroleum, this Thesis was motivated by the need to understand the unconventional phase transitions observed in Brazilian pre-salt samples. The challenges associated with investigating dark samples, especially those containing asphaltenes and high gas content, further underscore the importance of pursuing of this type of research. To achieve this, the general objective of this thesis was to investigate the fluid phase

behavior of various crude oil samples from the Brazilian pre-salt with the addition of carbon dioxide and/or methane under high-pressure and high-temperature conditions.

This will be accomplished using conventional and full-visibility high-pressure equilibrium cells, along with analytical methods to detect complex phase transitions in mixtures with high gas content.

Additionally, the research will involve performing thermodynamic modeling using a classical equation of state to describe and enhance the understanding of experimentally measured multiphase equilibria.

Finally, the investigation will include a synthetic system composed of pure heavy hydrocarbons, such as polyaromatic, branched, and cyclic compounds, in combination with a gas mixture, to replicate the phase behavior observed in crude oil systems.

3 CHAPTER II: EXPLORING THE FLUID PHASE EQUILIBRIA OF A BRAZILIAN PRE-SALT CRUDE OIL BY ADDING CARBON DIOXIDE USING CONVENTIONAL PVT TECHNIQUES AND SWIR MICROSCOPIC INVESTIGATION

3.1 Introduction

This chapter presents a study of a Brazilian pre-salt crude oil recombined with carbon dioxide (CO_2). This study is motivated by the potential occurrence of a liquid-liquid (LL) phase transition under high-pressure and high-temperature conditions, as reported by Cardoso et al. (2015) and Yanes et al. (2020) for fluids with high CO_2 content. The LL transition exhibits characteristics such as high dispersion and low-density contrast. Furthermore, conventional PVT techniques show low sensitivity in detecting this type of fluid-fluid transition.

Due to the natural crude oil opacity, no ideal experimental method exists to measure all phase transitions in crude oil–gas systems. Many experimental methods are described in the literature for performing phase behavior studies, which could be categorized as direct or indirect methods. Direct visual methods such as full visual PVT investigations or high-pressure microscope (HPM) can be used for phase behavior studies involving asphaltene precipitation (Cardoso et al., 2015; Mancilla-Polanco et al., 2019; Mohammadi et al., 2015), vapor-liquid equilibrium (Daridon et al., 2020), and wax precipitation (Daridon; Pauly; Milhet, 2002). On the other hand, indirect methods can identify phase transition through fluid properties variation, e.g., light scattering (Cardoso et al., 2015; Hammami et al., 2000), X-ray analysis (Dini; Becerra; Shaw, 2016), viscosity (Shadman et al., 2012), and calorimetry scanning (Andersen; Birdi, 1991; Juyal et al., 2011). Additionally, classical PVT experiments as pressure-volume monitoring during constant mass expansion (CME) can be used for liquid to liquid-vapor transition based on compressibility variation (Daridon et al., 2020; Johnston et al., 2017; Mancilla-Polanco et al., 2019; Romero Yanes et al., 2020a). Jamaluddin *et al.* (2002) classified the

asphaltene precipitation techniques detection into five categories (gravimetric, acoustic resonance, light scattering, filtration, and high-pressure microscopy), suggesting the use of solid detection system along with isothermal depletion as a valuable tool to phase behavior studies that present asphaltene precipitation. More recently, an acoustic device has been reported as a potential technique for solid-fluid equilibria, as any structural change can affect the acoustic properties of the fluid (Carrier et al., 2000) even at high-pressure conditions (Acevedo et al., 2020; Daridon; Carrier, 2017). However, all these techniques can present advantages and disadvantages depending on the nature of the fluid and the transitions researched. For instance, using only light scattering techniques may yield erroneous results (Aquino-Olivos et al., 2001; Cardoso et al., 2015; Hammami et al., 2000). Therefore, sometimes it appears preferable to couple several experimental techniques to avoid misinterpretation of observations, especially for complex systems exhibiting multi-fluid-fluid and solid-solid equilibria. For this reason, Cardoso *et al.* (2015) and Daridon *et al.* (2020) suggested the use of combined methods with at least one visual technique.

In light of this, this chapter aims to investigate the fluid phase equilibria of a highly opaque Brazilian pre-salt crude oil–CO_2 system at different temperatures and pressures, up to 90 MPa, and to provide valuable experimental data and analysis to enhance the understanding of the system's phase behavior. A combination of direct and indirect methods supported the measurements and validated all observed phase transitions. Furthermore, this chapter focuses on examining the occurrence of a potential dispersed liquid-liquid phase equilibrium under unconventional pressure and temperature conditions, assessing their sensitivity in terms of redissolution and the ability of traditional techniques to detect the onset of such transition.

3.2 Materials and methods

3.2.1 *Crude oil sample*

A Brazilian pre-salt dead oil named BR1 was supplied by Petróleo Brasileiro S.A. (PETROBRAS). Its properties are listed in Table 1, and the compositional profile is given in Table 2, which was also provided by PETROBRAS. Phase behavior studies were carried out along isopleths by mixing a known amount of crude oil with a mass of CO_2 to reach each isopleth composition. Pure CO_2 used to formulate the systems was provided

by White Martins (Brazil) with a purity of 99.99 wt %. The following global mole compositions were investigated in this study: z_{CO_2} = (37,9, 50.0, 76.6, 80.6, and 84.2) mol %.

Table 1. Molecular weight, °API, and SARA analysis for the BR1 sample.

Properties	Value
API gravity, °API	20
Saturated ± 1, %wt	42.4
Aromatic ± 1, %wt	24.5
Resins ± 1, %wt	30.0
Asphaltene ± 1, %wt	3.16
Reservoir temperature	342.15 K
Reservoir pressure	56.94 MPa

Table 2. Compositional analysis of the BR1 oil.

Component	Mole fraction / %
C_3	0.44
i-C_4	0.23
n-C_4	0.73
i-C_5	0.58
n-C_5	0.91
C_6	2.12
C_7	4.29
C_8	5.82
C_9	5.22
C_{10}	4.63
C_{11}	4.03
C_{12}	3.60
C_{13}	4.00
C_{14}	3.30
C_{15}	3.33
C_{16}	2.76
C_{17}	2.55
C_{18}	2.64
C_{19}	2.54
C_{20+}	46.25
Molecular weight C_{20+}	638

3.2.2   Pressure-Volume-Temperature (PVT) Apparatus

Figure 5 illustrates the PVT equipment used to perform all experiments in this chapter. The apparatus consists of a Fluid-Eval PVT cell (Vinci Technologies, France) with a high-pressure measurement cell equipped with a variable volume pump, allowing precise control of system volume and pressure with standard uncertainties of $u(V) = 0.01$ mL and $u(p) = 0.1$ MPa, respectively. This experimental setup has maximum operational conditions of 100.00 MPa for pressure, 1000 mL for volume, and 473.15 K for temperature. The cell head has a sapphire window that allows visualization of the fluid inside. It also contains a magnetic stirrer to ensure sample homogenization.

The top of the measurement cell integrates a solid detection system called NIR-SDS, based on a light scattering method working in the near-infrared. This device has a laser source that produces the signal, which passes through the fluid thanks to two sapphire windows. The sample's transmittance was analyzed at a constant wavelength (1,500 nm) using an optic transmission probe with a minimal sensibility of 1 pW.
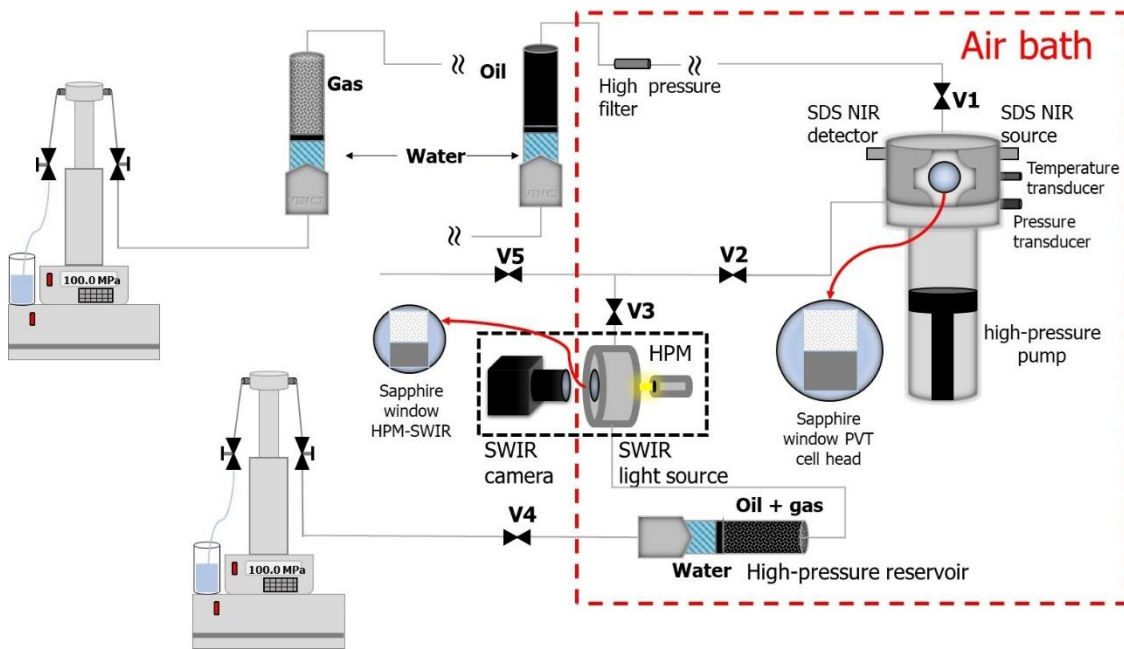
Figure 5. Schematic PVT apparatus, high-pressure microscope SWIR, and sample injection ensemble. (Created by the author)

The experimental setup also includes a high-pressure microscope (HPM) formed by an external cell with two sapphire windows facing each other and separated

by 100 μm. This additional device is positioned between the measuring cell and a variable-volume reservoir tank, as shown in Figure 5. This configuration enables the mixture to flow through the HPM cell. This continuous change of the fluid sample observed by microscopy is necessary to observe the sample representative of the fluid inside the PVT cell. The sapphire windows of the HPM cell are positioned between a light source and a short-wave infrared (SWIR) camera that is used to improve the observation of opaque mixtures. The SWIR apparatus allows fluid inspection at a wavelength where crude oil exhibits minimal light absorbance (Daridon et al., 2020). Therefore, any phase transition that causes SWIR light diffraction can be observed in a high-pressure microscope, especially for liquid-liquid equilibria. An objective lens with a magnification of 5x was used along with the SWIR camera. This assembly for microscopic observation is called HPM-SWIR in the schema of Figure 5. The whole equipment is enclosed in a thermoregulated oven to guarantee the thermal homogeneity of the fluid in all the devices used. The fluid temperature inside the PVT cell was measured by a thermocouple located at the cell head with a standard uncertainty of $u(T) = 0.1$ K.

3.2.3   Sample preparation

A synthetic static method was applied in this chapter (Dohrn et al., 2024). This method makes it possible to prepare a mixture where the global composition is known rather than the composition of each phase. Samples preparation began with a vacuum step for the PVT cell. Next, nearly 80 cm^3 of crude oil was carefully injected at a pressure above saturation pressure and T = 333.15 K using a high-pressure transfer cylinder and a high-pressure syringe pump (Teledyne Isco 260D) with a resolution of 0.01 cm^3. The exact amount of BR1 injected was determined using an analytical scale (Sartorius MSU5203P) with an accuracy of ±0.005 g. Then, the required amount of CO_2 was injected under pressure using a syringe pump (Teledyne Isco 260D). The volume of gas transferred was obtained by measuring the volume displacement of the syringe pump. The temperature and pressure of the gas were monitored during the injection to determine CO_2 density under transfer conditions and therefore to transform transfer volume in injected amount. For that purpose, the density of carbon dioxide was taken from the NIST database (Linstrom; Mallard, 2001). With this preparation method, the resulting expanded (k=2) combined uncertainty in the global mole fraction $U_c(z_{CO_2})$ was estimated to be

lower than 0.24 mol % using the equation provided in Appendix I. When both crude oil and CO_2 were introduced into the cell, the system was pressurized under continuous stirring (750 rpm) at a rate of 0.4 MPa·min^{-1} to reach the highest pressure of the study for the considered isopleth. At this pressure, the system can be in a single-phase or two-liquid phase equilibrium, depending on the feed composition of the system. The mixture was maintained for at least 10 h under this condition to ensure thermodynamic equilibrium before starting experiments.

3.2.4   *Constant Mass Expansion (CME) and Constant Mass Cooling (CMC) Tests*

Constant mass expansion (CME) experiments were carried out using a successive programmed depletion ramp, called continuous depletion, followed by a mid-ramp hold, the equilibrium step. The depletion ramp rate was fixed at 0.4 MPa·min^{-1} with continuous stirring to maintain the system equilibrium during pressure changes. The mid-ramp hold is a several-minute isobaric portion at a target pressure. During this pressure plateau, the stirring was turned off for 15 minutes. At this point, three equilibrium criteria were established: i) no pressure variation greater than 0.03 MPa; ii) No volume change greater than 0.05 cm^3; and iii) no temperature variation higher than 1.0 K. Once these criteria for 5 minutes are achieved, pressure, temperature, volume, and NIR-SDS signal values were recorded using AppliLab® software acquisition and plotted as a function of pressure. Finally, the system was visually inspected through the sapphire window to observe the appearance of a new phase. The transition pressures were determined from all the data recorded during the equilibrium steps in the CME. It is important to mention that the saturation pressure was identified using indirect and direct techniques. Firstly, from the compressibility change observed on the pressure-volume (PV) curve. Once saturation pressure was determined, the relative volume was calculated by the ratio between the mixture volume obtained by the PVT measurement cell and saturation volume (V/V^{sat}). Secondly, it is based on NIR-SDS signal drop. Finally, through direct observation via the sapphire windows at the PVT cell head. Using this method, the expanded uncertainty determined by using the *PV* curve and NIR-SDS signal was calculated to be $Uc_{(PV\ curve)} = \pm\ 0.59$ MPa and $Uc_{(NIR\text{-}SDS)} = \pm\ 0.59$ MPa at a confidence level of 95 %, respectively.

Constant mass cooling (CMC) was also conducted at fixed pressures to determine phase transition temperatures by temperature scanning when the slope of the phase envelope is too high in the p,T diagram. In this isobaric test, the sample is cooled by successive programmed temperature rate 0.05 K·min^{-1} followed by isothermal equilibrium steps. Similar to CME experiments, pressure, temperature, volume, and NIR-SDS signal values were recorded at each equilibrium step and then plotted as a function of temperature to detect phase change temperature. During this process, expanded uncertainty determined for the phase transitions during the CMC test was calculated to be $Uc_{(CMC)} = \pm\, 0.48$ K at a confidence level of 95 %.

3.2.5 High-pressure microscope SWIR (HPM-SWIR) tests

The high-pressure microscope was used to characterize the observed phases at the microscopic scale and confirm phase transition determined by results obtained in CME and CMC tests. Since a volume of approximately 8.0 cm^3 is required to fill the capillary line between the PVT cell head and the high-pressure reservoir (see Figure 5) a 20 cm^3 fluid sample was displaced from the PVT cell head to guarantee the representativity of the sample. The NIR-SDS signal before and after the HPM- SWIR procedure must be compared to ensure that the fluid sample in the HPM cell presents the same global composition as those of the main PVT cell. Depleting and cooling experiments in the HPM-SWIR were performed at the same conditions as the CME and CMC tests.

Data acquisition software records all observations during the HPM-SWIR tests as well as the pressure, temperature, and NIR-SDS signal in the main PVT cell. Additionally, the SWIR camera integrated into the HPM captures photo frames with a resolution of 640 x 512 pixels. Phase transition is observed when particle sizes, whether liquid or solid, are greater than 40 μm during fluid inspection within the HPM-SWIR. Expanded uncertainty for phase transition observed during CME and CMC in HPM-SWIR was calculated to be $Uc_{(HPM\text{-}SWIR)} = \pm\, 0.65$ MPa and $\pm\, 0.48$ K at a confidence level of 95 %, respectively.

3.3 Results and discussions

The fluid phase behavior of BR1 – CO_2 was determined based on 4 isoplethic measurements. Table 3 lists the results concerning phase transition measurement in the temperature range from 313.15 to 423.15 K for different BR1 – CO_2 pseudo-binary system mixtures.

Table 3. Phase transition data for BR1 – CO_2 systems.[a]

T / K	P / MPa	Transition	T / K	P / MPa	Transition
z_{CO_2} (mol %) = 37.9 ± 0.24			z_{CO_2} (mol %) = 76.6 ± 0.25		
313.15	3.63	vapor-liquid	329.4	89.63	liquid-liquid[b]
333.15	4.08	vapor-liquid	330.6	75.84	liquid-liquid[b]
353.15	5.08	vapor-liquid	335.95	55.16	liquid-liquid[b]
373.15	5.94	vapor-liquid	353.15	42.83	liquid-liquid[b]
393.15	6.93	vapor-liquid	373.15	36.30	liquid-liquid[b]
			393.15	36.06	vapor-liquid[b]
			373.15	41.09	liquid-liquid[c]
			353.15	49.73	liquid-liquid[c]
			331.95	89.63	liquid-liquid[c]
			326.15	48.26	solid-liquid-liquid[c]
			327.25	89.63	solid-liquid-liquid[c]
z_{CO_2} (mol %) = 50.0 ± 0.18			z_{CO_2} (mol %) = 80.6 ± 0.16		
313.15	6.06	vapor-liquid	351.25	89.63	liquid-liquid + asphaltene[b]
333.15	7.76	vapor-liquid	354.67	75.84	liquid-liquid + asphaltene[b]
353.15	9.79	vapor-liquid	373.15	55.36	liquid-liquid + asphaltene[b]
373.15	11.31	vapor-liquid	393.15	49.16	liquid-liquid + asphaltene[b]
393.15	12.88	vapor-liquid	413.15	45.67	liquid-liquid + asphaltene[b]
			413.15	47.97	liquid-liquid + asphaltene[c]
			393.15	54.58	liquid-liquid + asphaltene[c]
			373.15	65.68	liquid-liquid + asphaltene[c]
			363.15	72.48	liquid-liquid + asphaltene[c]

[a]Standard uncertainty u are $u(T)$ = 0.1 K, $u(P)$ = 0.1 MPa; [b]Phase equilibrium determined by NIR-SDS signal; [c]Phase equilibrium observed during HPM-SWIR fluid inspection.

Figures 6a and 6b present the volumetric change and the transmitted light intensity through the NIR-SDS device recorded during the CME tests at 373.15 K for BR1 – CO_2 mixtures with z_{CO_2} = (37.9 and 50.0) mol %. The relative volume was used to

standardize all the graphs in this chapter. Similar trends were observed for all temperatures investigated in low CO_2 content mixtures. Typical black oil *pressure-relative volume* curves (*p-V* curve) that exhibit a sharp change in compressibility at bubble point pressure were found for such compositions. Therefore, the transition pressures were easily determined by noting the break in the slope curve of the *p-V* curves. Moreover, bubbles in the liquid phase cause light scattering and lead to a sharp drop in the NIR-SDS signal (Hammami et al., 2000). It can be seen in Figures 6a and 6b that the bubble point pressures probed by the SDS method coincide perfectly with those determined by the PV method. For both these mixtures with low CO_2, the experiment only shows liquid (L) to vapor-liquid (VL) transitions. The results were plotted as a function of temperature in Figure 7, which shows that the bubble point pressure increases with temperature in the investigated domain.
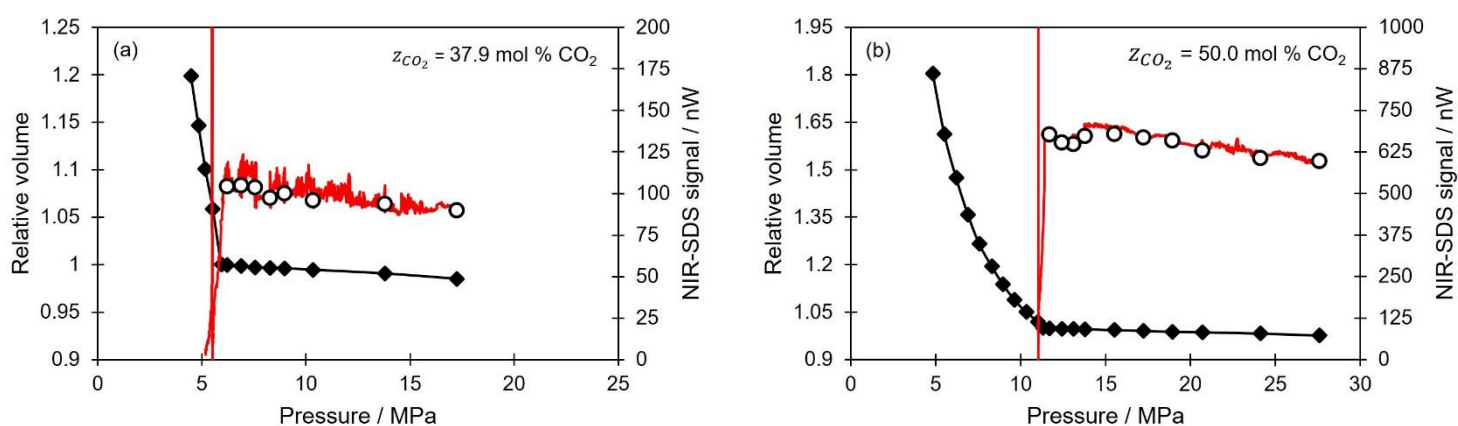
Figure 6. Pressure-relative volume curve (♦, black diamond), and SDS light transmittance intensity (○, circles) recorded during CME experiment carried out at 373.15 K in BR1 – CO_2 mixtures. (a) z_{CO_2}= 37.9 mol %; (b) z_{CO_2}= 50.0 mol %.
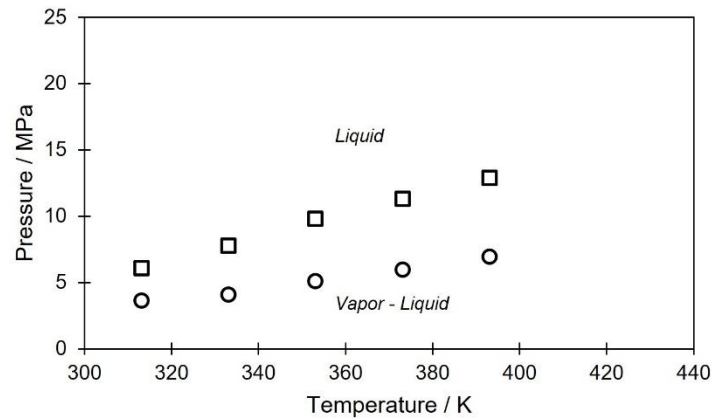
Figure 7. Phase diagram for BR1 – CO_2 mixtures with several feed compositions. L → VL transition for z_{CO_2} = 37.9 mol % (○, circles) and z_{CO_2} = 50.0 mol % (□, square).

The phase diagram for crude BR1 – CO_2 (z_{CO_2}= 76.6 mol % CO_2) is shown in Figure 8. For this mixture, the phase diagram was built by combining the results obtained during CME, CMC, and HPM-SWIR investigations. A liquid-liquid equilibrium (LLE) domain was observed above the critical temperature of CO_2. This mixture's pressure-temperature (*p,T*) projection is similar to a type III diagram, following the classification proposed by van Konynenburg and Scott (1980) for binary systems. Generally, LL immiscibility in systems with *n*-parafins or crude oil – CO_2 occurs at temperatures near or below the critical temperature of CO_2, where the miscibility of carbon dioxide in hydrocarbons is limited, and CO_2 could exist pure in a liquid phase. This behavior has been reported in the literature for some crude oil samples (Larson et al., 1989; Orr; Jensen, 1984; Orr; Yu; Lien, 1981). However, for this third composition investigated, the coupling of different techniques revealed a liquid-liquid (LL) phase equilibrium around *T* = 373 K and below.

During fluid inspection using HPM-SWIR, a common L → VL transition was observed with system depletion at 393 K, marked by typical gas bubbles arising from the liquid phase, which causes the SWIR light dispersion. In addition to fluid-fluid transitions, the formation of waxy solid crystals was detected during fluid inspection in HPM-SWIR. A solid-liquid-liquid region was observed beginning at a temperature of *T* = 326 K. The *p,T* projection of this isopleth is comparable to those observed for asymmetric heavy *n*-alkanes + CO_2 systems reported in the literature (Braga; Tavares; Ndiaye, 2022; Daridon et al., 2021; Yanes; Montel; Daridon, 2022a) but the L→ LL

transition occurs at lower temperatures as illustrated in Figure 9. The NIR-SDS technique detected the L → LL phase transition at a temperature below the visual observation provided by HPM-SWIR. This difference can be attributed to the intensity and sensitivity of the techniques. This LLE was marked by forming a dispersed liquid phase that presents a low coalescence in equilibrium with a continuous phase. When dispersed LLE was observed inside HPM-SWIR, NIR-SDS detected no major laser scattering. This behavior can suggest that dispersed LL presents a low contrast in phase density at high-pressure conditions. Nevertheless, the light scattering technique indicates a new phase formation at pressure conditions lower than the conditions observed in HPM-SWIR. This observation of complex phase transitions underscores the importance of combining different techniques for studying complex fluid phase equilibria. It highlights the advantage of visual methods such as HPM-SWIR inspection capable of detecting micrometric dispersions.
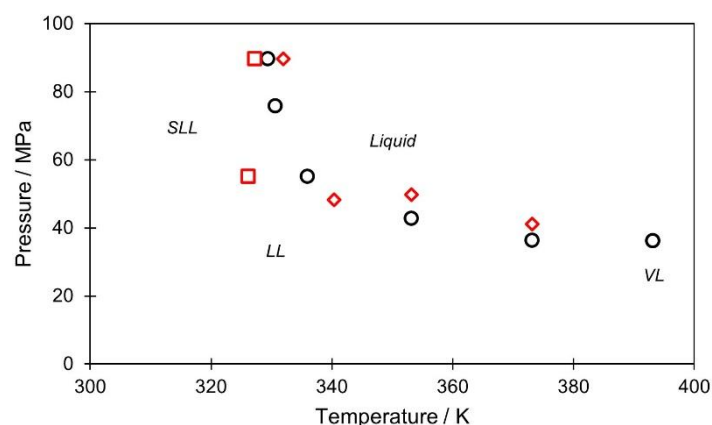
Figure 8. Phase diagram for BR1 – CO_2 (z_{CO_2} = 76.6 mol %) system. Vapor-liquid (VL) and fluid-fluid (LL) transition determined by NIR-SDS signal (○, circles); fluid-fluid transition (◊, red diamond) and solid-fluid-fluid (SLL) transition (□, red square) observed during HPM-SWIR inspection.
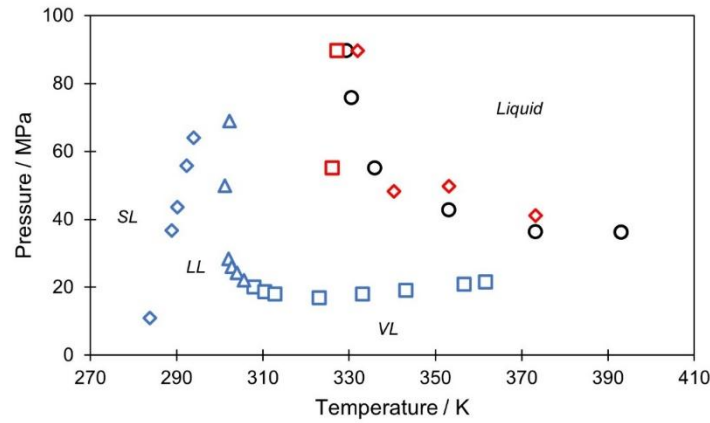
Figure 9. Isopleth phase diagram comparison with VL and LL regions for heptadecane + CO_2 (z_{CO_2}= 85.02 mol %) (blue symbols) and BR1 – CO_2 (z_{CO_2}= 76.6 mol %) (black and red symbols) mixtures.

Figure 10 depicts the results of CME tests at T = (353.15, 373.15, and 393.15) K and direct observation at the PVT cell head for the BR1 – CO_2 (z_{CO_2}= 76.6 mol % CO_2) system. A continuous shape for the PV curve with no change slop is observed at all temperatures investigated as pressure decreases. This result is similar to those reported for medium crude oil (25 < °API < 31) with a high gas content (Romero Yanes et al., 2019a, 2021c) and could be due to either a minimal contrast between properties of fluid phases in equilibrium just below the transition or a slow formation of the second fluid phase, which makes changes in the physical properties of the global system very smooth. In this case, the PV method is not valuable for measuring the condition of phase change. As shown in Figure 10, the NIR-SDS signal continuously increases during the beginning of fluid depletion in the CME experiment. This trend is correlated to a monotonous decrease in mixture density. When the liquid phase splits into two fluid phases, the light absorbance of the system sharply increases due to light dispersion, and the intensity of the received signal significantly decreases. Consequently, this drop in the NIR-SDS signal may serve as an indirect indicator of the formation of a new phase. However, this appearance must be confirmed by a visual inspection of the cell head or by HPM-SWIR to be validated. The L → LL transition curve for BR1 – CO_2 (z_{CO_2}= 76.6 mol % CO_2) exhibits a significant slope in the p,T phase diagram, making its detection imprecise by CME experiments, and, consequently, CMC appears to be more suitable. Therefore, CMC tests were carried out at p = (55.16, 75.84, and 89.63) MPa to determine saturation

temperature and map the full phase diagram in the pressure range of investigation. Only the NIR-SDS signal was used to identify phase transition in such conditions. Similar to CME tests, NIR-SDS signal drops when the phase transition occurs, as shown in Figure 11.
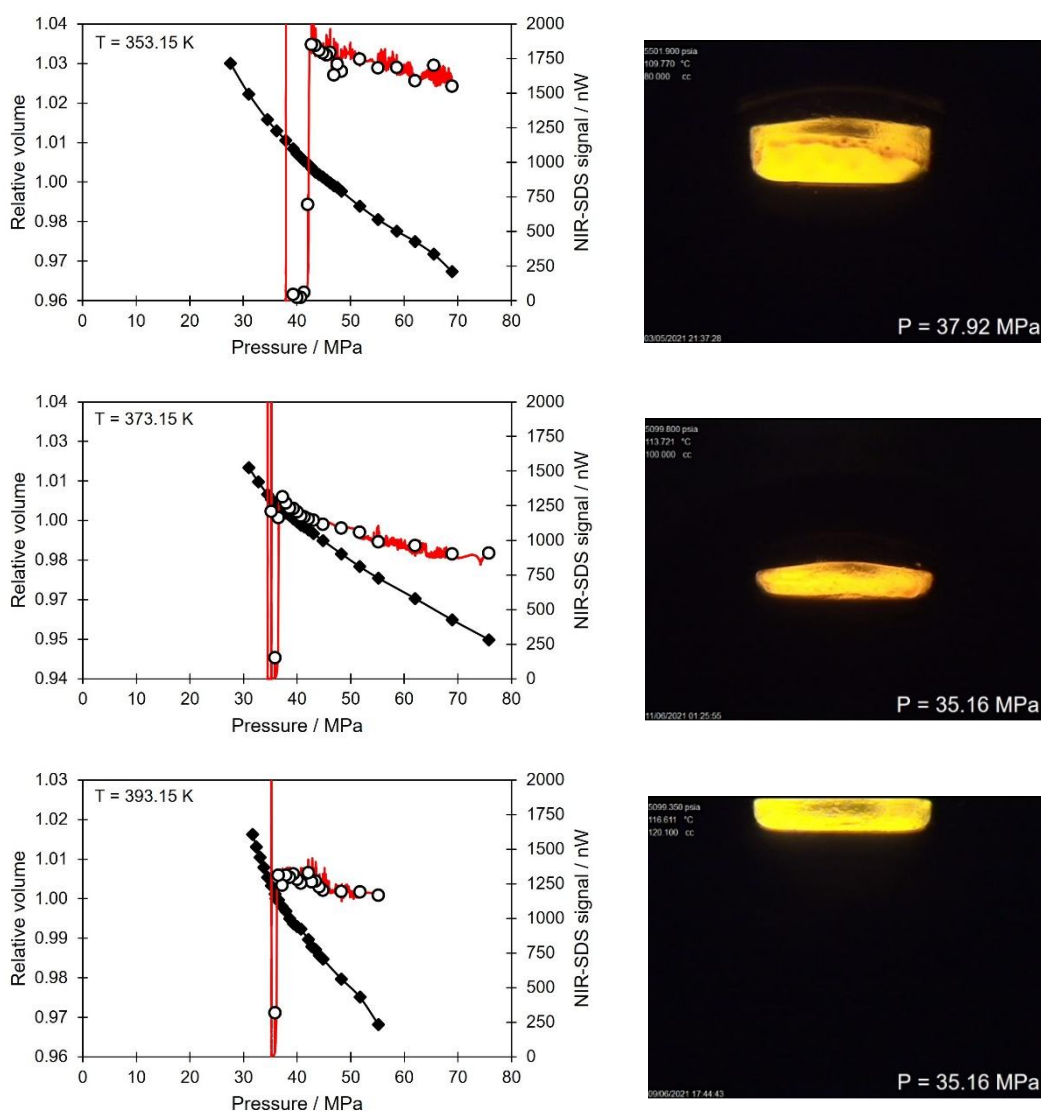
Figure 10. Volumetric behavior for BR1 – CO_2 (z_{CO_2} = 76.6 mol % CO_2) at T = (353.15, 373.15, and 393.15) K. Left: Pressure-relative volume curve (♦, black diamond), and NIR-SDS light transmittance intensity (○, circles); right: fluid inspection through sapphire in the PVT cell head.
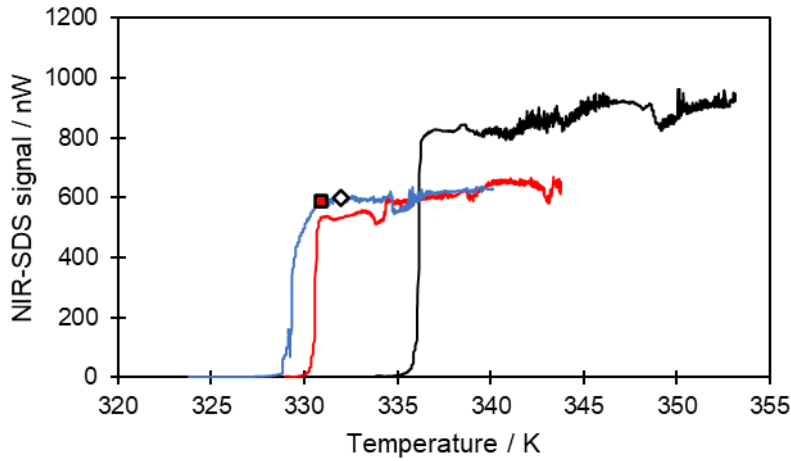
Figure 11. NIR-SDS light transmittance intensity during CMC for BR1 – CO_2 ($z_{CO_2}=$ 76.6 mol %) at p = [55.16 (—, black line), 75.84 (—, red line), and 89.63 (—, blue line)] MPa against temperature. Liquid-liquid detected by HPM-SWIR (◊, diamond) and phase transition detected by NIR-SDS (■, red square).

Figure 12 illustrates fluid inspection by using the HPM-SWIR. At high pressure, a monophasic liquid was observed in all temperature domains. When the mixture was depressurized at T = 393.15 K, a simple L → VL transition was observed at 36.00 MPa, characterized by bubbles rising and growing from bulk fluid and causing SWIR light diffraction. This phase transition occurs at pressure conditions near saturation pressure indicated by the NIR-SDS signal (Figure 10).
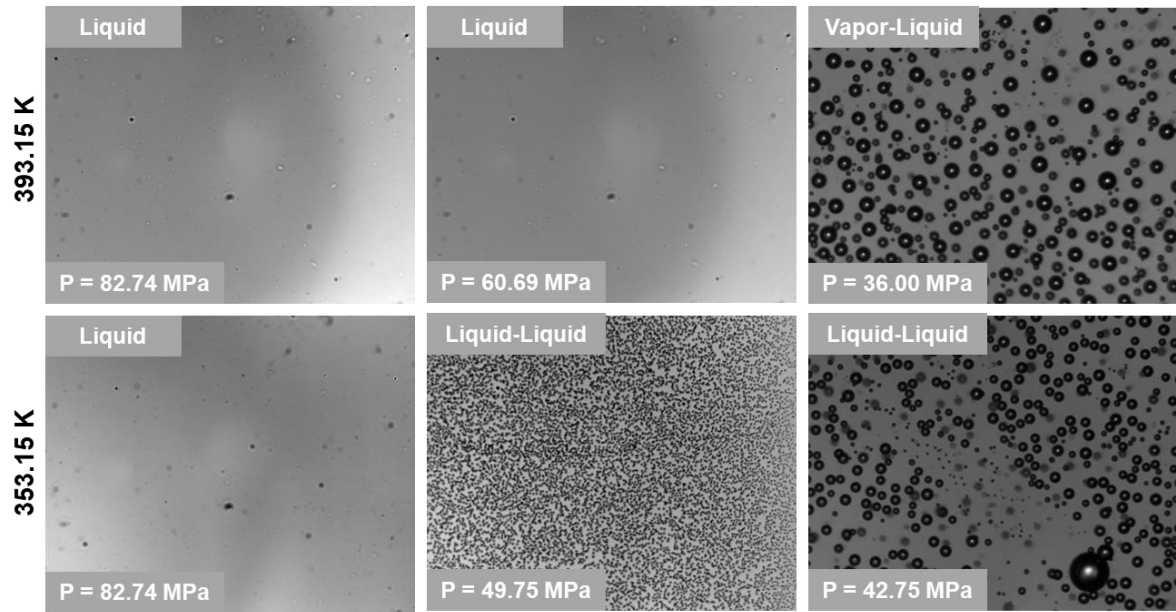
Figure 12. Fluid inspection using HPM-SWIR for BR1 – CO_2 (z_{CO_2} = 76.6 mol % CO_2) during fluid depletion at T = (393.15 and 353.15) K. Photo frame using a magnification of 5x.

During fluid depletion at T = 353.15 K, a fluid-fluid phase separation was first observed with the formation of small drops, which remain stable in the HPM cell if the pressure is maintained at a constant value just below the transition pressure. Observation of the PVT cell's head under the same conditions does not show phase segregation with time due to gravity. On the other hand, these drops grow when the pressure is lowered and continuously transform to form unstable bubbles at lower pressure. Identifying the exact nature of the fluid-fluid transition under these conditions is difficult. However, the continuous evolution of the dispersed phase from droplet (liquid) to bubble (vapor) nature leads us to call it liquid to liquid-liquid transition. From this CO_2 content, it can be stated that CO_2 becomes partly miscible in the BR1 sample even at much higher temperatures than the critical temperature of CO_2. Returning to Figure 10, it can be noticed that the NIR-SDS signal does not show enough sensibility to identify the onset of the L to LL transition. Therefore, the NIR-SDS signal indicates a phase transition only when LLE is more evident. The lack of sensitivity of the NIR-SDS signal for LL transition can be attributed to the similar density of liquid phases in equilibrium. This result is qualitatively consistent with findings from other Brazilian pre-salt crude oil samples (Romero Yanes et al., 2020a) when recombined with a high CO_2

amount. In the literature, the LLE observed for crude oil–CO_2 are usually related at temperature conditions near to CO_2 critical temperature and is characterized by an oil-rich phase and another CO_2-rich phase (Eghbali; Dehghanpour, 2017; Lindeloff et al., 2013; Orr; Yu; Lien, 1981). Moreover, the CO_2-rich phase may present a capacity to solubilize some heavy hydrocarbons in the oil-rich phase (LARSON et al., 1989), resulting in liquid phases with similar densities.

To confirm the phase transition indicated in Figure 11, CMC tests were carried out using the HPM-SWIR visualization method, and photos of the observed samples are shown in Figure 13. During isobaric cooling at $p = 89.63$ MPa, an L→LL transition was observed at $T = 331.95$ K. This transition is marked by a diamond sign (◊) in Figure 11. L→LL transition occurred in a temperature condition slightly above the point where the NIR-SDS signal sharply dropped, supporting that both liquid phases probably have similar volumetric and optic properties (Al Ghafri; Maitland; Trusler, 2014; Okuno; Xu, 2014; Orr; Yu; Lien, 1981). However, when the temperature reached $T = 327.25$ K, second liquid drops were observed with a larger size than at $T = 331.15$ K. This observation is marked in Figure 11 with a squared sign (■) and occurs when NIR-SDS signal starts to detect changes in the bulk fluid. In addition, when the system temperature reached a temperature of $T = 327.25$ K, a waxy solid phase appeared in addition to LLE. Similarly, the CMC test at $p = 48.26$ MPa presents an L→LL transition and a paraffinic phase when the system temperature equals $T = 326.15$ K. In this last case, the waxy crystals were more evident as their appearance conditions were more distant from those of the transition of the two liquid phases.
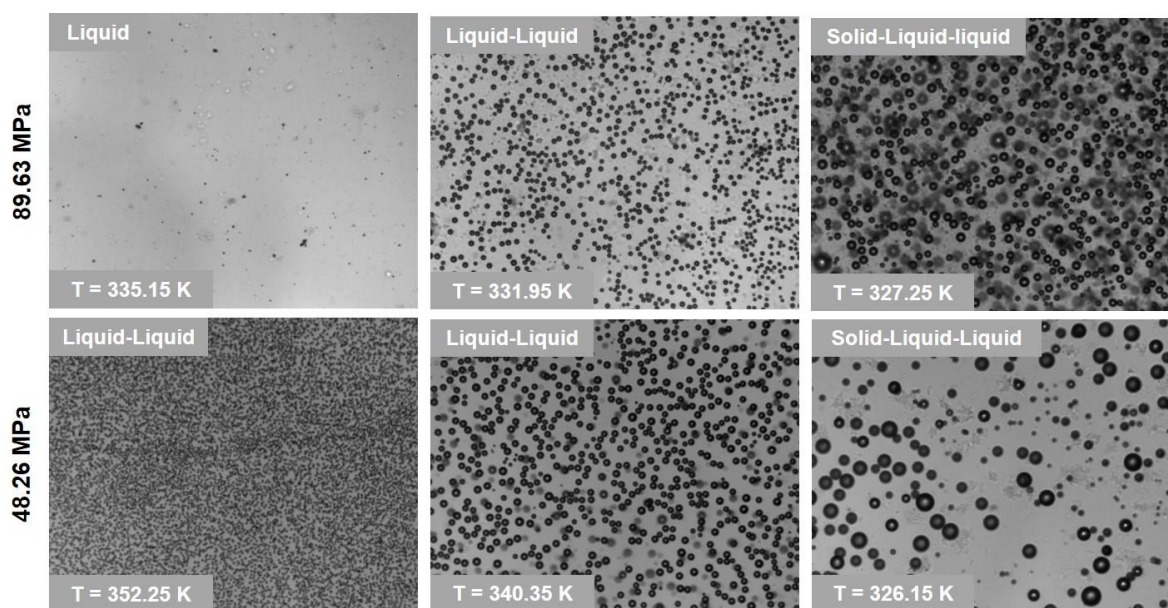
Figure 13. Fluid inspection using HPM-SWIR for BR1 – CO_2 (z_{CO_2}= 76.6 mol % CO_2) during isobaric cooling at p = (89.63 and 48.26) MPa. Photo frame using a magnification of 5x.

The following BR1- CO_2 mixture under study corresponds to a CO_2 content of 80.6 mol%. The phase diagram for this mixture is shown in Figure 14. As can be seen in the p,T diagram, adding 5 mol% gas to the previous mixture results in a shift of the phase envelope towards high pressure and high temperature, which can be attributed to an increase of the system asymmetry caused by the excess of carbon dioxide in the mixture. Consequently, this system would never be monophasic under reservoir conditions around T = 342 K and p = 57 MPa. In this composition, the excess CO_2 destabilized the asphaltene fraction, which was observed even at the highest temperature investigated.
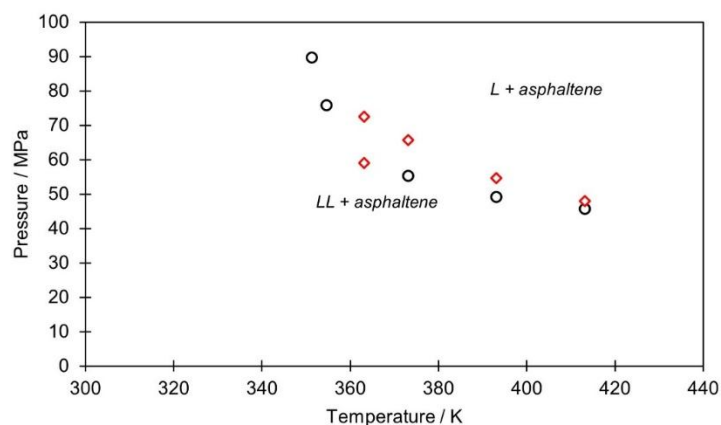
Figure 14. Phase diagram for BR1 – CO_2 (z_{CO_2} = 80.6 mol % CO_2) system. Fluid-fluid transition determined by the NIR-SDS signal (○, circles); Fluid-fluid transition (◊, red diamond) observed during fluid inspection using HPM-SWIR.

Figure 15 depicts the volumetric behavior and NIR-SDS signal recorded for the 80.6 mol% CO_2 mixture during the CME tests at T = (373.15, 393.15, 413.15) K along with the direct observation through the sapphire window in the PVT cell head. Based on this figure, it is observed that the SDS probe exhibits a different behavior depending on whether the signal is recorded continuously with the stirrer in action or on an equilibrium step when the system stirring is turned off. This difference is caused by particles settling. When the stirrer is stopped at the beginning of the equilibrium plateau, there is an instantaneous increase in the intensity measured by the SDS probe, as indicated by the vertical red lines in Figure 15. This increase in the SDS signal reflects a decrease in the absorbance of the fluid due to the particles settling in the fluid. This implies that the fluid is never homogeneous under the conditions of the experiment, even at the higher pressure corresponding to the beginning of the CME test. The rapidity of the settling phenomenon suggests a significant difference between the densities of the dispersed and continuous phase, which is not compatible with a fluid-fluid dispersion but with a dispersed solid in an oil system. As this phenomenon is observed at all temperatures, it is concluded that the solid is not a wax. Therefore, this dispersion is assigned to unstable asphaltenes (A) (Acevedo et al., 2020; Cardoso et al., 2014; Romero Yanes et al., 2021b, 2021c; Zou; Shaw, 2004) destabilized by CO_2, which acts as an anti-solvent for asphaltenes.
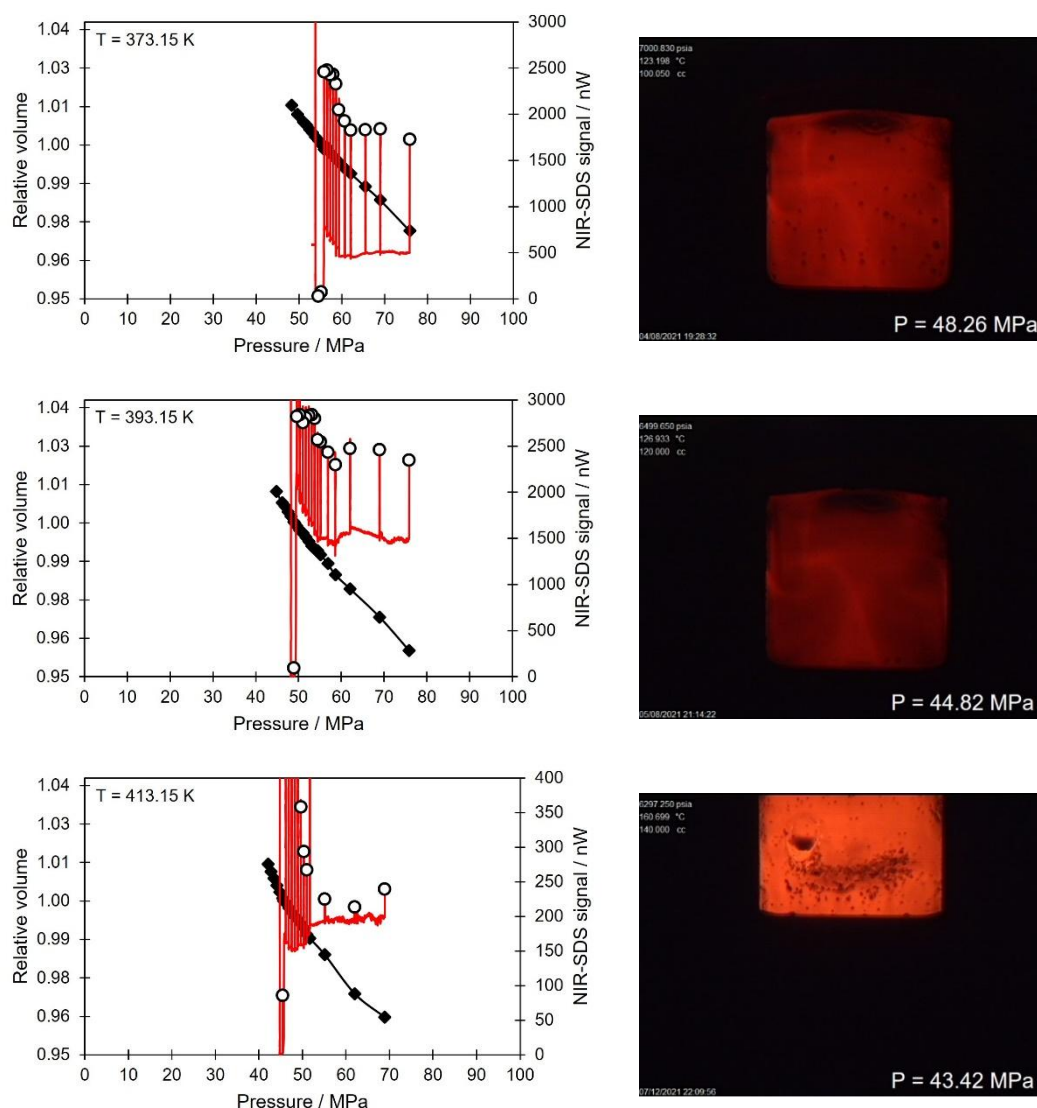
Figure 15. Volumetric behavior for BR1 – CO_2 (z_{CO_2} = 80.6 mol % CO_2) at T = (373.15, 393.15, and 413.15) K. Left: Pressure-relative volume curve (♦, black diamond), and NIR-SDS light transmittance intensity (○, circles); right: fluid inspection through sapphire in the PVT cell head.

Figure 16 depicts fluid inspection by using HPM-SWIR for BR1 – CO_2 (z_{CO_2} = 80.6 mol %) at T = (373.15, 393.15, and 413.15) K. Firstly, at high-pressure conditions it was observed asphaltenic flocs that confirm the conclusions drawn from SDS results. These flocs present a fractal morphology (Mohammadi et al., 2015) and a high preference for sticking on the sapphire window surface. Asphaltene flocs adsorb on the sapphire window because of superficial charges from Lewis acid-base, Bronsted base, and superficial hydroxyl groups (Cardoso et al., 2015). By comparing the pictures taken

at different temperatures but at the same high pressure (82.74 MPa), it can be noted that there is a difference in the densification of the number of asphaltene flocs, which shows that the temperature has here a stabilizing effect on the asphaltenes in the mixture. In qualitative terms, images obtained via high-pressure microscopy reveal that a portion of the asphaltenes redissolve as the temperature increases, suggesting that this mixture has a lower critical solution temperature (LCST) around these pressure and temperature conditions. Secondly, an LA $\rightarrow$ LLA transition was observed during HPM-SWIR fluid inspection for all isotherms investigated. As for the previous mixture, the NIR-SDS signal does not show sensibility enough to detect L$\rightarrow$ LL transition. The transition pressure value determined by this method always appears to be well below that determined by direct observation under the microscope. This confirms that SDS is poorly suited to detect this fluid-fluid transition or phase changes in multiphase systems. As the system studied in this chapter exhibits a complex multiphase behavior involving waxes, asphaltenes, and liquid-liquid dispersions, they can be best studied by high-pressure microscopy, particularly when combined with a SWIR camera. Furthermore, in this configuration, it is possible to work with high-magnification lenses that allow the observation of dispersed phases at the micron scale. Therefore, it will enable us to distinguish between wax, asphaltene or liquid dispersion despite the high opacity of the oil.
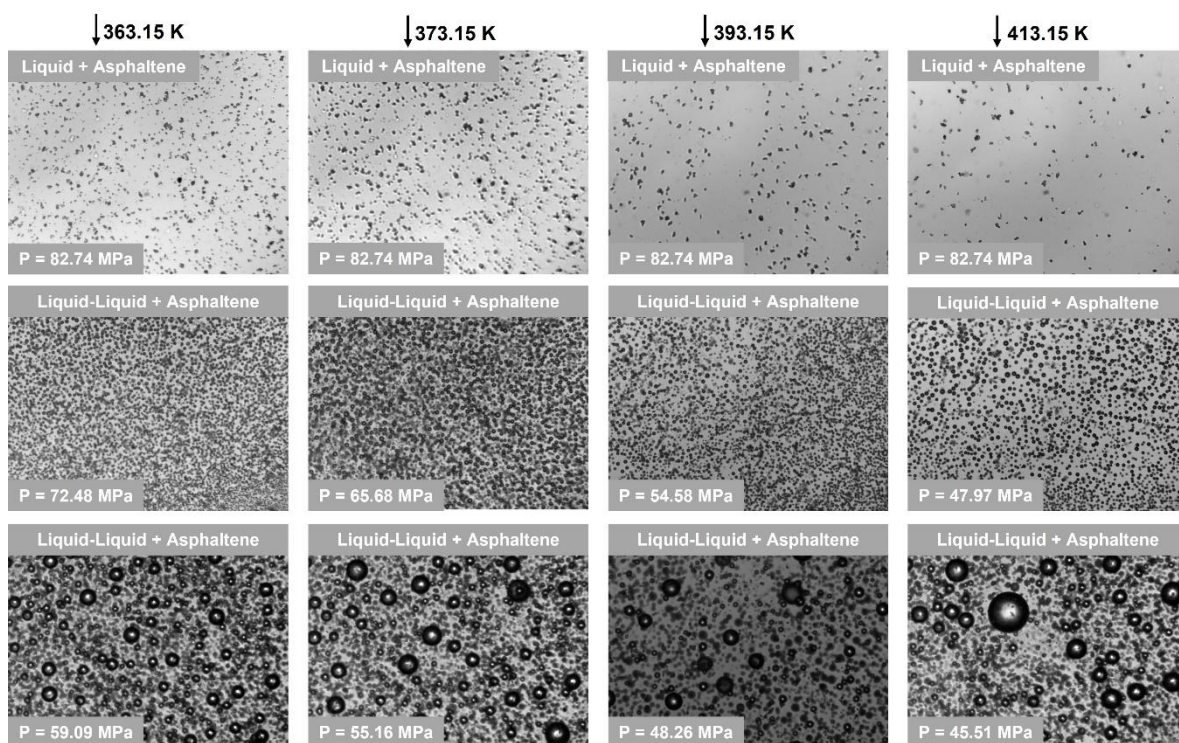
Figure 16. Fluid inspection using HPM-SWIR for BR1 – CO_2 (z_{CO_2} = 80.6 mol %) during fluid depletion at T = (363.15, 373.15, 393.15, and 413.15) K. Photo frame using a magnification of 5x.

An additional composition was prepared to complete the fluid phase behavior study of BR1 – CO_2 with a CO_2 content of 84.2 mol %. However, even under T = 413.15 K and p = 89.63 MPa conditions, a monophasic region was not obtained for this composition. Instead, a multiphase equilibrium was observed similar to the BR1 – CO_2 (z_{CO_2} = 80.6 mol %) system, which exhibited a liquid-liquid equilibrium in addition to asphaltenic flocs, revealing that the system in such high CO_2 content appears as a three phase liquid-liquid-asphalt equilibrium. Figure 17 shows the relative volume and SDS intensity recorded during the CME carried out at T = 373.15 K and the photo frame obtained by fluid inspection using the HPM-SWIR device. This figure shows that the SDS signal and the HPM observation reveal a heterogeneous system at this HT-HP condition. Furthermore, a change in the SDS signal can be observed when the pressure decreases below 70 MPa, with a sharp drop in the recorded light intensity. This behavior can be attributed to a change in the volumetric properties of the dispersed fluid phase, which change continuously from droplet-like to bubble-like in this domain (Larson et al., 1989).
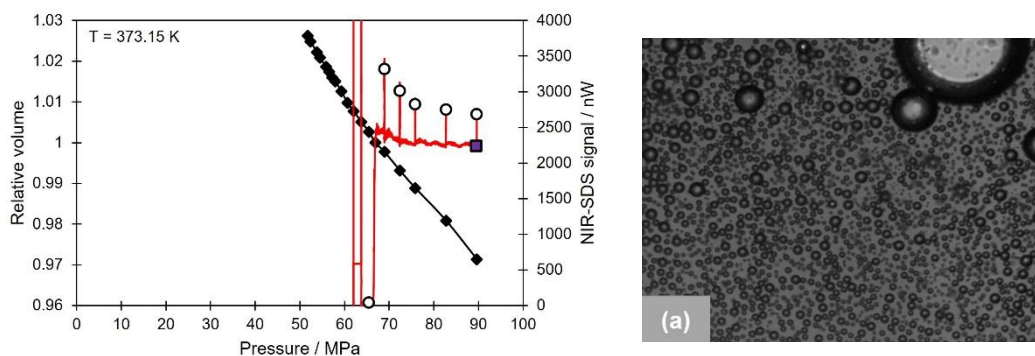
Figure 17. Volumetric behavior for BR1 – CO_2 (z_{CO_2} = 84.2 mol % CO_2) at T = 373.15 K. Pressure-relative volume curve (♦ black diamond), and NIR-SDS light transmittance intensity (○ circles); right: (a) LLE observation at T = 373.15 K and 89.63 MPa by using HPM-SWIR for BR1 – CO_2 (z_{CO_2} = 84.2 mol %).

3.4 Conclusion

Fluid phase equilibria of highly opaque Brazilian pre-salt crude oil were studied by adding CO_2 in four isopleth measurements. Different phase transitions were experimentally measured using indirect detection techniques and direct visualization methods, such as *pressure-volume* curves, light scattering, fluid inspection in HPM-SWIR, and observation at the PVT cell head. The LL equilibrium observed appeared as an LL dispersion at high pressure with a slight contrast in volumetric and optical properties between both phases, challenging the detection of the transition from L to LL by indirect techniques. Indeed, the traditional *pressure-relative volume* curve method has proven ineffective, as it failed to detect the change in compressibility associated with the transition. In contrast, the method based on monitoring the amplitude of a light beam passing through the SDS device can successfully identify the transition from L to LL during constant mass expansion. However, the application of this method is limited, as it only detects transitions at pressures lower than the actual pressure thresholds associated with the phase change. The high-pressure microscopy working in a particular range of infrared wavelengths (SWIR) allows for easy observation of liquid-liquid phases split as well as the appearance or presence of solid phases of wax or asphaltene type within a single liquid phase or even two liquid-liquid phase equilibria. It confirms that evaluating such complex phase behavior involving multi-phase equilibria requires coupling

experimental techniques that can operate at different scales. However, the real nature of this dispersed liquid-liquid equilibrium was not fully understood, mainly because of its occurrence in very high-pressure and high-temperature conditions. Therefore, this behavior will be studied in the following chapters of this Thesis.

4 CHAPTER III: ASSESSMENT OF FLUID PHASE EQUILIBRIA OF HIGH-CO₂ RESERVOIR FLUIDS

4.1 Introduction

In phase behavior studies, a practical approach is to recombine pure gas with a dead crude oil sample to observe the influence of gas addition until the gas-oil ratio (GOR) of the reservoir sample is reached or to recombine the crude oil sample with a complex gas mixture to replicate the behavior of live oil. In the case of Brazilian pre-salt samples, it is imperative to understand the effect of each gas added, as the live oil in these samples generally exhibits a high gas-oil ratio, mainly due to methane (CH_4) and carbon dioxide (CO_2). In Chapter II, the phase behavior of a highly opaque crude oil sample was studied by adding carbon dioxide under various temperature and pressure conditions. When the mixture was analyzed with a global mole composition higher than 70 mol% CO_2, liquid-liquid immiscibility was observed at temperatures far from the critical temperature of CO_2. The true nature of this phase transition was not fully understood and was attributed to the increased system asymmetry, mainly due to the excess CO_2 and the heavy hydrocarbon fraction. Furthermore, the limited sensitivity of some traditional PVT techniques was highlighted, reinforcing the need for a combination of analytical techniques to study such complex systems.

Since the true nature of the liquid-liquid equilibrium phenomenon observed in Chapter II is not yet fully understood, this chapter aims to study two different oil samples from the Brazilian pre-salt, sourced from two different fields, to determine whether this behavior is specific to a single fluid or caused by a particular component. Both samples present similar compositional analyses but differ in their S.A.R.A. distribution, particularly in the resins/asphaltene ratio. Additionally, this study was conducted at the reservoir temperature for each sample. The goal is to determine whether the appearance of heavier and denser phases, linked to the S.A.R.A. composition of the crude oils, influences the formation and the characteristics of the second liquid phase upon CO_2 addition. To achieve this, the same experimental setup used in Chapter II was

applied, including *pressure-volume* curves, light scattering techniques, direct observation through sapphire windows, and high-pressure microscope inspection. Consequently, a new experimental dataset for two different Brazilian pre-salt crude oils recombined with CO_2 was generated to highlight the experimentally observed multiphase equilibria.

4.2 Materials and Methods

4.2.1 Dead crude oil samples

Petróleo Brasileiro S.A. supplied both PSO-1 and PSO-2 dead crude oil samples. In this chapter, crude oil samples were named PSO-1 and PSO-2. Table 4 gives general information such as API gravity, S.A.R.A analysis, and water content. Moreover, Table 5 depicts the compositional analysis of crude oil samples. In this special case, the crude oil composition analysis is given as a lump because of confidential information regarding the fluid composition.

Table 4. API gravity, S.A.R.A. analysis, water content.

Properties	PSO-1	PSO-2
API gravity / °API	27.0	29.0
saturated content ±1 / wt%	78.3	60.9
aromatic content ±1 / wt%	20.5	21.8
resins content ±0.05 / wt%	0.40	16.9
asphaltene content ± 0.05 / wt%	0.70	0.40
water content ± 0.1 / wt%	0.2	0.6
wax appearance temperature / K	295.65	295.44
reservoir pressure / MPa	61.78	48.23
reservoir temperature / K	367.15	396.15

Table 5. Compositional analysis of crude oil samples.

	PSO-1	PSO-2
component	mol %	
C3	0.50	0.36
i-C4	0.24	0.20
n-C4	0.91	0.82
i-C5	0.70	0.72
n-C5	1.47	1.52

C6-C10	29.87	33.32
C11-C15	22.43	24.43
C16-C19	10.63	11.09
C_{20+}	33.25	27.54
C_{20+} molar weight / g·mol^{-1}	537	513

Density (ρ) and viscosity (η) measurements for API gravity determination were performed by using an Anton Paar SVM 3000 digital oscillation U-tube viscodensimeter, with standard uncertainty for ρ and η equal to ± 0.0005 g·cm^{-3} and ± 0.02 mPa·s, respectively. The temperature inside the U-tube cell was regulated to ± 0.01 K. Furthermore, asphaltene content was determined using the methodology reported by ALBOUDWAREJ et al. (2002), which consists of a single stage contact with n-heptane (analytical grade > 99.8 %). Moreover, the saturated, aromatic, and resin content described in Table 4 was determined using the ASTM D2007M procedure (Kharrat et al., 2007). Furthermore, water content was determined by Karl-Fischer titration (Metrohm, Brazil) in a triplicate procedure to ensure the real amount of water present in both samples. Wax appearance temperature (WAT) was determined by the intersection of two lines in the viscosity logarithm against the inverse of the absolute temperature plot described elsewhere (Paiva et al., 2017; Romero Yanes et al., 2018). Figure 18 presents the viscosity against the temperature of PSO-1 and PSO-2. Asphaltene onset precipitation was determined by asphaltene yield against n-C$_7$ mass fraction curve following the methodology described elsewhere (Agrawal et al., 2012; Alves et al., 2019) as well by determination of asphaltene solubility class index (ASCI) (Passade-Boupat et al., 2018) and the results are given in Table 6. The ASCI test can provide information on asphaltenic phase instability in oil infinity dilution mixtures of toluene and n-heptane (n-C7).
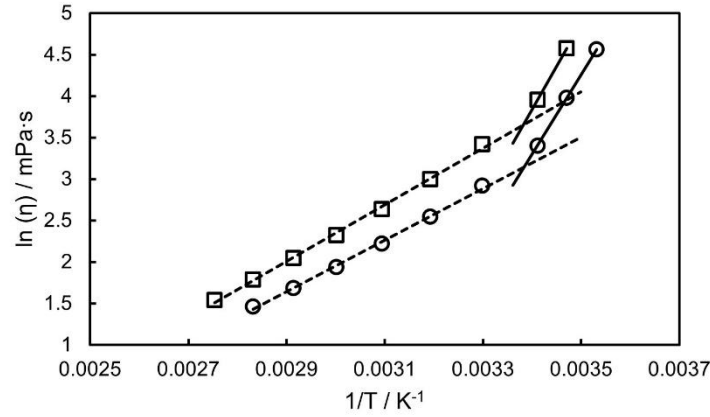
Figure 18. The natural logarithm of viscosity against the inverse of temperature plot. PSO-1 (□, square) and PSO-2 (○, circle).

Table 6. Asphaltene solubility class index (ASCI) and onset precipitation of PSO-1 and PSO-2 samples at p = 0.1 MPa.

	PSO-1	PSO-2
ASCI	16	14
asphaltene onset precipitation, wt% n-C_7	55.28	44.22

This chapter also applied the synthetic method to conduct all fluid phase equilibria investigations (Dohrn et al., 2024). This approach overcomes the challenge of determining phase compositions by allowing the preparation of a mixture with a known global composition. However, this challenge is replaced by the difficulty of precisely achieving the exact global composition required to perform the experiments. Therefore, the phase behavior investigation of both PSO-1 and PSO-2 crude oil samples was conducted at reservoir temperature (Table 4) by adding a known amount of carbon dioxide (CO_2) to dead oil. Six (6) global mole compositions for PSO-1 + CO_2, as follows: z_{CO_2} = (40.8, 60.9, 70.2, 75.1, 78.0, and 80.0) mol%; and for PSO-2 + CO_2, as follow: z_{CO_2} = (35.6, 66.8, 72.8, 75.0, 78.0, and 80.0) mol% were investigated. General information on the gas used in this chapter is given in Table 7.

Table 7. General information on carbon dioxide (CO_2) used in this chapter for fluid phase behavior investigations.

component	CAS Reg. No.	molar weight/ g·mol^{-1}	mole fraction purity[a]	supplier
carbon dioxide	124-38-9	44.0	0.99995	White Martins, Brazil

4.2.2 Experimental setup, mixture preparation and constant mass expansion procedure

The same experimental apparatus used in Chapter II was applied in this chapter, and a representative schematic is shown in Figure 19. First, the PVT measurement cell is vacuumed. Then, a high-pressure transfer cylinder is loaded with crude oil sample (PSO-1 or PSO-2) and injected into the measurement cell using a syringe pump (Teledyne Isco 100DM). The amount of crude oil injected is determined by measuring the mass difference before and after injection using an analytical scale (Sartorius MSU5203P) with an accuracy of ±0.005 g. Next, a given amount of carbon dioxide (CO_2) is injected under pressure into a PVT measuring cell using a second syringe pump with a resolution of 0.1 mL. Pressure and temperature were monitored to guarantee a constant CO_2 density at transfer conditions, enabling the conversion of the recorded volume displacement into injected mass. For this purpose, the density of CO_2 was taken from the *NIST database* (Linstrom; Mallard, 2001). The expanded ($k = 2$) uncertainty to global mole composition $Uc(z_{CO_2})$ was estimated to be lower than 0.25 mol %. More details about global mole composition uncertainty are given in Appendix I.
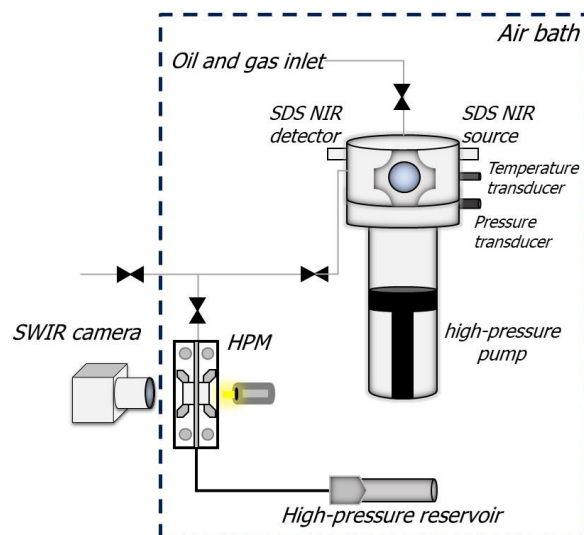
Figure 19. Schematic diagram of pressure-volume-temperature setup, high-pressure microscope, and sample injection ensemble. (Created by the author)

After the preparation of the mixture, the temperature was stabilized, and the system pressure was gradually increased to the maximum pressure condition for each global composition. Similar to Chapter II, depending on the global composition, the system can either remain in a single liquid phase or form two fluid phases in equilibrium at high-pressure conditions. The mixture was kept under pressure before the experiment and constantly stirred for at least 12 hours to achieve thermodynamic equilibrium. Afterwards, a traditional constant mass expansion procedure was performed, comprising two steps: i) successive programed depressurization ramp, named continuous depletion, and ii) mid-ramp programmed stabilization, referred to as the equilibrium step. Continuous depletion is performed at a constant rate of 0.4 MPa·min^{-1} under stirring to maintain the system in equilibrium while the stirring system is turned off during the equilibrium step of 5 minutes. During the equilibrium step, pressure, temperature, volume, and light transmittance power (NIR-SDS signal) values are recorded using Applilab ® software. From all these measurements, phase transition pressures are indirectly determined.

The plot of the *pressure-volume* (*p,V*) curve is initially applied to identify the transition between the low-compressible (liquid) and highly-compressible (vapor) phases. Nevertheless, as pointed out in Chapter II, the difference between the volumetric properties of liquid and vapor is reduced for mixtures with high gas content. In this

condition, plotting the volume change concerning pressure is preferable instead of the volume itself. To do so, we utilize the *Y*-factor parameter given by the following equation:

$$Y_{factor} = -\frac{V_{initial}}{P_{initial}}\left(\frac{P-P_{initial}}{V-V_{initial}}\right) \tag{3.1}$$

where $V_{initial}$ and $P_{initial}$ denote the volume and pressure of the PVT cell measurements at the CME test's initial conditions, respectively. The *Y*-factor is a dimensionless property related to the secant bulk modulus of the fluid (Daridon; Orlandi; Carrier, 2016) and has been proven to detect the vapor phase in mixtures with a high gas content (Daridon et al., 2020; Romero Yanes et al., 2021b).

4.2.3 *High-pressure microscope inspection*

Similarly to Chapter II, all mixtures were investigated using the high-pressure microscope (HPM-SWIR). The previous chapter demonstrated that SWIR inspection allows for precise observation of the fluids inside the microscope, enabling the detection of fluid-fluid transitions that are nearly undetectable by conventional PVT techniques. Therefore, this approach was applied again to better understand and characterize the fluid-fluid transitions observed in this chapter, particularly the transition from a single liquid phase to a liquid-liquid transition.

Once the HPM-SWIR is loaded with the mixture, an isothermal depletion is performed under the same conditions as the CME test. Additionally, during the system depletion in the HPM-SWIR tests, the fluid flows from the PVT measuring cell to the high-pressure reservoir simultaneously at a flow rate of 0.3 cm³·min⁻¹ using an external syringe pump. This methodology ensures that the sample observed inside the HPM-SWIR cell remains representative of the fluid inside the PVT cell throughout the test.

4.3 Results and discussion

4.3.1 Oil PSO-1 + CO₂

Table 8 lists all experimental data measured for PSO-1 + CO_2, and Figure 20 presents the p,V curves at $T = 367.15$ K for different PSO-1 + CO_2 mixtures with CO_2 content ranging from 40 to 80 mol%. For global composition up to 75.1 mol% CO_2, a vapor phase formation was detected by observing discontinuities in the derivative of p,V curves in Figure 20. The NIR-SDS signal confirmed this finding. As depicted in Figure 21a, where the NIR-SDS light transmittance recorded during the CME performed in a mixture with 40.8 mol% of CO_2 was plotted as a function of pressure along with the Y-factor (eq. 3.1), the sharp change in NIR-SDS signal intensity perfectly coincides with the shift in fluid compressibility highlighted by a break in Y-factor slope. Such a sharp drop in light transmittance results in small bulk bubbles, leading to light scattering at the bubble point pressure. Similar behavior was observed until 78.0% of carbon dioxide was injected into the oil. For this specific CO_2 composition and beyond, as shown in Figure 20, the measured p-V curve displays a smooth shape with no discernible slope breakpoints. This characteristic p,V curve shape is typical of medium crude oil (25.1<API°<30.8), with a high gas content ($z_{gas} > 70.0$ mol%) (Johnston et al., 2017; Romero Yanes et al., 2020b). However, a change regime in the derivative of the volumetric behavior is observed in the Y-factor, as depicted in Figure 21b for a mixture with 80% CO_2, which would indicate the appearance of a vapor phase in a liquid system. The bubble formation is also highlighted by a drastic variation in the signal measured by the SDS probe, as shown in Figure 21b. The bubble point occurs at pressure conditions near $p = 35$ MPa for this composition. The same trend for Y-factor and NIR-SDS signal against pressure was observed for the system with 75.1 and 78.0 mol% gas, indicating the presence of a bubble point as fluid depletion occurs in all these mixtures.

A comparison of Figures 21a and 21b reveals different phenomena above the bubble point. In Figure 21a, corresponding to a mixture with low CO_2 content, the signal appears continuous throughout the experiment. It suggests that no phase transition occurs until the bubble point is reached. On the contrary, in Figure 21b, the SDS signal between 45 and 35 MPa fluctuates between the expansion and stabilization of the system. This type of observation is characteristic of a heterogeneous system that settles when system stirring is stopped, indicating that another transition occurred above the bubble point

pressure. This suggests that a phase split takes place during the depletion of this mixture. Still, it was impossible to detect them indirectly by the *Y*-factor curve due to the low compressibility contrast between the fluid phases at the phase separation point. To confirm this finding, constant mass expansion experiments were repeated for these mixtures, but this time using the HPM device.

Table 8. Experimental phase transition data was measured for PSO-1 + CO_2 at the corresponding reservoir temperature ($T = 367.15$ K).

z_{CO_2} / mol%	p / MPa	transition
40.8	7.05	L → LV
60.9	13.24	L → LV
70.2	20.11	L → LV
75.1	28.70	L → LL[a]
78.0	42.16	L → LL[a]
80.0	48.95	L → LL[a]
75.1	27.10	LL→LLV
78.0	32.92	LL→LLV
80.0	35.56	LL→LLV

[a]Phase transition observed during fluid inspection inside HPM-SWIR. Standard uncertainties $u(T) = 0.1$ K, and the expanded uncertainties Uc (k=2) are $Uc(z_{CO_2}) = 0.25$ mol%, $Uc(L \rightarrow LV) = 0.25$ MPa, $Uc(L \rightarrow LL) = 0.31$ MPa, and $Uc(LL \rightarrow LLV) = 0.25$ MPa.
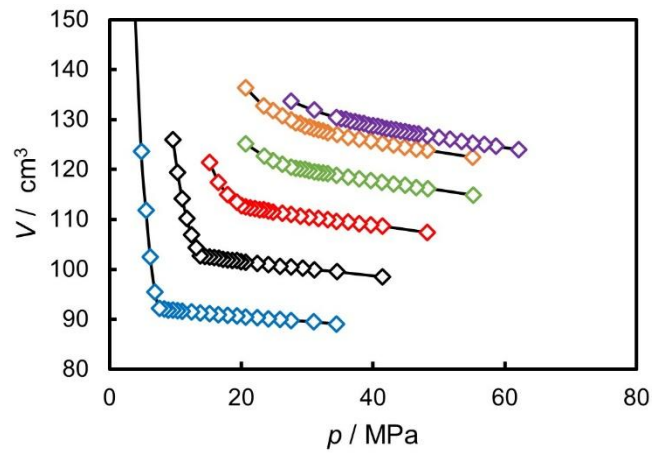
Figure 20. Pressure-volume plot for PSO-1 + CO_2 systems at $T = 367.15$ K and different global mole compositions, such as $z_{CO_2} = 40.8$ mol% (blue diamond, ◊), $z_{CO_2} = 60.9$ mol% (black diamond, ◊), $z_{CO_2} = 70.2$ mol% (red diamond, ◊), $z_{CO_2} = 75.1$ mol% (green

diamond, ◊), z_{CO_2} = 78.0 mol% (orange diamond, ◊), and z_{CO_2} = 80.0 mol% (purple diamond, ◊).
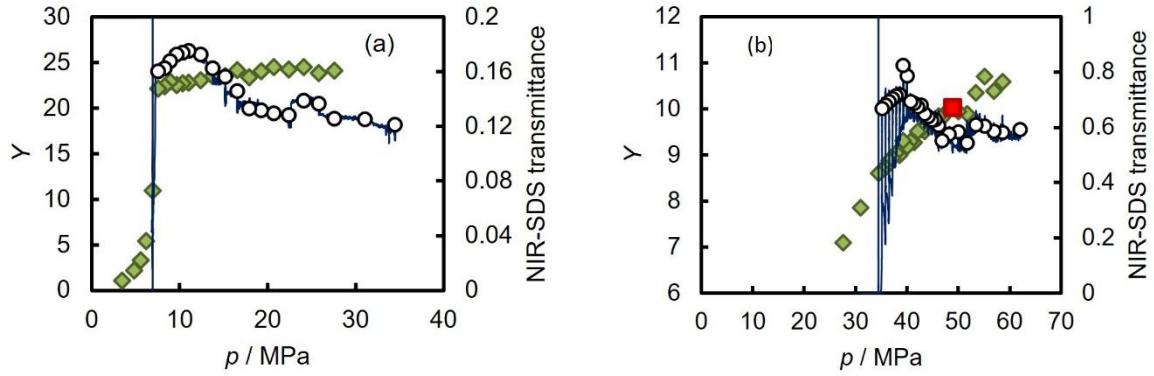
Figure 21. CME tests result for PSO-1 + CO$_2$ [z_{CO_2} = (40.8 and 80.0) mol%] at T = 367.15 K; Y-factor (green diamond, ♦) against pressure and NIR-SDS transmittance (circle, ○); (a) z_{CO_2} = 40.8 mol% and (b) z_{CO_2} = 80.0 mol%.

Figure 22 shows snapshots of the fluid inside the HPM cell taken with the SWIR camera during a CME experiment for a mixture with 75 and 80 mol% CO$_2$. A monophasic liquid state was observed in the first snapshots (3.5a and 3.5d) corresponding to the higher pressure of each experiment, demonstrating that all CO$_2$ was recombined in the PSO-1 sample at higher pressure, even in such high gas content conditions. It is worth noting that the black dots in this figure are only adhered dirt on the inner surfaces of the sapphire windows or on the SWIR camera lens, which cannot be removed without completely dismantling the apparatus (camera + cell). However, this inconvenience does not compromise all the experimental results regarding inspecting the fluid inside the HPM-SWIR. Figures 22b and 22e illustrate the formation of a dispersed liquid phase as the pressure drops during fluid expansion.

This transition from a single liquid phase to a liquid-liquid (LL) equilibrium is more evident for a system with 80 mol% CO$_2$. It can be seen in Figure 21b, where the pressure at which this second liquid phase appears is marked as a red square (■), that the formation of this second phase did not lead to a significant variation in the mixture compressibility or NIR-SDS signal. Similar to the second liquid phase identified and discussed in Chapter II, the dispersed liquid phase observed for PSO-1 + CO$_2$ remains

stable when the pressure is maintained constant, showing similar characteristics, with no phase segregation due to gravity in the PVT cell head.

Additionally, rapid redissolution is observed when the pressure inside the HPM-SWIR increases, indicating a reversible transition. This behavior supports the hypothesis that both fluid phases formed have a low-density contrast, leading to poor phase segregation. Based on this first result, it is possible to suggest that this fluid-fluid transition is not exclusive to a specific Brazilian pre-salt sample. Furthermore, this phase transition was again observed only in mixtures with a CO_2 mole composition higher than 70 mol%.
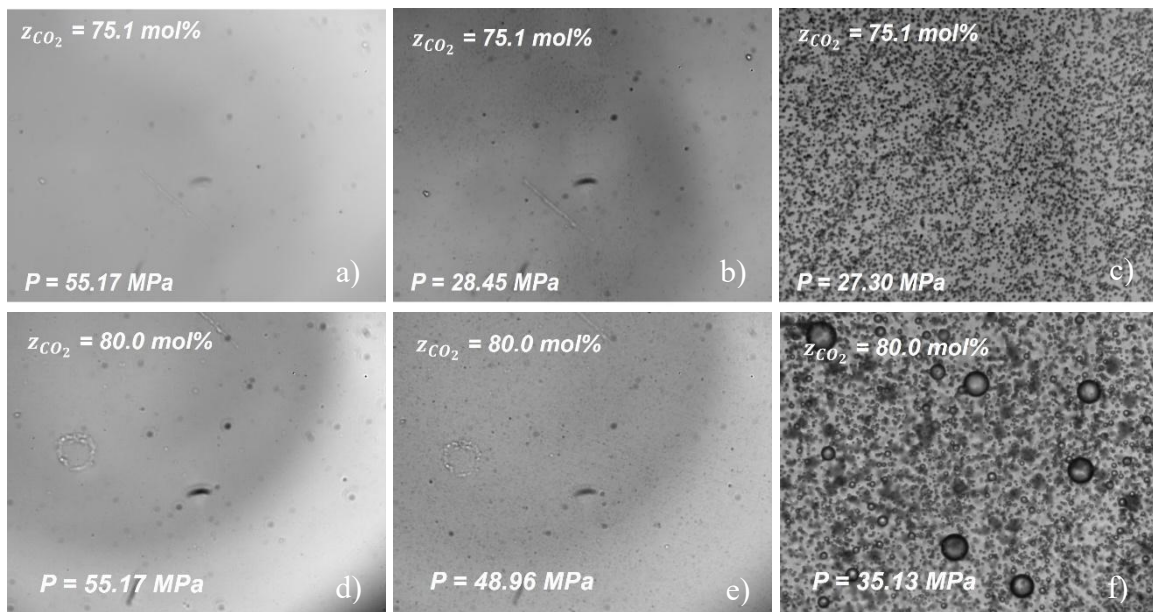
Figure 22. Fluid inspection using the HPM-SWIR for PSO-1 + CO_2 z_{CO_2} = (75.1 and 80.0) mol% system at T = 367.15 K. Snapshots using a magnification of 5x.

Considering the PSO-1 + CO_2 mixture with a global composition of 80 mol% CO_2, observations made while the mixture flows through HPM-SWIR revealed that the second liquid phase formed reflects a preference to adhere to the sapphire windows of the microscope. This behavior may indicate some phase polarity and their affinity to the polar surface of the microscope cell, as suggested by previous studies (Cardoso et al., 2015). During constant mass expansion experiment, the volume of the dispersed phase increases up to a saturation pressure near p = 35.0 MPa, where vapor bubbles are released from the liquid droplets. At this point, called the bubble point, the system becomes in a three-phase liquid-liquid-vapor equilibrium. This point coincides with the pressure condition where

the *Y*-factor shows a regime change in Figure 21b. These HPM observations reveal that the fluid passes from a monophasic liquid state, forming a liquid-liquid (LL) equilibrium by depressurization, and then undergoes a three-phasic liquid-liquid-vapor (LLV) equilibrium at low pressure. The same behavior was observed for systems with 75.1 and 78.0 mol% CO_2. All the measured transition pressures, L→LL and LL→LLV, are listed in Table 8. This type of phase transition mapping was made possible by combining SWIR-microscopy fluid inspection with the *Y*-factor plot. Although the NIR-SDS indicates a phase transition at the same pressure condition as the *Y*-factor curve (around 35 MPa), without the SWIR inspection, both the liquid-liquid and the liquid-liquid-vapor transitions could be overlooked, and the system might be mistakenly considered as a simple liquid to liquid-vapor transition.

The phase behavior observed here for high CO_2 content is very similar to those observed in Chapter II and other investigations of pre-salt crude oil fluid phase behavior (Cardoso et al., 2015; Romero Yanes et al., 2020a). Typically, in simple binary or synthetic CO_2 systems, the liquid-liquid equilibrium (LLE) occurs at temperatures near the CO_2 critical temperature (Al Ghafri; Maitland; Trusler, 2014; Braga; Tavares; Ndiaye, 2022; Daridon et al., 2021; Enick; Holder; Morsi, 1985; Fall; Luks, 1985; Hottovy; Luks; Kohn, 1981; Kukarni et al., 1974; Simoncelli et al., 2020; Yanes; Montel; Daridon, 2022a). This behavior is also observed in more complex systems, such as crude oil + carbon dioxide (Bryant; Monger, 1988; Eghbali; Dehghanpour, 2017; Lindeloff et al., 2013; Orr; Jensen, 1984; Orr; Yu; Lien, 1981; Turek; Metcalfe; Fishback, 1988b). In both cases, the liquid-liquid phase is characterized by oil-rich and CO_2-rich phases. Despite the ability of CO_2 to extract some heavy hydrocarbons (Larson et al., 1989; Turek; Metcalfe; Fishback, 1988b), the liquid-liquid equilibrium in these systems exhibits two well-defined fluid phases with distinct densities and is limited at temperature conditions near to CO_2 critical temperature. However, in this study, the investigation was conducted at $T = 367$ K, well above the CO_2 critical temperature. Under these pressure and temperature conditions, Yanes et al. (2020) showed that the second liquid phase formed from a pre-salt oil concentrates more high molecular weight hydrocarbon through a combination of experimental measurements and equation-of-state modeling. Qualitatively, it can infer a similar conclusion on the LL observed in this chapter, with the formation of a dispersed phase that seems denser and more viscous than the initial oil, allied to the fact that it has a similar interaction with the sapphire window, indicating the

polar nature of the formed liquid phase and their asphaltene-like interactions, resembling more of a bituminous phase than a low-viscosity, mobile CO_2-rich phase.

Throughout the CME experiment, no observations indicated the destabilization of asphaltenes through the appearance of unstable asphaltene flocs. Consequently, the asphaltenes remain concentrated within this dispersed liquid phase rather than self-aggregating into solid flocs. These findings suggest that the asphaltenes maintain their solubility within the dispersed liquid phase, contributing to their dark, heavy, and viscous behavior.

4.3.2   Oil PSO-2 + CO_2

The second pre-salt oil (PSO-2) sample was investigated by adding up to 80 mol% of carbon dioxide. Table 9 gives all experimental phase transition points measured in this pseudo-binary system. For this system, the occurrence of a vapor phase was indirectly detected from the slope change in p,V diagram for mixture with a global mole percentage until $z_{CO_2} = 75.0$ mol%, as shown in Figure 23. Above this gas content, the volumetric method failed to detect any transition. However, the NIR-SDS and HPM-SWIR techniques effectively identified phase transitions in these conditions.

Table 9. Experimental phase transition data was measured for PSO-2 + CO_2 at the corresponding reservoir temperature ($T = 396.15$ K).

z_{CO_2} / mol%	p / Mpa	transition
35.6	9.17	L + A → LVA
66.8	20.53	L + A → LVA
72.8	25.79	L + A → LVA
75.0	29.33	L + A → LVA
78.0	41.37	L + A → LLA[a]
80.0	46.19	L + A → LLA[a]
78.0	31.89	LLA → LLVA
80.0	34.23	LLA → LLVA

[a]Phase transition observed during fluid inspection inside HPM-SWIR. Standard uncertainties $u(T) = 0.1$ K, and the expanded Uc (k=2) are $Uc(z_{CO_2}) = 0.3$ mol%, $Uc(L \rightarrow LV) = 0.25$ MPa, $Uc(L \rightarrow LL) = 0.31$ MPa, and $Uc(LL \rightarrow LLV) = 0.25$ MPa.
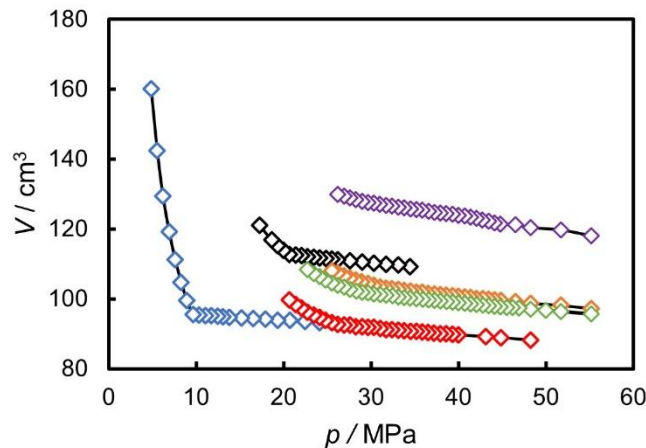
Figure 23. Pressure-volume plot for PSO-2 + CO_2 systems at T = 396.15 K and different global mole compositions. z_{CO_2}= 35.6 mol% (blue diamond, ◊); z_{CO_2}= 66.8 mol% (black diamond, ◊); z_{CO_2}= 72.8 mol% (red diamond, ◊); z_{CO_2}= 75.0 mol% (green diamond, ◊); z_{CO_2}= 78.0 mol% (orange diamond, ◊); and z_{CO_2}= 80.0 mol% (purple diamond, ◊).

In this second system, the recorded NIR-SDS light transmittance signal exhibited a significant difference between depletion and equilibrium steps. Figures 24a and 24b show the difference in NIR-SDS signals between equilibrium steps and continuous depletion, even in the mixture with only 35% CO_2. This type of SDS response is usually associated with a heterogeneous system that can be either a liquid-liquid or liquid-solid phase equilibrium. Typically, this behavior can be assigned to an asphaltene precipitation (Lei et al., 2015; Romero Yanes et al., 2019a) once carbon dioxide could act as an asphaltene destabilizer (Cruz et al., 2019; Gonzalez et al., 2008). However, as the light scattering technique is an indirect measurement technique for phase transition detection, more is needed to know about the nature of the phases in equilibrium. Therefore, to identify the nature of the phases in equilibrium responsible for the anomalies detected by the NIR-SDS signal, all the mixtures studied for PSO-2 + CO_2 were investigated using the HPM-SWIR device.
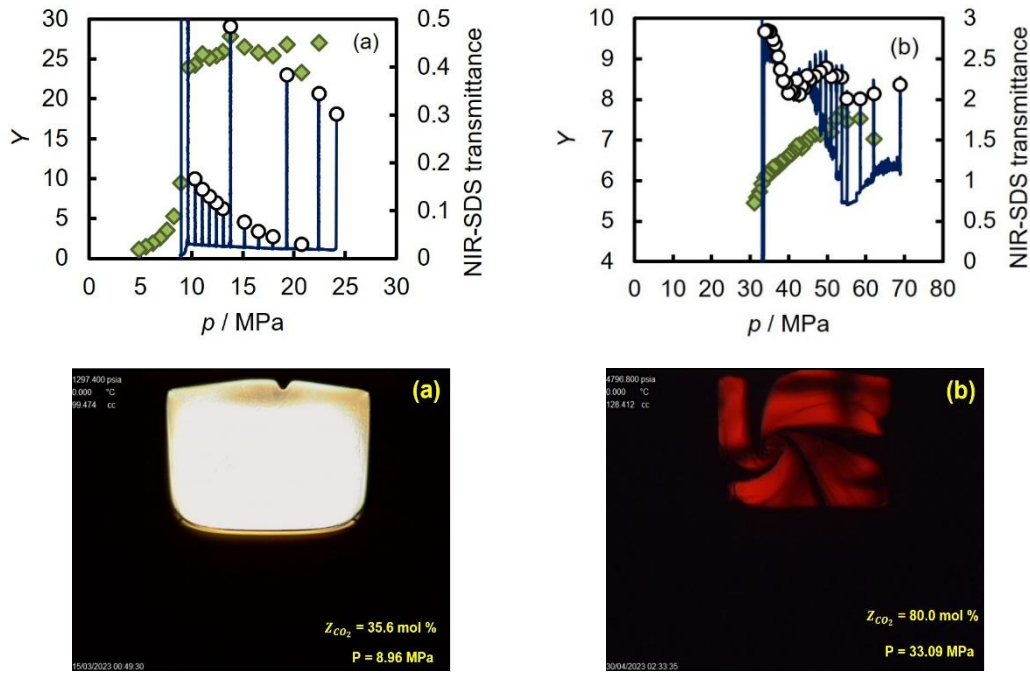
Figure 24. CME tests results for PSO-2 + CO_2 [z_{CO_2} = (35.6 and 80.0) mol%] at 396.15 K; Y-factor (green diamond, ♦), NIR-SDS transmittance (circle, ○) against pressure, and direct observation through sapphire windows at PVT cell head. 6.a, z_{CO_2}= 35.6 mol%; 6.b, z_{CO_2}= 80.0 mol%.

Figure 25 depicts snapshots obtained during a fluid inspection in HPM-SWIR for a system with 72.8 mol% CO_2 system at T = 396.15 K. For this composition, it can be observed asphaltenic flocs stuck onto the sapphire window of the microscope cell, demonstrating a preference for the polar surface of HPM-SWIR sapphire window (Cardoso et al., 2015; Romero Yanes et al., 2020b). The amount of these unstable asphaltenes qualitatively increases with fluid depletion. This behavior was also experimentally observed for the system with 75.0 mol% CO_2. The same destabilized asphaltenes were observed in the previous compositions, even in the mixture with 35.6 mol% CO_2. The asphaltenes adhere at the sapphire window in the HPM-SWIR cell, preventing an accurate observation of vapor phase formation inside the HPM cell. However, as previously pointed out, LV transitions were easily detected from the classical *p-V* method (up to 72.8 mol% CO_2) in this composition range. Surprisingly, asphaltenes of oil PSO-2 destabilize in a mixture containing 35 mol% CO_2, equivalent to 9% by mass, whereas 44 wt% heptane is needed to destabilize the dead oil, which is almost five times more. These findings reveal that the discontinuity in the NIR-SDS signal was caused by

the presence of asphaltene flocs in the bulk fluid, showing that, even under high-pressure conditions, the mixture is not in a single-phase liquid state.

Nevertheless, Sepúlveda's criteria (Guzmán et al., 2017; Kumar; Voolapalli; Upadhyayula, 2018), based on S.A.R.A. analysis presented in Table 4, predict a stabilization of asphaltenes in this system. Nevertheless, this result is contradictory to observations within the HPM-SWIR. Despite having similar asphaltene contents and ASCI values, the two oils differ drastically regarding asphaltene destabilization caused by CO_2 injection and their resin content, which is significant in dead oil PSO-2. Therefore, the interaction between CO_2 and resins is likely the primary factor contributing to the substantial difference in the quantity required for asphaltene destabilization in the oil, either by C_7 or CO_2. However, because of the large resins in the PSO-2 sample, it is prudent to state that this heavy solid phase results from the co-precipitation of resins and asphaltene. Furthermore, compared to sample PSO-1, the resin/asphaltene ratio plays an important role in the occurrence of this solid phase once no significative compositional difference can be observed between both crude oil samples.
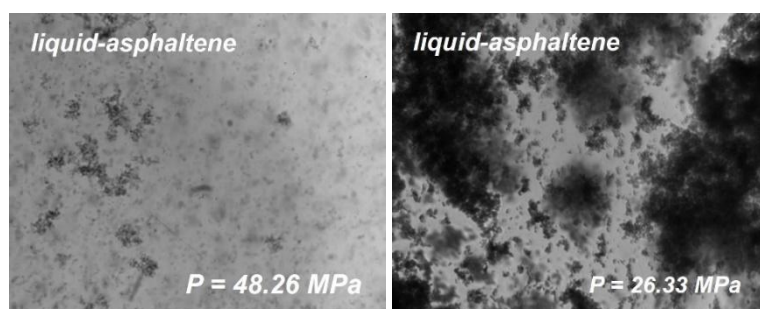
Figure 25. Fluid inspection using the HPM-SWIR for PSO-2 + CO_2 (z_{CO_2} = 72.8 mol%) at T = 396.15 K. Snapshots using a magnification of 5x.

To complete the fluid phase behavior of the PSO-2 + CO_2 system, two additional global compositions corresponding to 78.0 and 80.0 mol% CO_2 were evaluated. Figure 26 shows some snapshots obtained during fluid inspection inside the HPM-SWIR cell. The behavior of the fluid phase observed differs significantly from the compositions studied previously, as the asphaltenes observed within the HPM-SWIR decreased in a composition with a high gas content compared to the mixture with 72% and 75% carbon dioxide. With this high CO_2 content, the system tends to demix as pressure decreases during the CME experiment and forms a liquid-liquid equilibrium. At

these compositions, the phase behavior becomes similar to that found in PSO-1 + CO_2 systems with 78.0 and 80.0 mol% CO_2. The transition from liquid to liquid-liquid was particularly tricky to detect with this second system due to the presence of unstable asphaltenes stuck on sapphire windows above the L to LL transition pressure, and that masked the appearance of scattered droplets during fluid depletion in the HPM cell.

Moreover, this fluid-fluid transition does not affect the *Y*-factor curve, as shown in Figure 21, and SDS is perturbed by the flocs of asphaltenes still present in the system. Therefore, the formation of this high-pressure fluid-fluid phase equilibrium was detected by the appearance of turbidity inside HPM-SWIR caused by the scattering of SWIR light. As depletion evolves, the second liquid phase interacts with the unstable asphaltene present in HPM-SWIR to form an apparent macroscopic fluid phase adhering to the surface of the microscope. This phase resembles a heavy hydrocarbon phase and exhibits viscosity akin to a bituminous phase. Microscopic observations do not conclusively distinguish whether this is a homogeneous phase formed by the redissolution of asphaltenes within the second liquid phase or a heterogeneous medium comprising unstable asphaltenes and the second liquid phase. In these conditions, the observation of the second system closely resembles that observed for the PSO-1 sample, reinforcing that the second liquid phase formed has heavy polar petroleum components dissolved. For this complex experimental observation, the static nature and the fact that a small portion of the entire fluid is observed means that it is impossible to distinguish whether another transition has occurred, which requires a visual technique in which the whole fluid is followed under this condition. Finally, as present in Figure 27, the *Y*-factor against pressure demonstrates an occurrence of a vapor phase at pressure conditions near $p = 31.00$ and 34.00 MPa for systems with 78.0 and 80.0 mol% CO_2, respectively. These bubble point pressures were determined by the intersection between the linear trend in the liquid-liquid (LL) and liquid-liquid-vapor (LLV) regions. Therefore, for these two last compositions studied, it can be observed that during a CME experiment, the system initially consists of a single liquid phase with a few unstable asphaltenes. Subsequently, it goes into a liquid-liquid (bitumen) phase and finally reaches a three-phase liquid-liquid-vapor equilibrium (LLV) below the bubble point when the experiment concludes.
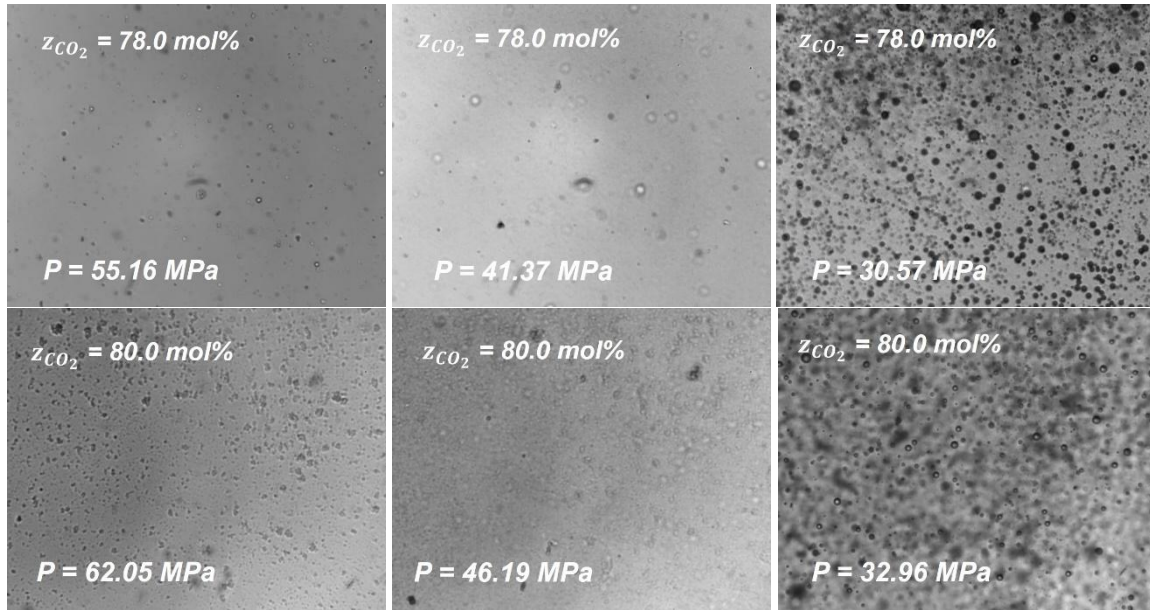
Figure 26. Fluid inspection using the HPM-SWIR for PSO-2 + CO_2 [z_{CO_2}= (78.0 and 80.0) mol%] system at T = 396.15 K. Snapshots using a magnification of 5x.
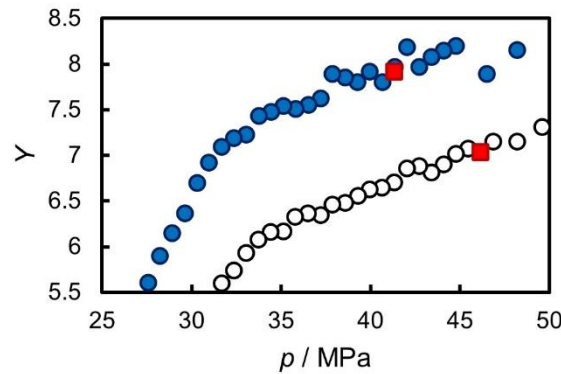
Figure 27. *Y-factor* against pressure for PSO-2 + CO_2 [z_{CO_2} = (78.0 and 80.0) mol%] at T = 396.15 K; z_{CO_2}= 78.0 mol% (blue circle, ●); z_{CO_2}= 80.0 mol% (empty circle, ○); LL equilibrium observed in HPM-SWIR (red square, ■).

4.3.3 Comparison between phase behavior of PSO-1+ CO_2 and PSO-2 + CO_2

Figure 28 shows the pressure-composition (*p,z*) fluid phase equilibrium diagrams constructed from all the phase transition measurements obtained for PSO-1 + CO_2 and PSO-2 + CO_2 at the respective reservoir temperatures. These phase diagrams show a similarity in the fluid phase behavior of both crude oil samples investigated

concerning the transition pressure experimentally measured, despite their differing responses to asphaltene destabilization.

The onset of asphaltene destabilization was not added in either of these diagrams as it was not detectable. No unstable asphaltene was observed in the first system, regardless of the amount of carbon dioxide added to the system or the pressure investigated. Conversely, asphaltene destabilization was observed above the bubble point in all the mixtures investigated for the second system. However, the resin/asphaltene ratio is essential in the liquid-liquid and liquid-liquid-vapor transitions when no significant compositional difference can be observed in different crude oil samples.
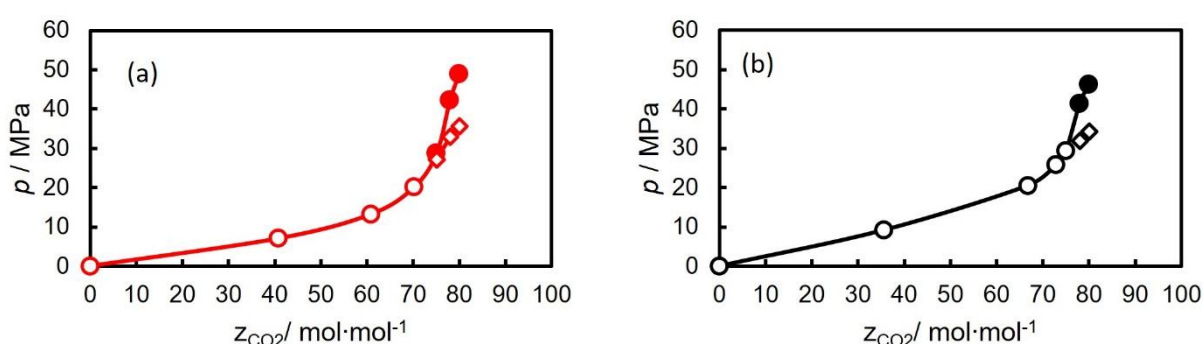
Figure 28. Isothermal pressure-composition diagram for PSO-1 + CO_2 mixture (a) at $T = 367.15$ K and PSO-2 + CO_2 mixture (b) at $T = 396.15$ K. L→LV transition (empty circle, ○), L → LL transition (full circle, ●), and LL → LLV transition (diamond, ◊).

Among all the systems studied in this chapter, the intrinsic phase behavior of crude oil mixtures with high CO_2 content reveals several noteworthy points: Firstly, the transition from liquid-liquid (LL) to liquid-liquid-vapor (LLV) with CO_2, for which there are not many studies available in the literature that report this type of phase transition for similar or comparable systems, especially under temperature conditions significantly higher than the critical temperature of CO_2; and secondly, the redissolution of the asphaltene phase above the bubble point pressure, probably due to the molar excess of supercritical CO_2 when a liquid-liquid phase split occurs.

The difference in the minimum global composition required to observe the transition from L to LL in the two systems studied in this chapter can be attributed to the difference in reservoir temperatures investigated. While it has not yet been possible to confirm whether the dispersed LLE effectively concentrates the heavy polar fraction of

the oil, this hypothesis is supported by the experimental observations from HPM-SWIR. This aspect will be examined in greater detail in the next chapter of this Thesis.

4.4   Conclusion

A new set of data for two different samples of Brazilian crude oil recombined with carbon dioxide is presented in this chapter, showing not only liquid to liquid vapor, but also the occurrence of liquid-liquid and liquid-liquid-vapor transitions. For both crude oil samples studied, a liquid-liquid equilibrium characterized by a second heavy liquid phase similar to bitumen showed a similar behavior on adhesion in the sapphire window of the HPM cell, which was very similar to the LL equilibrium observed in Chapter II. Indicating that this is not a fluid-fluid transition unique to a Brazilian pre-salt sample. In addition, an unstable phase was observed in the PSO-2 + CO_2 systems investigated, and its precipitation was related to the CO_2-resin interaction. Furthermore, due to the high complexity of the fluid-fluid transition observed in this chapter and the limitation of the experimental observations in the HPM-SWIR, a new visual approach will be used in the next chapter to study the phase behavior of the oil + gas systems.

5 CHAPTER IV: A COMPREHENSIVE STUDY OF DIFFERENT CRUDE OIL SAMPLES BY ADDING CARBON DIOXIDE AND/OR METHANE: EXPERIMENTAL AND MODELING STUDY

5.1 Introduction

In the last two chapters (II and III), the occurrence of a fluid-fluid transition with specific characteristics has been shown, including: i) low-density contrast, ii) high dispersity, and iii) rapid redissolution with pressure increase. This liquid-liquid equilibrium has been linked to the heavy fraction of crude oil samples, particularly asphaltenes. Furthermore, the observed phase equilibrium was attributed to the system's high asymmetry, which, under high carbon dioxide content conditions, may lead to liquid-liquid immiscibility under high-pressure and high-temperature conditions. This phenomenon underscores the complex interactions within these asymmetric mixtures and their implications for understanding phase behavior in crude oil systems.

So far, the observation of the phase behavior of the samples studied has been achieved through a combination of experimental techniques, primarily two volumetric methods (p-V and Y-Factor) and a light scattering technique (NIR-SDS), along with high-pressure microscopic inspection in the shortwave infrared (SWIR) wavelength range. This combination of techniques enables the observation of various fluid phase transitions and even fluid-solid phase equilibria, facilitating the mapping of the complete phase diagram. However, some uncertainties remain, as only a limited portion of the fluid is visible in the high-pressure microscope. This limitation can hinder the capture of detailed visual information about phase transitions, particularly in scenarios where three phases may be present. In such cases, one phase may exhibit a strong affinity for the surface, causing it to adhere and remain in the PVT cell, thereby rendering it unobservable in the microscopic cell. To address this limitation, using a high-pressure equilibrium cell with full visibility is a suitable approach. In this context, Daridon *et al*. (2020) developed an experimental setup designed for investigating dark fluids by coupling a shortwave infrared camera to a horizontal full-view high-pressure equilibrium cell featuring a large-diameter sapphire window. This innovative method allows for the inspection of the entire fluid sample inside the measurement cell at a wavelength in which heavy hydrocarbons exhibit minimal light absorption, enabling the detection of any phase transitions that

cause SWIR light scattering, particularly for liquid to liquid-liquid transitions. Moreover, this observation can be combined with the volumetric behavior recorded during the experiments. For instance, Yanes *et al.* (2020) employed this setup to investigate samples from the Brazilian pre-salt, demonstrating an accurate method for detecting dispersed fluid-fluid transitions under high-pressure and high-temperature conditions.

Therefore, in this chapter, the method reported by Daridon *et al.* (2020) and Yanes *et al.* (2020) was applied to investigate the fluid phase behavior of three crude oil samples from the Brazilian pre-salt. The main objective is to study the phase behavior and observe the influence of different gases, such as carbon dioxide and methane, on complex phase transitions, especially the liquid to liquid-liquid transition of high-pressure and high-temperature. Additionally, two carbon dioxide + methane mixtures, which represent the gas compositions typically found in Brazilian pre-salt reservoir fluids, were considered for recombination with the three dead oils. The phase behavior study was conducted by varying the global mole composition of the mixture from 13 to 85 mol% gas at temperatures ranging from 308.15 to 373.15 K and pressures up to 90 MPa. This comprehensive approach aimed to provide a complete characterization of the phase behavior of these fluids, represented in both the pressure-temperature (*p-T*) and pressure-composition (*p-z*) diagrams. Finally, the Peng-Robinson equation of state was applied to model all experimental fluid-fluid phase transitions measured in this chapter.

5.2 Materials and methods

5.2.1 *Crude oil samples and gases*

PETROBRAS S.A. provided three different dead crude oil samples, referred to as BPs-1, BPs-2, and BPs-3, to conduct fluid phase behavior studies through gas addition. The characteristics of these samples are shown in Table 10. Additionally, the compositional analysis of the dead crude oil is presented in Table 11. The three crude oil samples come from the same field. PETROBRAS S.A. provided the oil profile, and the standard analysis includes information up to C_{20+} and its molecular weight.

Table 10. General information on the dead crude oil samples used in this chapter.

property	BPs-1	BPs-2	BPs-3
average molecular weight / g·mol^{-1}	287.2	295.2	295.8
Saturates / wt%	59.6	56.8	62.9
Aromatics / wt%	21.6	24.3	18.4
Resins / wt%	17.8	18.0	17.9
Asphaltenes / wt%	1.0	0.9	0.7

Table 11. Profile composition of the dead crude oil samples studied in this chapter.

compound	crude oil sample / mol·mol^{-1}		
	BPs-1	BPs-2	BPs-3
C_3	0.41	0.46	0.30
i-C_4	0.20	0.19	0.13
n-C_4	0.75	0.68	0.53
i-C_5	0.56	0.48	0.39
n-C_5	1.15	0.97	0.83
C_6	2.77	2.22	2.02
C_7	7.60	4.63	4.35
C_8	6.12	6.58	6.42
C_9	6.76	5.91	5.66
C_{10}	5.89	5.00	4.80
C_{11}	4.92	4.34	4.20
C_{12}	4.47	3.94	3.84
C_{13}	4.59	4.13	3.97
C_{14}	4.32	3.40	3.29
C_{15}	3.67	3.22	3.12
C_{16}	3.83	2.54	2.46
C_{17}	2.75	2.09	2.07
C_{18}	3.05	2.25	2.23
C_{19}	2.45	2.15	2.04
C_{20+}	33.40	44.48	47.08
HCF	0.34	0.34	0.27
	molecular weight / g·mol^{-1}		
C_{20+}	550.16	470.28	453.25
HCF	550.80	550.80	550. 80
	BPs-1	BPs-2	BPs-3
γ_{C20+}	0.9516	0.9404	0.9398

*HCF : heavy condensed fraction

Four different gases were used: carbon dioxide (CO_2), methane (CH_4), and two CO_2 + CH_4 mixtures in various molar ratios, as shown in Table 12. Phase behavior

analyses were performed by adding a known mass of the crude oil sample to the PVT cell and gas to achieve the target compositions. The global compositions evaluated ranged from 13.0 to 85.0 mol% gas. All mixtures were prepared by adding gas to the dead crude oil.

Table 12. Gas and their mixture used in this chapter to prepare the system investigated.

compound	mole fraction / mol·mol^{-1}			
	gas-1	gas-2	gas-3	gas-4
CO_2	100.0	0.0	24.7	50.0
CH_4	0.0	100.0	75.3	50.0

5.2.2   High-pressure setup and mixture preparation

The high-pressure PVT apparatus used to determine phase transition in all mixtures evaluated in this chapter is presented in Figure 29. The core of this device features a horizontal high-pressure cell with a variable volume piston that allows a pressure variation from 0.1 to 100 MPa. In addition, the cell is equipped with a full-view sapphire window on the front of the cell. A pressure gauge measures the system pressure in direct contact with the fluid inside the cell. The pressure gauge was calibrated by comparison with a primary standard pressure sensor, providing an accuracy of 0.02% in the operational range of the PVT cell, providing a pressure uncertainty $u(p^{gauge}) = 0.02$ MPa. To homogenize the mixture, the inner face of the piston is equipped with a magnetic stirrer. In addition, temperature cell measurements are carried out using a Pt-100 thermocouple connected to the body of the measuring cell with an uncertainty of $u(T^{gauge}) = 0.1$ K. The fluid temperature is controlled by circulating a heat-carrying fluid through the cell's thermal jacket using a thermostatic bath. A shortwave infrared (SWIR) camera was attached to the front of the sapphire windows. The camera was equipped with three different lenses: a wide-angle lens for capturing an overall view of the fluid within the cell, as well as 4x and 8x lenses for focusing on dispersed liquid droplets and solid objects, such as crystals and asphaltene flocs. The wide-angle lens allows for observation of the fluid along its entire length, from the inside of the sapphire window to the piston-mounted agitator, even in the presence of an opaque fluid up to 10 cm thick. In contrast, the 4x and 8x lenses are designed to focus on specific areas;

therefore, the observed object is typically positioned on the fluid just behind the sapphire window. It is important to note that agitation must be halted to effectively focus on a particular object under these conditions. This visual configuration allows the fluid to be inspected in a spectral range of 900 to 1,700 nm. In this condition, the crude oil samples have minimal light absorption and are therefore visualized as almost transparent fluids.
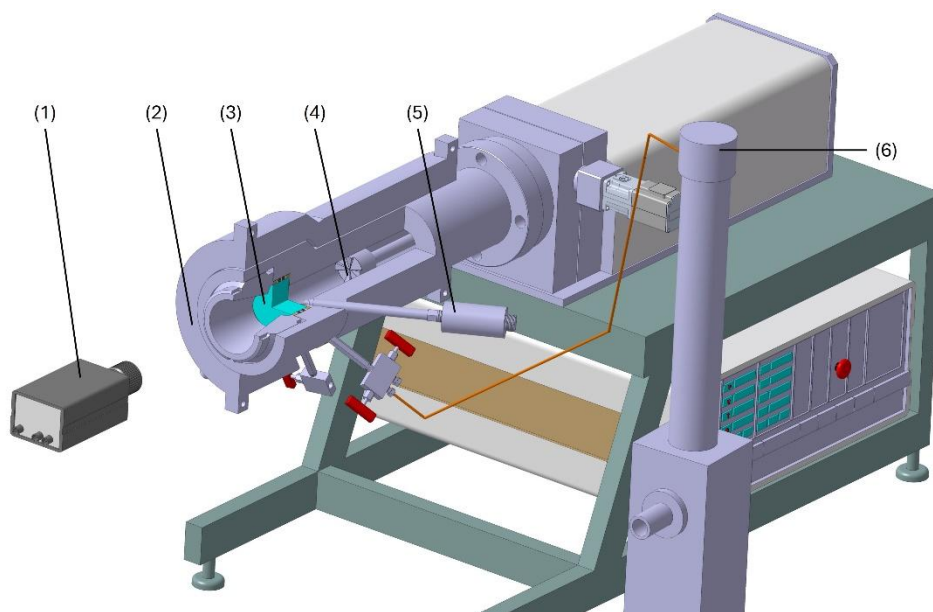
Figure 29. Schematic of the full-visibility high-pressure variable volume cell with coaxially coupled SWIR apparatus. (1) SWIR camera; (2) thermal jacket; (3) sapphire window; (4) stirrer at the end of the piston; (5) pressure transducer; and (6) syringe pump for gas injection. (Created by the author)

Similar to the last chapters, a synthetic method was applied to perform the study (Dohrn et al., 2024). Initially, the pressure inside the cell was reduced using a vacuum pump. Afterwards, the crude oil sample (BPs-1, BPs-2, or BPs-3) was heated at a constant temperature of $T = 333$ K for 24h to redissolve any waxy crystals prior to the transfer of the oil in the cell. Dead crude oil was gravimetrically introduced into the measurement cell, and the exact mass of the crude oil injected was determined using an analytical balance with an accuracy of 0.001 g. Subsequently, a syringe pump injected the required gas amount to reach a desirable global composition into the cell. The pressure and temperature in the syringe pump were monitored to guarantee constant density during injection. The displaced volume was converted to a mass injection using the density values obtained from the NIST REFPROP software (Linstrom; Mallard, 2001). Finally,

the mixture was heated to the desired temperature, and once the target temperature stabilized, the system pressure was increased. Depending on the global mole composition and temperature conditions, the system can be observed at high-pressure in a monophasic liquid state or as two liquid phases in equilibrium. The system was vigorously stirred once both pressure and temperature were stable to ensure mixture homogenization and equilibrium. Following this procedure, the expanding uncertainty regarding the mass of crude oil and gas injected was estimated to be better than 0.01 g and 0.005 g, respectively.

5.2.3   Constant mass expansion experiments

An isothermal depressurization was performed for all mixtures by continuously expanding cell volume at a depletion rate no higher than 0.3 MPa·min^{-1}. All mixtures were investigated in a temperature range from 308.15 to 373.15 K. During the experiments, the pressure, the volume, and the temperature conditions of the fluid inside the measurement cell were recorded. Based on this data, the *Y*-factor (equation 4.1) curves against pressure were drawn to determine the bubble point pressure (e.g. liquid to liquid-vapor or liquid-liquid to liquid-liquid-vapor).

$$Y_{factor} = -\frac{V_{initial}}{p_{initial}}\frac{(p-p_{initial})}{(V-V_{inital})} \tag{4.1}$$

where $V_{initial}$ and $p_{initial}$ denotes volume and pressure at the test initial condition.

Unlike the bubble point, liquid to liquid-liquid transitions results in minimal changes in the volumetric properties of the system, whether in the volume itself or its derivatives. Under these conditions, the *Y*-factor does not allow for the indirect detection of the appearance of a second liquid phase. Therefore, only direct visual observation allows for phase change detection. A dichotomous approach was used to determine the L to LL transition pressure, which involves moving back and forth from the single liquid phase to the two-phase LL equilibrium by progressively reducing the pressure steps using the visual SWIR approach mentioned above. Using the methodology described above, the estimated uncertainty using a conventional coverage factor $k_P = 2$ where liquid (L) to liquid-vapor (LV) is equal to 0.2 MPa; liquid (L) to liquid-liquid (LL) is equal to 0.6 MPa; and liquid-liquid (LL) to liquid-liquid-vapor (LLV) equal to 0.2 MPa. More information about the expanded uncertainty for LV, LL, and LLV is given in Appendix I.

5.2.4   Thermodynamic modeling

The classical Peng-Robinson (PR) equation of state (Peng; Robinson, 1976; Robinson; Peng, 1978) was employed to model the fluid-fluid phase transition experimentally measured in this work. The iso-fugacity criterion was applied as the primary condition to determine thermodynamic equilibrium. To achieve this, the fugacity coefficients of components in each phase were calculated using the PR EOS with a classical mixing rule as follows:

$$p = \frac{RT}{V_m - b} - \frac{a}{(V_m + b)(V_m - b)} \tag{4.2}$$

$$a = \sum_i \sum_j x_i x_j \sqrt{(a_i a_j)}(1 - k_{ij}) \tag{4.3}$$

$$b = \sum_i x_i b_i \tag{4.4}$$

where p denote the pressure, T is the temperature, R is the universal gas constant, V_m is the molar volume, x_i is the mole fraction of the component i in the mixture, a_i is the attractive parameter, b_i is the co-volume parameter, and k_{ij} represent the binary interaction parameter between the component i and j.

The attractive and co-volume parameters were calculated for each compound according to the following equations:

$$a_i = 0.45724 \frac{R^2 T_{c,i}^2}{p_{c,i}} \alpha_i(T) \tag{4.5}$$

$$b = 0.0778 \frac{RT_{c,i}}{p_{c,i}} \tag{4.6}$$

As presented in eq. 4.5, the temperature dependence on the attractive parameter is described by an α function, as shown in eq. 4.7.

$$\alpha_i(T) = \left[1 + m_i \left(1 - \sqrt{\frac{T}{T_{c,i}}} \right) \right]^2 \tag{4.7}$$

where m_i was calculated using the acentric factor ω_i according to following correlations:

$$m_i = 0.37464 + 1.54226\omega_i - 0.26992\omega_i^2 \quad if \ \omega < 0.49 \tag{4.8}$$

$$m_i = 0.379642 + 1.48503\omega_i - 0.164423\omega_i^2 + 0.016666\omega_i^3 \ \ if \ \omega \geq 0.49 \tag{4.9}$$

Critical properties such as critical temperature (T_c) and critical pressure (p_c), which are necessary for calculating the equation of state (EOS) parameters for pure components are listed in Table 13. While these physical constants are available for most pure components (Linstrom; Mallard, 2001), they remain unknown for the heavy fraction, that needs the prediction of critical parameters for these pseudo-components. To achieve this, the Lee-Kesler correlations (KESLER; LEE, 1976; Lee; Kesler, 1975) were applied to obtain T_c and critical pressure p_c associated with the heavy fraction C_{20+}. These correlations are expressed in the following forms:

$$T_c = 341.7 + 811.1\gamma + [0.4244 + 0.1174\gamma]T_b + \frac{[0.4669 - 3.26238\gamma]10^5}{T_b} \tag{4.10}$$

$$ln(p_c) = 8.3634 - \frac{0.0566}{\gamma} - \left[0.24244 + \frac{2.2898}{\gamma} + \frac{0.11857}{\gamma^2}\right]10^{-3}T_b + \left[1.4685 + \frac{3.648}{\gamma} + \right.$$

$$\left. \frac{0.47227}{\gamma^2}\right]10^{-7}T_b^2 - \left[0.42019 + \frac{1.6977}{\gamma^2}\right]10^{-10}T_b^3 \tag{4.11}$$

where γ represents the specific gravity of the C_{20+}. It can be noted that the boiling temperature (T_b) of the heavy fraction was used as an input parameter in addition to γ in these correlations. Since T_b is itself unknown, it must be predicted. For this purpose, the, the Riazi and Daubert correlation (Riazi; Daubert, 1987) was applied to determine the T_b of the C_{20+} as given in equation 4.12.

$$T_b = 6.77857(MM_{C20+})^{0.401673}\gamma^{-1.58262}exp[3.77409 * 10^{-3}(MM_{C20+}) +$$

$$2.984036\gamma - 4.25288 * 10^{-3}(MM_{C20+})\gamma] \tag{4.12}$$

where MW_{C20+} denotes the molecular weight of the C_{20+} fraction. Finally, the acentric factor to the C_{20+} fraction was also determined using the Lee-Kesler correlation, as given by equation 4.13.

$$\omega = \frac{-ln(p_c)-5.92714+6.09648\left(\frac{T_b}{T_c}\right)^{-1}+1.28862ln\left(\frac{T_b}{T_c}\right)-0.169347\left(\frac{T_b}{T_c}\right)^{6}}{15.2518-15.6875\left(\frac{T_b}{T_c}\right)^{-1}-13.4721\ln\left(\frac{T_b}{T_c}\right)+0.43577\left(\frac{T_b}{T_c}\right)^{6}}$$ (4.13)

with temperature in K and pressure in bar.

Table 13. Molecular weight and critical properties for carbon dioxide, methane and crude oil cuts.

component	MW	Tc / K	p_c / MPa	ω
CO_2	44.01	304.20	7.38	0.2250
C_1	16.04	190.60	4.60	0.0115
C_3	44.10	369.80	4.25	0.1454
i-C_4	58.12	408.10	3.65	0.1760
n-C_4	58.12	425.20	3.80	0.1928
i-C_5	71.89	465.83	3.50	0.2226
n-C_5	72.15	469.60	3.37	0.2273
C_6	84.00	512.55	3.35	0.2504
C_7	96.00	548.15	3.14	0.2848
C_8	107.00	576.35	2.97	0.3155
C_9	121.00	604.95	2.76	0.3535
C_{10}	134.00	629.85	2.60	0.3877
C_{11}	147.03	668.10	2.51	0.3932
C_{12}	159.90	690.21	2.39	0.4200
C_{13}	172.64	710.49	2.28	0.4459
C_{14}	185.22	729.22	2.19	0.4708
C_{15}	197.62	746.62	2.11	0.4949
C_{16}	209.83	762.87	2.04	0.5181
C_{17}	221.82	778.10	1.97	0.5407
C_{18}	233.59	792.45	1.91	0.5625
C_{19}	245.11	806.00	1.86	0.5837
C_{20+}: BPs-1	550.16	916.32	1.04	1.1395
C_{20+}: BPs-2	470.28	894.84	1.11	1.0780
C_{20+}: BPs-3	453.25	889.30	1.15	1.0535
HCF	550.78	1240.00	1.55	1.2000

Based on the results obtained in the last two chapters, it is highly probable that the observed dispersed liquid-liquid equilibrium is related to the properties of the

heavy fraction of the crude oil sample, particularly its asphaltene content. For this reason, to model the phase behavior observed in the mixtures investigated in this chapter, the C_{20+} fraction was divided into two parts: one consisting of standard C_{20+} and the other of a heavy condensed fraction (HCF). The amount of HCF extracted from the initial C_{20+} was established as the mass fraction of asphaltenes shown in Table 10. This quantity is deducted from the initial C_{20+} to create the two new fractions (C_{20+} and HCF). This procedure combines the approach in this chapter with the methodology reported by Yanes *et al.* (2020), who also employed an HCF to model the complex phase behavior observed in Brazilian pre-salt samples. Therefore, to maintain the predictive character of the PR EoS, the physical constants reported by Yanes *et al.* (2020) for the HCF have been kept in this chapter.

This combination of approaches was fundamental to modeling the liquid-liquid and liquid-liquid-vapor experimentally observed. Predicted phase diagrams comprising the liquid-vapor (LV), liquid-liquid (LL), and liquid-liquid-vapor (LLV) phase boundaries were obtained by performing a series of multiphasic flash calculations based on the Michelsen tangent plane distance method (Michelsen, 1982a, 1982b). Binary interaction parameters between carbon dioxide and methane with all crude oil fraction were fitted to experimental data to describe all phase transition measures, using the relative absolute deviation as the objective function, as follows:

$$obj_{function} = \sum_{i=1}^{N_{exp}} \left| \frac{(p^{calc} - p^{exp})}{p^{exp}} \right| \tag{14}$$

where the superscript $calc$ and exp denotes the transition pressure calculated and experimental, respectively.

5.2.5 Results and discussion

5.2.6 Experimental measurements of phase boundaries

Experimental data obtained for mixtures created by adding pure carbon dioxide to the oil samples BPs-1 and BPs-2 are presented in Table 14. For both systems, only a simple liquid (L) to liquid-vapor (LV) transition was identified until a global

composition of 60 mol% CO_2. The transition pressures are very similar for the same global mole composition BPs-1 and BPs-2. The occurrence of the vapor phase was easily identified and observed through direct fluid inspection using the SWIR camera, as shown in Figure 30. These data are depicted in several isopleth *pressure-temperature* (*p-T*) diagrams for each mixture, as shown in Figures 31 and 32 for BPs-1+CO_2 and BPs-2+CO_2, respectively.

Table 14. Fluid-fluid phase transition for mixtures of crude oil + CO_2 at a given temperature T in different mixtures of global composition $z_{CO_2} \pm U(z_{CO_2})$ in mol% with expanded uncertainty (k=2).

BPs-1 + CO_2								
$z_{CO_2} = 20.12 \pm 0.16\%$			$z_{CO_2} = 40.11 \pm 0.18\%$			$z_{CO_2} = 60.01 \pm 0.25\%$		
T/K	p/MPa	transition	T/K	p/MPa	transition	T/K	p/MPa	transition
308.15	2.17	L → LV	308.15	3.25	L → LV	308.15	6.03	L → LV
323.15	2.76	L → LV	323.15	4.20	L → LV	323.15	7.90	L → LV
338.15	3.33	L → LV	338.15	5.01	L → LV	338.15	10.12	L → LV
358.15	3.26	L → LV	358.15	6.17	L → LV	358.15	12.70	L → LV
373.15	3.35	L → LV	373.15	6.96	L → LV	373.15	14.48	L → LV

$z_{CO_2} = 70.00 \pm 0.25\%$			$z_{CO_2} = 75.23 \pm 0.25\%$		
T/K	p/MPa	transition	T/K	p/MPa	transition
303.15	45.10	L → LL	320.15	53.71	L → LL
308.15	29.29	L → LL	323.15	46.70	L → LL
313.15	23.16	L → LL	338.15	32.79	L → LL
323.15	21.07	L → LL	358.15	30.16	L → LV
338.15	19.97	L → LV	373.15	30.62	L → LV
358.15	22.66	L → LV	303.15	6.18	LL→ LLV
373.15	22.43	L → LV	308.15	6.93	LL→ LLV
303.15	6.26	LL→ LLV			
308.15	6.96	LL→ LLV			

BPs-2 + CO_2								
$z_{CO_2} = 20.31 \pm 0.16\%$			$z_{CO_2} = 39.86 \pm 0.28\%$			$z_{CO_2} = 59.96 \pm 0.25\%$		
T/K	p/MPa	transition	T/K	p/MPa	transition	T/K	p/MPa	transition
308.15	1.63	L → LV	308.15	3.94	L → LV	308.15	6.63	L → LV
323.15	1.98	L → LV	323.15	4.80	L → LV	323.15	8.46	L → LV
338.15	2.35	L → LV	338.15	5.64	L → LV	338.15	10.40	L → LV
358.15	2.82	L → LV	358.15	6.76	L → LV	358.15	12.83	L → LV
373.15	3.18	L → LV	373.15	7.61	L → LV	373.15	14.61	L → LV

$z_{CO_2} = 69.94 \pm 0.26\%$		
T/K	p/MPa	transition

303.15	32.61	L → LL
308.15	25.60	L → LL
323.15	19.11	L → LV
338.15	18.69	L → LV
358.15	20.38	L → LV
373.15	21.30	L → LV
303.15	6.08	LL→ LLV
308.15	7.14	LL→ LLV

*Expanded uncertainty for $U_{L \to LV}$, $U_{L \to LL}$, and $U_{LL \to LLV}$ are 0.21 MPa, 0.66 MPa, and 0.21 MPa, respectively.
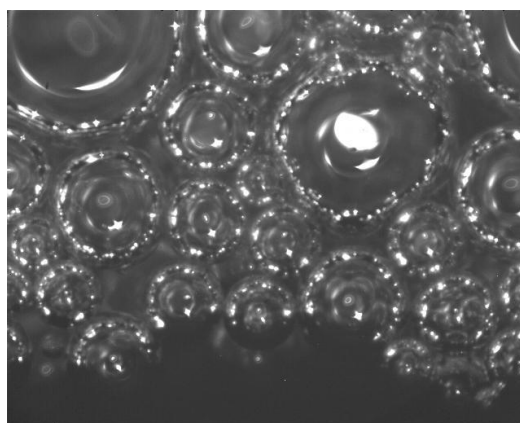
Figure 30. Liquid-vapor equilibrium for BPs-1 + CO_2 with 20.12 mol % CO_2 at $T = 323.15$ K.
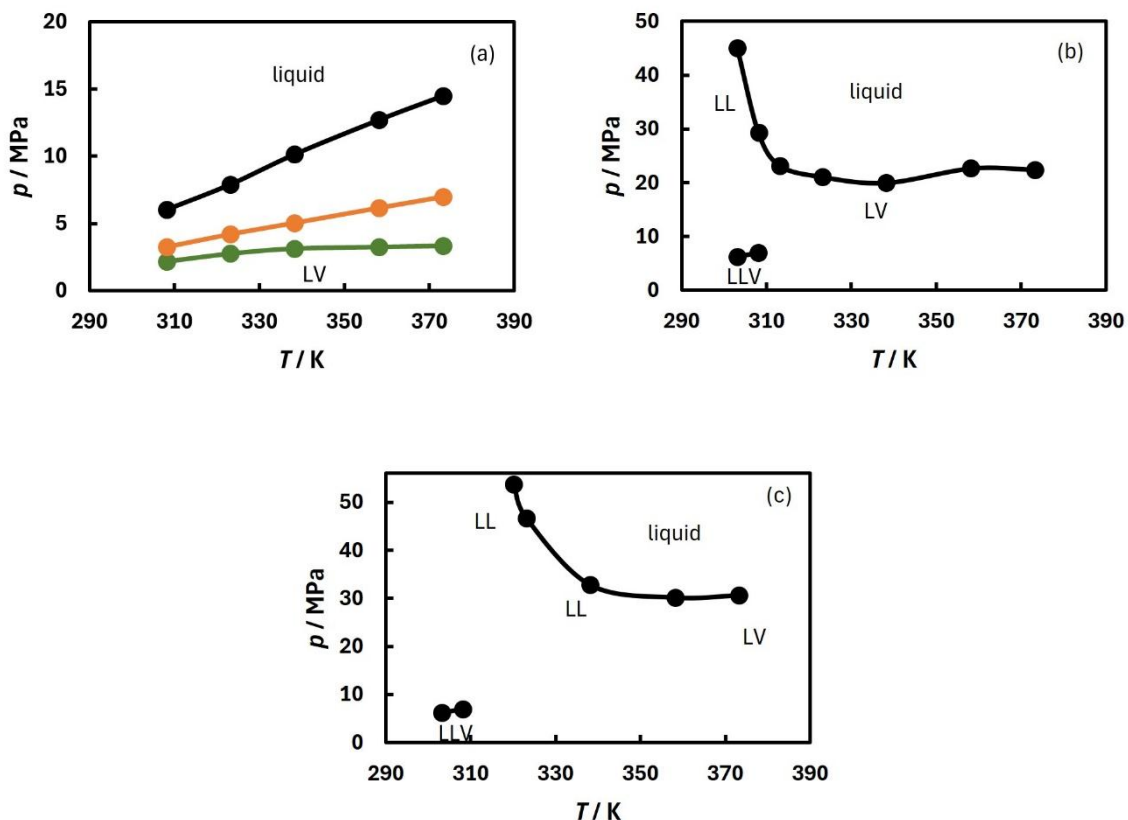
Figure 31. p-T diagram at different global compositions for BPs-1+CO_2 mixture. a) z_{CO_2} = 20.12 mol% (green circle, ●), z_{CO_2} = 40.11 mol% (orange circle, ●), and z_{CO_2} = 60.01 mol% (black circle, ●); b) z_{CO_2} = 70.00 mol%; and c) z_{CO_2} = 75.23 mol%.
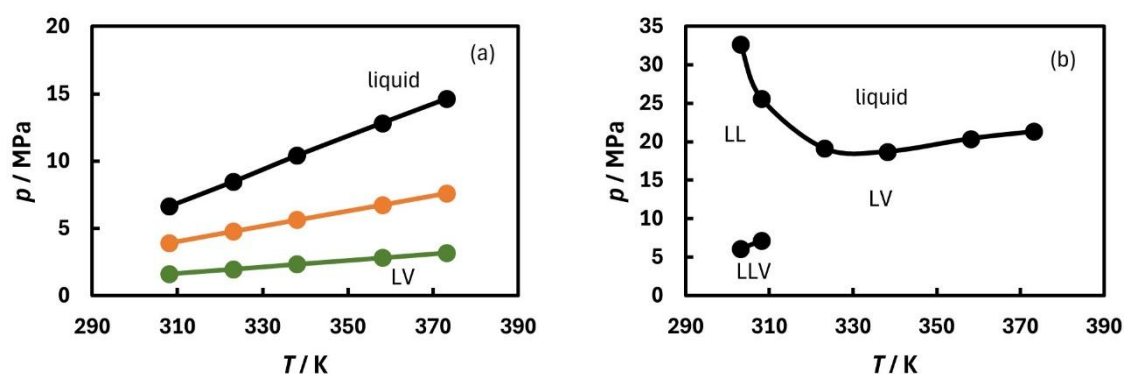
Figure 32. p-T diagram at different global compositions for BPs-2+CO_2 mixture. a) z_{CO_2} = 20.31 mol% (green circle, ●), z_{CO_2} = 39.86 mol% (orange circle, ●), and z_{CO_2} = 59.96 mol% (black circle, ●); b) z_{CO_2} = 69.94 mol%.

Regime changes in the *Y*-factor curve against pressure also detected the bubble point pressure, denoting a more compressible phase formation, typical of a vapor phase. Nevertheless, for mixtures with 70 mol% CO_2 and beyond, the carbon dioxide became partly miscible in the BPs-1 and BPs-2. Therefore, the system presents a liquid-liquid phase heterogeneity at temperatures higher than the CO_2 critical temperature. The detected liquid (L) to liquid-liquid transition (LL) reveals that both systems investigated with CO_2 present a Type III shape following the classification proposed by Van Konynenburg and Scott (1980), and this can be assigned to the high asymmetry and property differences between the CO_2 and the heavy hydrocarbon fraction present in crude oil. In contrast to the bubble point, the transition from a single liquid phase to liquid-liquid equilibrium (square symbol ■ in Figure 33a) does not result in any break in the *Y*-factor curve. This L→LL transition was only detected by direct observation using the SWIR apparatus, where the dark liquid drops cause a smooth SWIR light dispersion. Here, the LLE does not present any phase segregation, even after hours of equilibration, suggesting a somewhat comparable density between phases.

Figure 33b presents a snapshot of the LLE for BPs-1+CO_2 with 70 mol% at p = 20.2 MPa and T = 308.15 K using a 4x magnification objective. In this figure, the dispersed liquid droplets exhibit an appearance very similar to gas bubbles from a visual perspective. Consequently, by observing only a static image, liquid-liquid equilibrium can easily be mistaken for liquid-vapor equilibrium. However, by activating the stirrer and recording a video, it becomes clear that in the case of liquid-vapor equilibrium, the bubbles consistently rise vertically and rapidly. In contrast, in liquid-liquid equilibrium, the droplets follow the rotational movement of the stirrer. Moreover, by combining both SWIR inspection and the *Y*-factor curve, it can be stated that it is a liquid to liquid-liquid transition. At the same temperature, the mixture goes from a liquid-liquid equilibrium to a three-phase liquid-liquid-vapor equilibrium (LLVE) as pressure decrease, which is indicated by the sharp drop in the *Y*-factor curve at pressure near 7.0 MPa. This three-phase equilibrium extends until T = 308.15 K, 4 K higher than the CO_2 critical temperature. In addition, it can be noted that the LLV sites maintained the same pressure conditions across different global mole compositions, which may indicate a plateau in the pressure-composition (*p-z*) diagram. This type of behavior regarding the LLV transition in crude oil + CO_2 systems can be classified as a Type III diagram, which may be related to the lack of lighter compounds in the mixture.
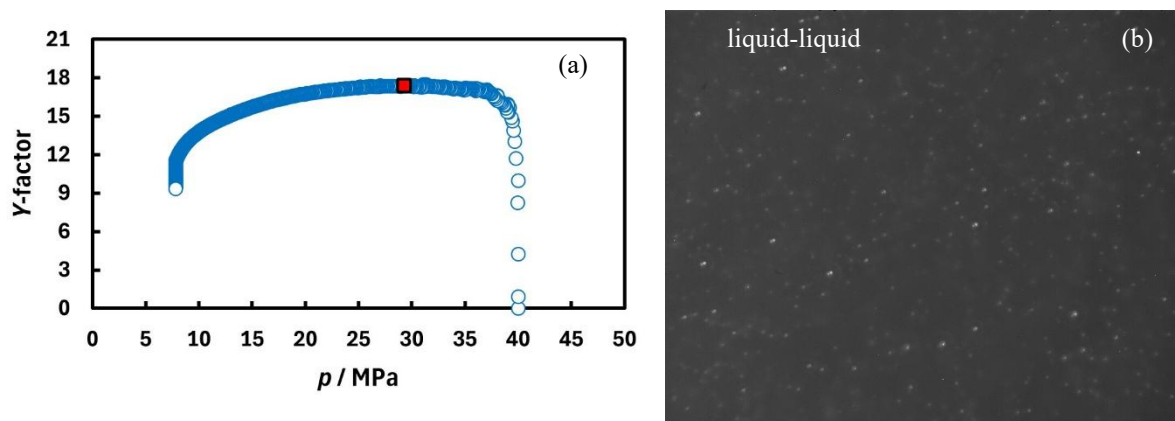
Figure 33. a) *Y-factor* against pressure for BPs-1+CO_2 system with z_{CO_2} = 70.00 mol% at a fixed temperature T = 308.15 K; b) liquid-liquid equilibrium observed at T = 308.15 and p = 12.90 MPa.

Based on these initial results, a qualitative comparison can be drawn between the liquid-liquid transitions observed in this chapter and those described in Chapters II and III. Once again, it appears that an excess of CO_2 is required to induce a liquid-liquid split (about z_{CO_2} ≥ 70 mol % CO_2), highlighting the significant role of asymmetry in triggering this phase transition. Although the shape of the phase diagram for mixtures with CO_2 is similar to those obtained for binary mixtures of *n*-alkanes + CO_2 with a comparable global composition (Cismondi et al., 2012; Daridon et al., 2021; Enick; Holder; Morsi, 1985; Fall; Fall; Luks, 1985; Fall; Luks, 1985; Hottovy; Luks; Kohn, 1981; Rodriguez-reartes et al., 2009; Vitu et al., 2008b; Yanes; Montel; Daridon, 2022a), which generally occurs at low temperatures, the LLE observed in this study extends up to T = 338.15 K for BPs-1 + CO_2 with 75.23 mol% gas, this demonstrates that the addition of gas shifts the LL loci to higher temperatures. However, above T = 308.15 K, only a critical change from LL to LV was observed. This certainly reveals the existence of a critical end point in the vicinity of 308 K.

Although the BPs-1 and BPs-2 samples have similar compositions and S.A.R.A distribution, they differ regarding asphaltene precipitation. For global compositions higher than 70 mol% CO_2, the BPs-2 + CO_2 mixture begins to present a solid phase with a high affinity for adhering to the polar sapphire window surface of the PVT cell, typical of asphaltenes (Cardoso et al., 2015; Mohammadi et al., 2015; Romero Yanes et al., 2020a, 2019b), while for BPs-1 + CO_2, none experimental observation regarding asphaltene was detected in global composition range investigated. This solid

phase prevents accurately determining the L to LL transition, as it is detected only through SWIR inspection. Therefore, these data are not included, and the higher compositions are not investigated for BPs-2 + CO_2.

Subsequently, the measurements were repeated under the same conditions, but with pure methane instead of CO_2. All phase transition data experimentally measured for mixtures with CH_4 are listed in Table 15 and illustrated in Figure 34. A series of isothermal CME tests are carried out for BPs-1 and BPs-2 with the addition of CH4, revealing that only the LV transition occurs until a global composition of up to 70 mol% CH_4 at different temperatures.

Table 15. Fluid-fluid phase transition for mixtures of crude oil + CH_4 at a given temperature T in different mixtures of global composition $z_{CH_4} \pm U(z_{CH_4})$ in mol% with expanded uncertainty (k=2).

BPs-1+ CH$_4$								
$z_{CH_4} = 19.93 \pm 0.16\%$			$z_{CH_4} = 40.04 \pm 0.18\%$			$z_{CH_4} = 60.49 \pm 0.25\%$		
$T/$K	$p/$MPa	transition	$T/$K	$p/$MPa	transition	$T/$K	$p/$MPa	transition
308.15	5.93	L → LV	308.15	16.58	L → LV	308.15	42.82	L → LV
323.15	6.30	L → LV	323.15	17.25	L → LV	323.15	42.11	L → LV
338.15	6.57	L → LV	338.15	17.84	L → LV	338.15	41.88	L → LV
358.15	6.97	L → LV	358.15	18.54	L → LV	358.15	41.39	L → LV
373.15	7.21	L → LV	373.15	18.96	L → LV	373.15	41.06	L → LV
$z_{CH_4} = 70.07 \pm 0.26\%$			$z_{CH_4} = 75.91 \pm 0.25\%$					
$T/$K	$p/$MPa	transition	$T/$K	$p/$MPa	transition			
308.15	63.74	L → LV	308.15	84.00	LL→ LLV			
323.15	61.54	L → LV	323.15	79.90	LL→ LLV			
338.15	59.59	L → LV	338.15	76.02	LL→ LLV			
358.15	57.32	L → LV	358.15	72.07	LL→ LLV			
373.15	56.47	L → LV	373.15	69.10	LL→ LLV			
BPs-2 + CH$_4$								
$z_{CH_4} = 19.87 \pm 0.16\%$			$z_{CH_4} = 39.87 \pm 0.18\%$			$z_{CH_4} = 59.99 \pm 0.25\%$		
$T/$K	$p/$MPa	transition	$T/$K	$p/$MPa	transition	$T/$K	$p/$MPa	transition
308.15	5.18	L → LV	308.15	14.36	L → LV	308.15	37.17	L → LV
323.15	5.51	L → LV	323.15	15.28	L → LV	323.15	36.97	L → LV
338.15	5.91	L → LV	338.15	15.69	L → LV	338.15	36.74	L → LV
358.15	6.33	L → LV	358.15	16.60	L → LV	358.15	36.69	L → LV
373.15	6.56	L → LV	373.15	17.05	L → LV	373.15	36.61	L → LV
$z_{CH_4} = 70.00 \pm 0.25\%$			$z_{CH_4} = 74.97 \pm 0.26\%$			$z_{CH_4} = 79.99 \pm 0.23\%$		
$T/$K	$p/$MPa	transition	$T/$K	$p/$MPa	transition	$T/$K	$p/$MPa	transition

308.15	58.77	L → LV	308.15	73.55	LL→ LLV	358.15	79.36	LLA → LLAV
323.15	55.65	L → LV	323.15	69.94	LL→ LLV	373.15	77.41	LLA → LLAV
338.15	54.10	L → LV	338.15	67.88	LL→ LLV			
358.15	52.63	L → LV	358.15	64.14	LL→ LLV			
373.15	51.62	L → LV	373.15	62.44	LL→ LLV			

*Expanded uncertainty for $U_{L→LV}$, $U_{L→LL}$, and $U_{LL→LLV}$ are 0.21 MPa, 0.66 MPa, and 0.21, respectively.
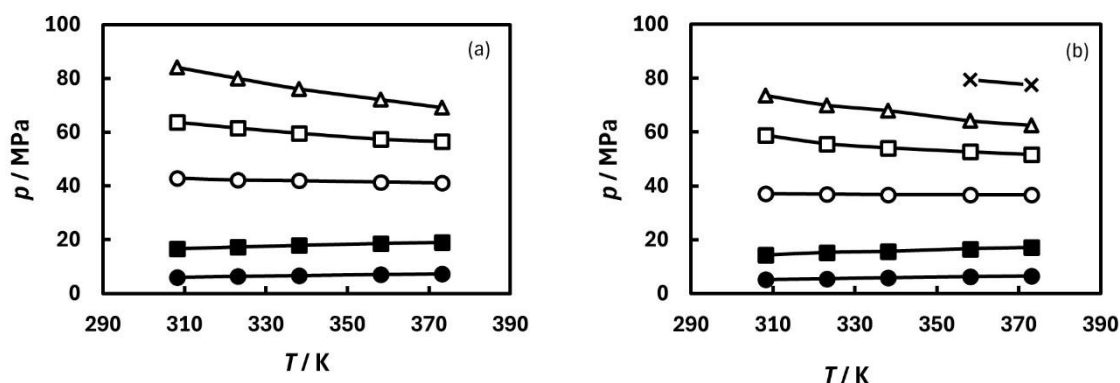
Figure 34. *p-T* diagrams for BPs-1 and BPs-2 with methane at different global composition. a) BPs-1 + CH4: z_{CH_4} = 19.93 mol% (black circle, ●), z_{CH_4} = 40.04 mol% (black square, ■), z_{CH_4} = 60.49 mol% (empty circle,○), z_{CH_4} = 70.07 mol% (empty square, □), and z_{CH_4} = 75.91 mol% (empty triangle, Δ); b) BPs-2 + CH4 : z_{CH_4} = 19.87 mol% (black circle, ●), z_{CH_4} = 39.87 mol% (black square, ■), z_{CH_4} = 59.99 mol% (empty circle,○), z_{CH_4} = 70.00 mol% (empty square, □), z_{CH_4} = 75.95 mol% (empty triangle, Δ), and z_{CH_4} = 79.99 mol% (**x**).

When the BPs-1 and BPs-2 samples were investigated with a molar composition close to 75 mol% CH4, the system was not monophasic, even under high-pressure conditions regardless of the temperature within the investigated range. This heterogeneous state was associated with a dispersed liquid-liquid equilibrium (LLE), which was only detected through SWIR inspection (Figure 35a). Similar to the LLE detected for mixtures with CO2, it appears as a mist which does not present any phase segregation by gravity force, even after a long equilibration time. Therefore, no straightforward interface could be observed between these liquid phases. This observation suggests that phases present a similar density even by adding methane instead of carbon dioxide, avoiding phase segregation. Moreover, this LLE was observed until the temperature of T = 373.15 K. When the CME test is performed, an apparent change in the

Y-factor curve can be observed, indicating that the biphasic LLE passes to an LLVE in such high-pressure conditions, as exemplified in Figure 36 for mixture BPs-2 + CH₄. Using $T = 323.15$ K as an example, at bubble point pressure, the vapor bubble moving to the top of the PVT cell (bright dots in Figure 35b) could be observed, demonstrating the low density of the vapor phase. Similar behaviors were observed in all temperatures investigated.
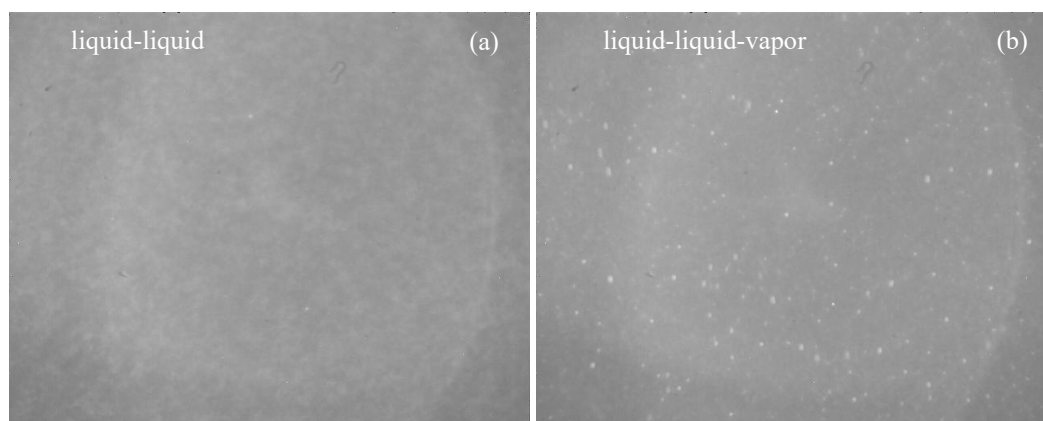
Figure 35. SWIR inspection for BPs-2 + CH₄ with 75.95 mol %. a) LLE observed at $T = 323.15$ K and $p = 80.00$ MPa, and b) LLVE observed at $T = 323.15$ K and $p = 65.50$ MPa.
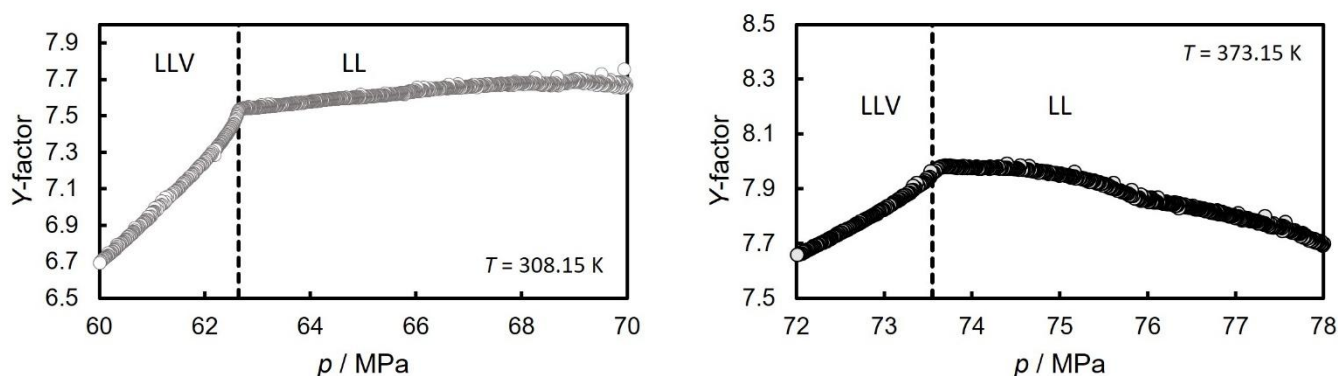
Figure 36. *Y-factor* against pressure for BPs-2 + CH₄ with 75.95 mol% at two different temperature conditions.

As the system with a molar composition close to 75 mol% CH₄ consistently exhibited a liquid-liquid phase behavior at all pressures and temperatures studied and with both dead oils, it was not possible to determine the transition conditions from liquid to liquid-liquid in these mixtures. With the addition of 70% methane, the system remained

entirely liquid at high pressure, regardless of the temperature. In contrast, with 75% methane content, the system consistently exhibited a liquid-liquid phase separation. This indicates that the transition from liquid to liquid-liquid must have a very steep slope in the pressure-composition diagram. To accurately detect this transition, it would be necessary to conduct measurements between 70% and 75% by varying the composition by just a few percent. However, this would require a considerable number of time-consuming measurements at high pressure. Therefore, in the *p-z* diagram reported in Figure 37, this transition is represented as a virtual boundary around 72.5 mol%.
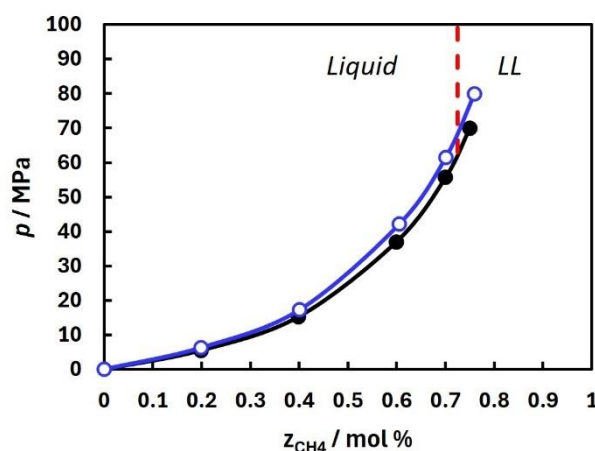
Figure 37. *p-z* diagram obtained for BPs-1 (empty circle) and BPs-2 (full circle) with methane at *T* = 325.15 K

Comparing and contrasting these pseudo-binary systems with binary mixtures reported in the literature, the LL loci observed for *n*-alkanes + CH_4 are limited to hydrocarbons up to *n*-heptane (Chen; Chappelear; Kobayashi, 1976; Hottovy; Kohn; Luks, 1982; Lin; Hwang; Kobayashi, 1978; Preston; Funk; Prausnitz, 1971). This significant difference between the phase behavior observed here and that of binary mixtures containing a heavy alkane in addition to methane indicates that such binary mixtures cannot serve as effective model mixtures to describe the behavior of Brazilian pre-salt fluids. This comparison suggests that the characteristics of the heavy fraction have a substantial impact on the shape of the phase diagram, potentially explaining the existence of the liquid-liquid transition even in the absence of CO_2.

One final composition was investigated for BPs-2 + CH_4, corresponding to 79.99 mol% CH_4. For this composition, the system remains multiphasic in a LLVE up to

a temperature near $T = 353.15$ K. At this temperature and above ($T = 373.15$ K), a solid asphaltenic phase (A), adhering to the sapphire window (bright dots in Figure 38), was observed within the LLE region, indicating that the mixture now exhibits a three-phase liquid-liquid-asphaltene equilibrium (LLAE). This means that CO_2 has a more pronounced effect on asphaltene destabilization than CH_4 for BPs-2. This behavior is unexpected, since CH_4 normally has a more pronounced effect on asphaltene destabilization. However, considering the appearance of the second liquid phase, it can be suggested that the second liquid phase is capable of solubilizing asphaltenes, concentrating them in its composition. Furthermore, despite the destabilization of the asphaltenes, it did not alter the mixture phase equilibria, remaining the LLE at pressures above the bubble point. The bubble point pressure was measured only at these two temperatures, revealing a liquid-liquid-asphaltene-vapor equilibrium (LLAVE), while at temperatures lower than $T = 353.15$ K, only a critical LLA to LVA transition occurs.
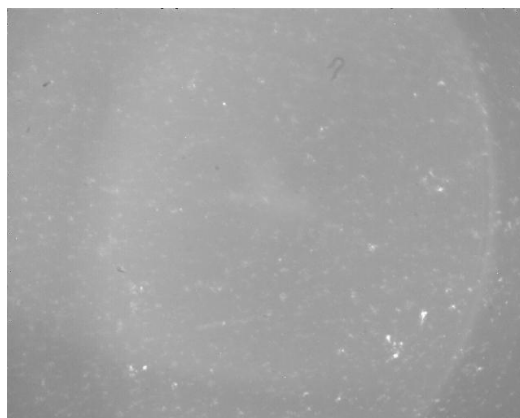
Figure 38. Liquid-liquid-asphaltene equilibrium (LLAE) observed by SWIR inspection for BPs-2 + CH_4 with 79.99 mol% at $T = 353.15$ K and $p = 84.00$ MPa

Studies conducted on both crude oils with CO_2 and CH_4 have demonstrated the emergence of liquid-liquid transitions at high gas content. Regardless of the gas used, the appearance of these liquid-to-liquid transitions did not align with the observations made in simple binary mixtures where the heavy fraction is replaced by a heavy alkane.

To further the understanding of this type of system and the impact of gas, the measurements were repeated using mixtures of the two gases. Two specific mixtures were prepared containing both CO_2 and CH_4 was considered to reproduce gas composition of Brazilian pre-salt live oil with high CO2 content. To achieve this, two different gas

mixtures with distinct molar compositions were used, referred to as gas-3 and gas-4. Gas-3 has a 75.3% CH_4 and 24.7% CO_2 molar fraction, while gas-4 comprises a 1:1 molar ratio of CH_4 and CO_2. Additionally, to extend the study, another crude oil sample, named BPs-3, was evaluated by adding these gas mixtures, and its phase behavior was compared with that of BPs-1 and BPs-2. Phase transition data for the mixtures with gas-3 and gas-4 are presented in Tables 16 and 17, respectively.

Table 16. Fluid-fluid phase transition for mixtures crude oil + gas-3 at a given temperature T in different mixtures of global composition $z_{gas-3} \pm U(z_{gas-3})$ in mol% with expanded uncertainty (k=2).

BPs-1 + gas-3								
$z_{gas-3} = 23.36 \pm 0.18\%$			$z_{gas-3} = 45.00 \pm 0.18\%$			$z_{gas-3} = 64.78 \pm 0.24\%$		
T/K	p/MPa	transition	T/K	p/MPa	transition	T/K	p/MPa	transition
308.15	5.88	L → LV	308.15	16.18	L → LV	308.15	38.02	L → LV
323.15	6.16	L → LV	323.15	17.45	L → LV	323.15	38.15	L → LV
338.15	6.61	L → LV	338.15	18.16	L → LV	338.15	38.47	L → LV
358.15	7.16	L → LV	358.15	19.03	L → LV	358.15	38.85	L → LV
373.15	7.67	L → LV	373.15	19.42	L → LV	373.15	39.13	L → LV
$z_{gas-3} = 74.11 \pm 0.23\%$								
T/K	p/MPa	transition						
308.15	61.57	LL→ LLV						
323.15	60.44	LL→ LLV						
338.15	59.02	LL→ LLV						
358.15	57.82	LL→ LLV						
373.15	56.68	LL→ LLV						
BPs-2+ gas-3								
$z_{gas-3} = 23.09 \pm 0.18\%$			$z_{gas-3} = 45.08 \pm 0.18\%$			$z_{gas-3} = 64.80 \pm 0.24\%$		
T/K	p/MPa	transition	T/K	p/MPa	transition	T/K	p/MPa	transition
308.15	5.37	L → LV	308.15	14.86	L → LV	308.15	35.54	L → LV
323.15	5.81	L → LV	323.15	15.71	L → LV	323.15	35.76	L → LV
338.15	6.20	L → LV	338.15	16.41	L → LV	338.15	35.93	L → LV
358.15	6.69	L → LV	358.15	17.33	L → LV	358.15	36.21	L → LV
373.15	7.02	L → LV	373.15	18.00	L → LV	373.15	36.71	L → LV
$z_{gas-3} = 72.82 \pm 0.25\%$			$z_{gas-3} = 81.24 \pm 0.19\%$					
T/K	p/MPa	transition	T/K	p/MPa	transition			
308.15	52.84	L → LV	308.15	78.87	LLA → LLAV			
323.15	51.82	L → LV	323.15	75.34	LLA → LLAV			
338.15	50.66	L → LV	338.15	72.48	LLA → LLAV			
358.15	49.78	L → LV	358.15	69.79	LLA → LLAV			

| 373.15 | 49.30 | L → LV | 373.15 | 67.86 | LLA → LLAV |

BPs-3 + gas-3								
$z_{gas-3} = 23.49 \pm 0.18\%$			$z_{gas-3} = 45.03 \pm 0.18\%$			$z_{gas-3} = 62.23 \pm 0.25\%$		
T/ K	p/ MPa	transition	T/ K	p/ MPa	transition	T/ K	p/ MPa	transition
308.15	4.83	L → LV	308.15	13.70	L → LV	308.15	30.26	L → LV
323.15	5.21	L → LV	323.15	14.61	L → LV	323.15	30.54	L → LV
338.15	5.58	L → LV	338.15	15.34	L → LV	338.15	31.05	L → LV
358.15	6.11	L → LV	358.15	16.18	L → LV	358.15	31.86	L → LV
373.15	6.40	L → LV	373.15	16.66	L → LV	373.15	32.18	L → LV
$z_{gas-3} = 71.32 \pm 0.20\%$			$z_{gas-3} = 80.57 \pm 0.17\%$					
T/ K	p/ MPa	transition	T/ K	p/ MPa	transition			
308.15	47.62	L → LV	308.15	77.52	LLA → LLAV			
323.15	47.19	L → LV	323.15	73.06	LLA → LLAV			
338.15	46.61	L → LV	338.15	70.28	LLA → LLAV			
358.15	46.30	L → LV	358.15	67.89	LLA → LLAV			
373.15	45.82	L → LV	373.15	66.31	LLA → LLAV			

*Expanded uncertainty for $U_{L\to LV}$, $U_{L\to LL}$, and $U_{LL\to LLV}$ are 0.21 MPa, 0.66 MPa, and 0.21, respectively.

Table 17. Fluid-fluid phase transition for mixtures crude oil + gas-4 at a given temperature T in different mixtures of global composition $z_{gas-4} \pm U(z_{gas-4})$ in mol% with expanded uncertainty (k=2).

BPs-1 + gas-4								
$z_{gas-4} = 13.43 \pm 0.12\%$			$z_{gas-4} = 17.62 \pm 0.11\%$			$z_{gas-4} = 31.99 \pm 0.23\%$		
T/ K	p/ MPa	transition	T/ K	p/ MPa	transition	T/ K	p/ MPa	transition
308.15	1.96	L → LV	308.15	2.82	L → LV	308.15	6.87	L → LV
323.15	2.21	L → LV	323.15	3.10	L → LV	323.15	7.40	L → LV
338.15	2.40	L → LV	338.15	3.67	L → LV	338.15	8.11	L → LV
358.15	2.68	L → LV	358.15	4.00	L → LV	358.15	8.75	L → LV
373.15	2.90	L → LV	373.15	4.25	L → LV	373.15	9.24	L → LV
$z_{gas-4} = 43.42 \pm 0.29\%$			$z_{gas-4} = 58.05 \pm 0.29\%$			$z_{gas-4} = 69.79 \pm 0.26\%$		
T/ K	p/ MPa	transition	T/ K	p/ MPa	transition	T/ K	p/ MPa	transition
308.15	10.89	L → LV	308.15	19.94	L → LV	308.15	38.10	L → LV
323.15	12.00	L → LV	323.15	22.20	L → LV	323.15	38.17	L → LV
338.15	12.78	L → LV	338.15	22.75	L → LV	338.15	38.36	L → LV
358.15	13.94	L → LV	358.15	24.03	L → LV	358.15	38.74	L → LV
373.15	14.75	L → LV	373.15	25.03	L → LV	373.15	39.17	L → LV
$z_{gas-4} = 74.75 \pm 0.26\%$								
T/ K	p/ MPa	transition						
308.15	52.14	LL→ LLV						
323.15	49.58	LL→ LLV						
338.15	48.38	LL→ LLV						
358.15	47.76	LL→ LLV						
373.15	47.73	LL→ LLV						

BPs-2 + gas-4								
z_{gas-4} = 19.96 ± 0.16%			z_{gas-4} = 39.91 ± 0.18%			z_{gas-4} 59.95 ± 0.25%		
T/K	p/MPa	transition	T/K	p/MPa	transition	T/K	p/MPa	transition
308.15	3.26	L → LV	308.15	8.64	L → LV	308.15	19.35	L → LV
323.15	3.66	L → LV	323.15	9.54	L → LV	323.15	20.98	L → LV
338.15	3.99	L → LV	338.15	10.18	L → LV	338.15	22.28	L → LV
358.15	4.45	L → LV	358.15	11.05	L → LV	358.15	23.54	L → LV
373.15	4.72	L → LV	373.15	11.72	L → LV	373.15	24.39	L → LV
z_{gas-4} = 69.98 ± 0.25%			z_{gas-4} = 74.95 ± 0.26%			z_{gas-4} = 79.76 ± 0.23%		
T/K	p/MPa	transition	T/K	p/MPa	transition	T/K	p/MPa	transition
308.15	33.05	L → LV	308.15	43.28	LL→ LLV	308.15	58.64	LLA → LLAV
323.15	33.49	L → LV	323.15	42.55	LL→ LLV	323.15	54.63	LLA → LLAV
338.15	33.77	L → LV	338.15	42.13	LL→ LLV	338.15	53.70	LLA → LLAV
358.15	34.96	L → LV	358.15	42.43	LL→ LLV	358.15	52.51	LLA → LLAV
373.15	35.83	L → LV	373.15	42.52	LL→ LLV	373.15	52.03	LLA → LLAV
BPs-3 + gas-4								
z_{gas-4} = 20.07 ± 0.16%			z_{gas-4} = 40.00 ± 0.18%			z_{gas-4} = 59.99 ± 0.25%		
T/K	p/MPa	transition	T/K	p/MPa	transition	T/K	p/MPa	transition
308.15	3.67	L → LV	308.15	9.41	L → LV	308.15	21.05	L → LV
323.15	4.13	L → LV	323.15	10.33	L → LV	323.15	22.47	L → LV
338.15	4.40	L → LV	338.15	11.16	L → LV	338.15	23.69	L → LV
358.15	4.88	L → LV	358.15	12.29	L → LV	358.15	25.21	L → LV
373.15	5.25	L → LV	373.15	12.99	L → LV	373.15	26.04	L → LV
z_{gas-4} = 69.97 ± 0.26%			z_{gas-4} = 74.99 ± 0.26%			z_{gas-4} = 79.99 ± 0.23%		
T/K	p/MPa	transition	T/K	p/MPa	transition	T/K	p/MPa	transition
308.15	36.35	L → LV	308.15	48.29	LL→ LLV	308.15	63.25	LLA → LLAV
323.15	36.72	L → LV	323.15	46.93	LL→ LLV	323.15	60.24	LLA → LLAV
338.15	36.84	L → LV	338.15	46.32	LL→ LLV	338.15	57.81	LLA → LLAV
358.15	37.69	L → LV	358.15	46.16	LL→ LLV	358.15	55.79	LLA → LLAV
373.15	38.03	L → LV	373.15	46.18	LL→ LLV	373.15	55.18	LLA → LLAV
z_{gas-4} = 83.49 ± 0.21%								
T/K	p/MPa	transition						
323.15	80.72	LLA → LLAV						
338.15	68.72	LLA → LLAV						
358.15	65.87	LLA → LLAV						
373.15	63.86	LLA → LLAV						

[*]Expanded uncertainty for $U_{L\to LV}$, $U_{L\to LL}$, and $U_{LL\to LLV}$ are 0.21 MPa, 0.66 MPa, and 0.21, respectively.

The transition pressures measured for mixtures with gas-3 and gas-4 are presented in the form of isothermal *p-z* diagrams in Figures 39 and 40, respectively. For BPs-1 and BPs-2, the fluid phase behavior is very similar to that of mixtures with pure CH_4, with only LV transitions for mixtures until 70 mol% gas. Moreover, when crude oil

samples are examined at high gas content for gas-3 and gas-4, the same LLE is observed at high pressure and high-temperature conditions. Similarly, the LLE evolves to an LLVE in the temperature domain investigated. The addition of CO_2 in the gas mixture decreases the LLV transition pressure, and this reduction in the transition pressure allows the investigation of more global compositions.

Furthermore, the minimum composition to observe the dispersed LLE was almost the same as that of the system with pure CH_4. Moreover, an interesting behavior regarding asphaltene flocculation was observed, as the asphaltenic phase was only noted at a global mole composition similar to those observed for mixtures with pure CH_4, mainly for sample BPs-2. This type of result shows that, even when adding a gas mixture ($CH4 + CO2$), the second liquid phase formed stabilizes the asphaltenes in its composition, and asphaltene flakes are only observed when excess gas is added to the mixture, forcing them out of solution. Furthermore, based on these results and the shape of the pressure-temperature diagram, it can be concluded that the asymmetry between CH_4 and the heavy hydrocarbon fraction significantly influences the emergence of the liquid-liquid domain observed at high temperatures. Contrary to initial expectations, these interactions between methane and the heavy fraction appear to be more responsive than those involving CO_2 to explain the specific behavior of the Brazilian pre-salt fluids.
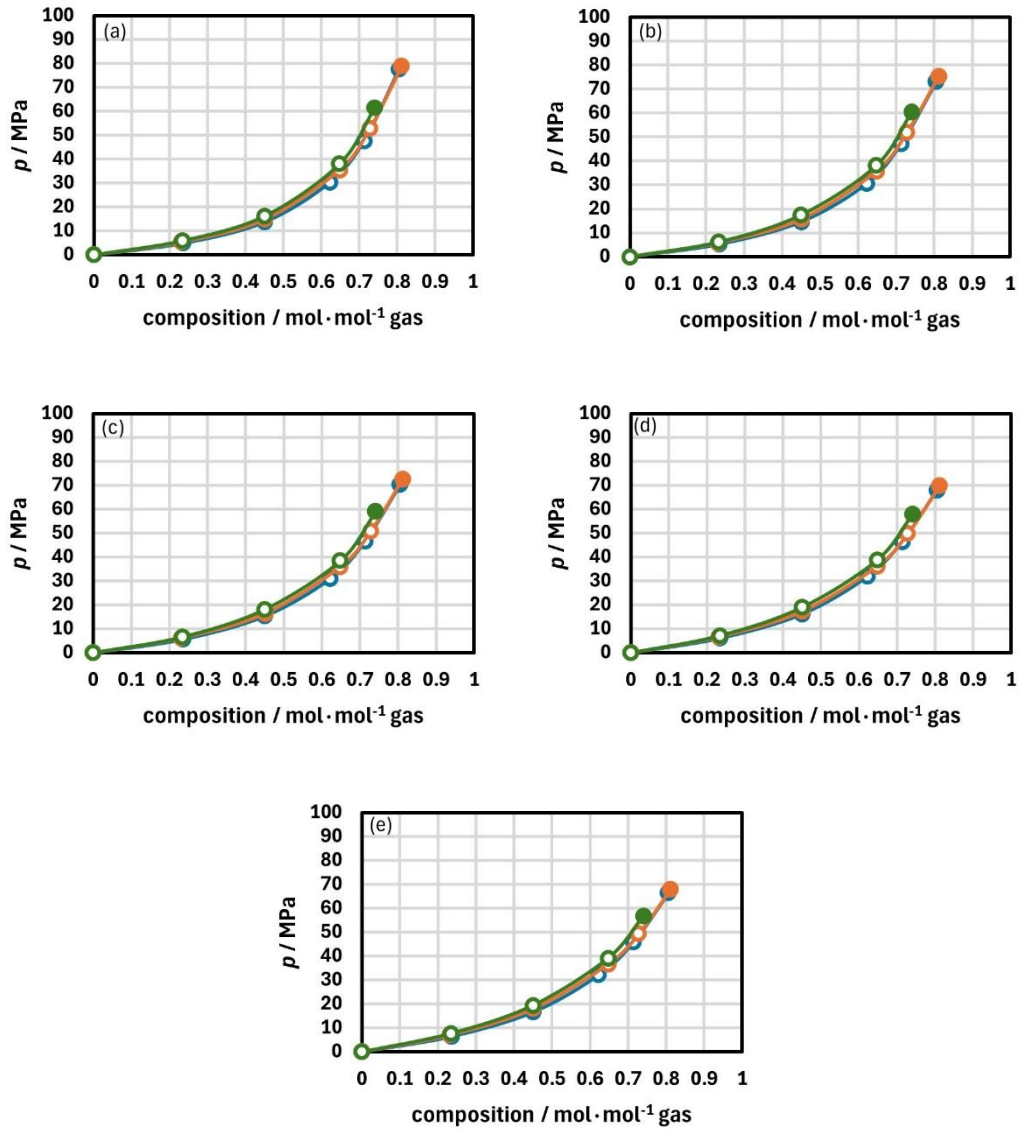
Figure 39. Isothermal p-z_{gas-3} diagrams for BPs-1 (green, ●), BPs-2 (orange, ●), and BPs-3 (blue, ●), with gas-3 at different global composition; T = 308.15 K (a), T = 323.15 K (b), T = 338.15 K (c), T = 358.15 K (d), T = 373.15 K (e); LV (empty circle) and LLV (full circle).
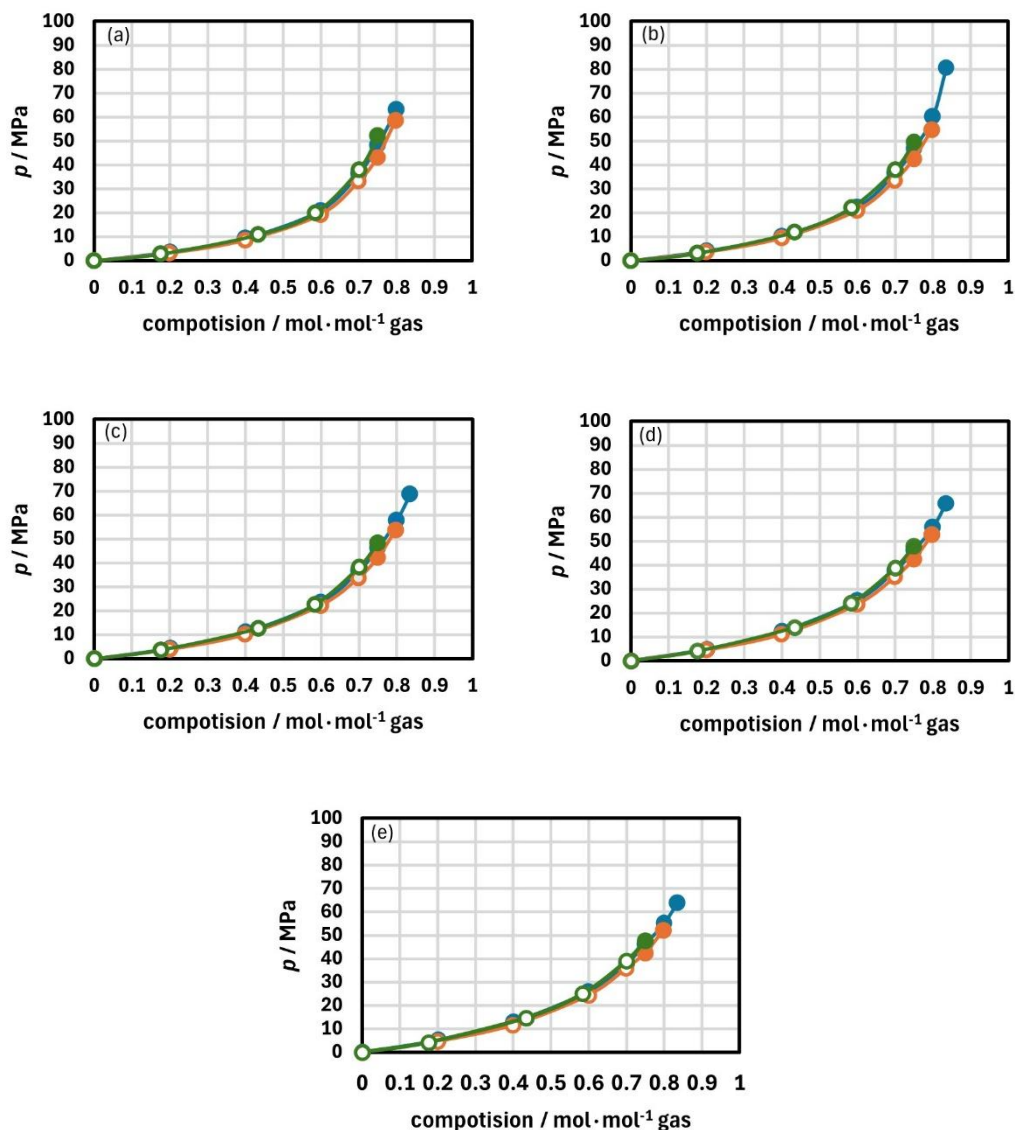
Figure 40. Isothermal p-z_{gas-4} diagrams for BPs-1 (green, ●), BPs-2 (orange, ●), and BPs-3 (blue, ●), with gas-3 at different global composition; $T = 308.15$ K (a), $T = 323.15$ K (b), $T = 338.15$ K (c), $T = 358.15$ K (d), $T = 373.15$ K (e); LV (empty circle) and LLV (full circle).

For mixtures with a global composition of 80 mol% and higher, the asphaltic phase was observed adhering to the sapphire surface along with the LLE. The LLE interacts with the asphaltenic phase formed when the system stirring is turned on. Moreover, the asphaltenic phase amount qualitatively increases when more gas is added to the mixture, forming a heavy, denser, viscous, bituminous-like phase. In this high gas content condition, two types of immiscibility can be observed, one formed by dispersed

little liquid drops, and another characterized by a heavy bituminous-like, which slips at the sapphire window when the fluid is stirred. For instance, Figure 41a shows the LLE and a heavy bituminous-like phase formed for the BPs-3 + gas-4 mixture with 83.49 mol% gas-4. An additional composition of 84 mol% gas-4 was studied for BPs-2, and the same heavy bituminous-like phase is observed (Figure 41b). In such high gas content conditions, LLA→LLAV transition was measured for the BPs-3 + gas-4 mixture in some temperature conditions, whereas only a critical change from LLA to LAV was observed for the BPs-2 + gas-4 mixture with 84 mol% gas-4. This heavy bituminous-like, viscous, and denser phase shows no preference for the polar surface of the sapphire window; however, it presents a higher density compared to the other fluid phases, allowing it to settle after a stabilization time when the system stirrer is turned off.
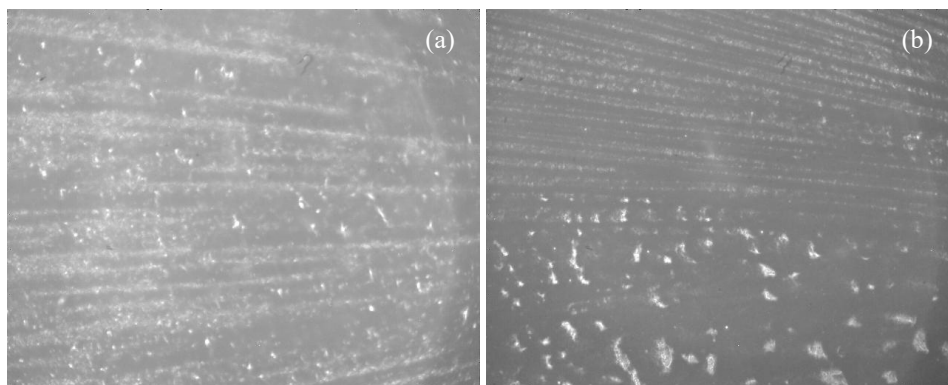
Figure 41. Liquid-liquid-asphaltene equilibrium (LLAE) observed by SWIR inspection. (a) BPs-3 + gas-4 z_{gas-4} = 83.49 mol% at T = 338.15 K and p = 83.00 MPa, and (b) BPs-2 + gas-4 z_{gas-4} = 84.00 mol% at T = 323.15 K and p = 80.00 MPa.

Based on all the mixtures investigated, some points can be highlighted. Firstly, the dispersed LLE was detected only by SWIR light diffraction during fluid inspection, which agrees with the observations made in the last chapters. Secondly, even with a different gas, the LL immiscibility presents the same characteristic, particularly the lower density contrast, requiring a high gas content condition. Finally, the formation of the second liquid phase seems to relate to the heavy fraction of the crude oil sample, demonstrating an interaction with the asphaltenic phase. Moreover, the type of phase behavior observed in the samples studied so far reflects the complexity of reservoir fluid phase behavior studies, and all phase diagrams highlight the importance of a theoretical-experimental study in such a system.

5.2.7   Thermodynamic modeling

Peng-Robinson equation of state (PR EoS) was applied to model all experimental fluid-fluid transitions measured in this chapter. In this context, the binary interaction parameters (k_{ij}) were fitted to the transition pressures, either LV, LL, or LLV. All regressed k_{ij} are given in Table 18. BPs-1 and BPs-2 samples were fitted using systems studied with pure CH_4 and CO_2 and then applied to predict the fluid phase behavior with mixture with gas-3 and gas-4. These parameters were also applied to BPs-3, since this crude oil sample was only investigated with the addition of gas-3 and gas-4. For interaction between carbon dioxide and methane, the coefficient $k_{CO_2-CH_4}$ was fixed to -0.02 for calculations of all phase transitions. Since each crude oil sample has a unique C_{20+} fraction, specific $k_{CO_2-C_{20+}}$, $k_{CH_4-C_{20+}}$, and $k_{HCF-C_{20+}}$ were obtained regarding the BPs-1, BPs-2, and BPs-3.

Table 18. Binary interaction parameter used to predict fluid-fluid phase transition.

i/j	CO_2	C_1	HCF
CO_2	0.000	-0.020	0.150
C_1	-0.020	0.000	0.130
C_3	0.135	0.000	0.000
i-C_4	0.130	0.000	0.000
n-C_4	0.130	0.000	0.000
i-C_5	0.125	0.000	0.000
n-C_5	0.125	0.000	0.000
C_6	0.100	0.000	0.000
C_7	0.100	0.005	0.000
C_8	0.100	0.005	0.000
C_9	0.100	0.017	0.000
C_{10}	0.100	0.019	0.000
C_{11}	0.100	0.021	0.000
C_{12}	0.100	0.023	0.000
C_{13}	0.100	0.025	0.000
C_{14}	0.100	0.027	0.000

C$_{15}$	0.100	0.028	0.000
C$_{16}$	0.100	0.030	0.000
C$_{17}$	0.100	0.032	0.000
C$_{18}$	0.100	0.034	0.000
C$_{19}$	0.100	0.036	0.000
C$_{20+}$: BPs-1	0.100	0.080	0.019
C$_{20+}$: BPs-2	0.100	0.072	0.020
C$_{20+}$: BPs-3	0.080	0.080	0.030
HCF	0.150	0.130	0.000

Initially, some approaches were used to try to model the experimental data measured in this chapter. First, the division into the C$_{20+}$ fraction was not used to generate two distinct compounds, such as a new C$_{20+}$ and HCF. In this approach, only the adjustments of the binary interaction parameters were used. For this first approach, although the model curves fit the phase transition points well, the model does not describe the high-temperature liquid-liquid equilibria and, especially, the liquid-liquid-vapor equilibria observed experimentally. Secondly, the approach using HCF and the new C$_{20+}$ was used so that the critical properties of the new C$_{20+}$ were adjusted along with the binary interaction parameters. In this second approach, the model qualitatively describes the phase transitions observed experimentally well, but the model begins to lose its predictive character, being limited to application to other oil samples, since C$_{20+}$ is a distinct fraction for each oil sample. Therefore, the third and final approach was used to model the systems, where HCF and the new C$_{20+}$ are taken into account and the critical properties of C$_{20+}$ are estimated using correlations well established in the literature.

Some interesting insights can be observed regarding the k_{ij} adjusted. Firstly, higher values were obtained for the CO$_2$ interaction parameter than for CH$_4$. Secondly, higher k_{ij} value between the HCF fraction and CH$_4$ and CO$_2$ can be noted, demonstrating the influence of taking this component into account in describing the experimentally observed phase equilibria. Furthermore, although low values of $k_{HCF-C_{20+}}$ were obtained, it is worth noting that considering the non-ideality between these two heavy phases was crucial for modeling purposes, especially for describing the LLV transition at higher temperatures. Finally, a good description of the experimental and calculated data was

reached. Predicted phase diagrams obtained by PR EoS for mixtures with CO_2 are depicted in Figure 42 and Figure 43, respectively. Furthermore, results for mixtures with CH_4 are given in Figures 44 and 45. Moreover, the predicted phase diagrams for mixtures with gas-3 and gas-4 are shown in Figures 46 and 47, respectively.
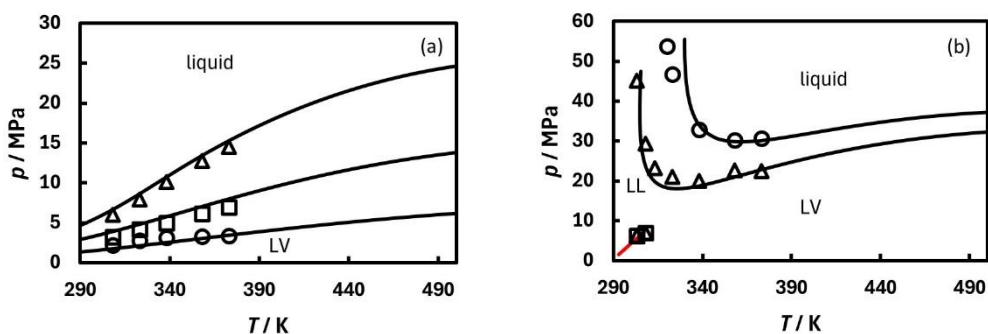
Figure 42. *p-T* diagram for BPs-1 + CO_2 experimental (points) and PR EoS (continuous line);(a) z_{CO_2}= (20.12, 40.11, and 60.01) mol%, and (b) z_{CO_2} = (70.00 and 75.23) mol%. biphasic (black line) and triphasic (red line) regions.
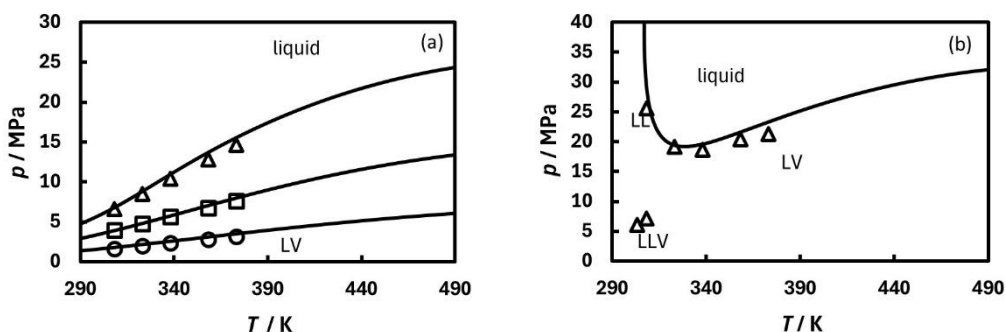
Figure 43. *p-T* diagram for BPs-2 + CO_2 experimental (points) and PR EoS (continuous line);(a) z_{CO_2}= (20.31, 39.86, and 59.96) mol%, and (b) z_{CO_2} = 69.94 mol%. biphasic (black line) and triphasic (red line) regions.
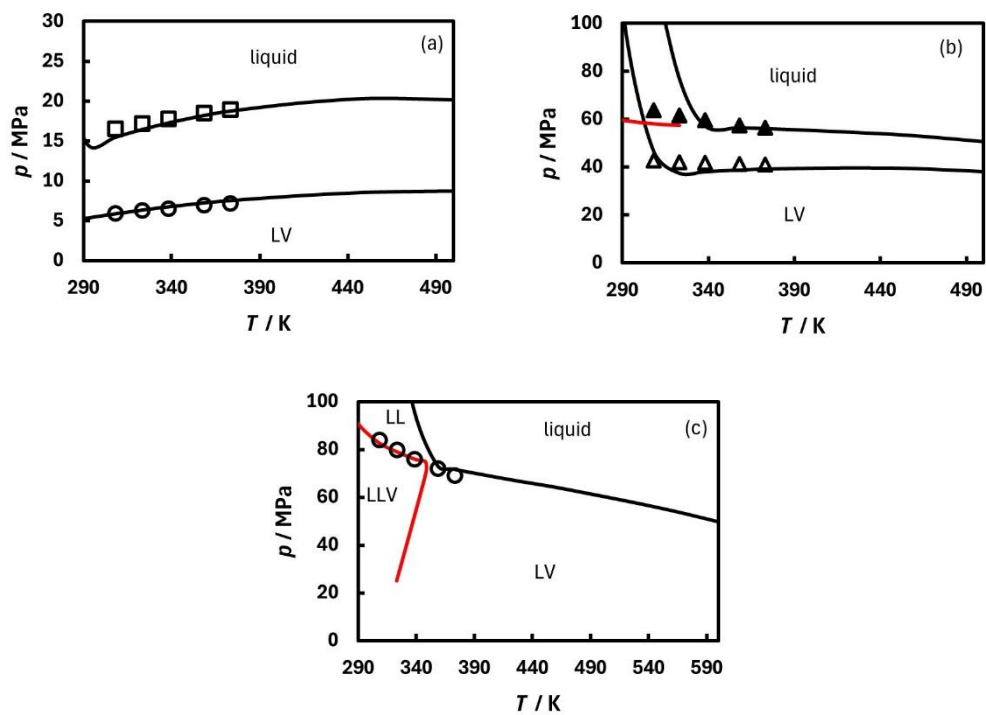
Figure 44. p-T diagram for BPs-1 + CH$_4$ experimental (points) and PR EoS (continuous line);(a) z_{CH_4} = (19.93 and 40.04) mol%; (b) z_{CH_4} = (60.49 and 70.07) mol%; and (c) z_{CH_4} = 75.91 mol%. biphasic (black line) and triphasic (red line) regions.
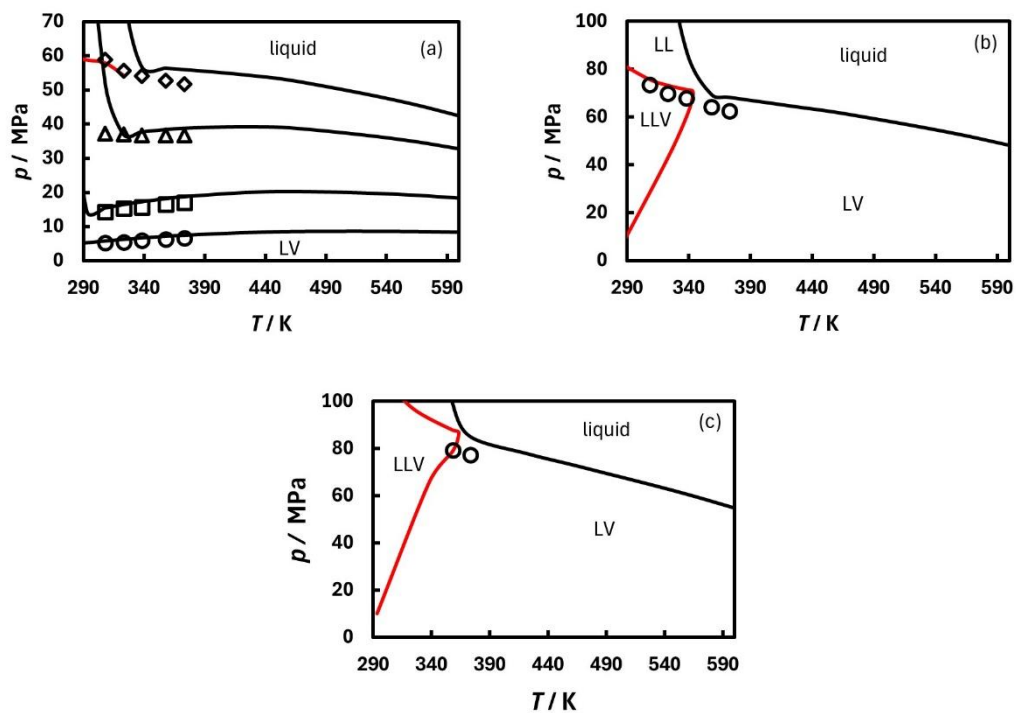
Figure 45. *p-T* diagram for BPs-2 + CH$_4$ experimental (points) and PR EoS (continuous line);(a) z_{CH_4}= (19.87, 39.87, 59.99, and 70.00) mol%; (b) z_{CH_4} = and 75.95 mol%; and (c) z_{CH_4} = 79.99 mol%. biphasic (black line) and triphasic (red line) regions.
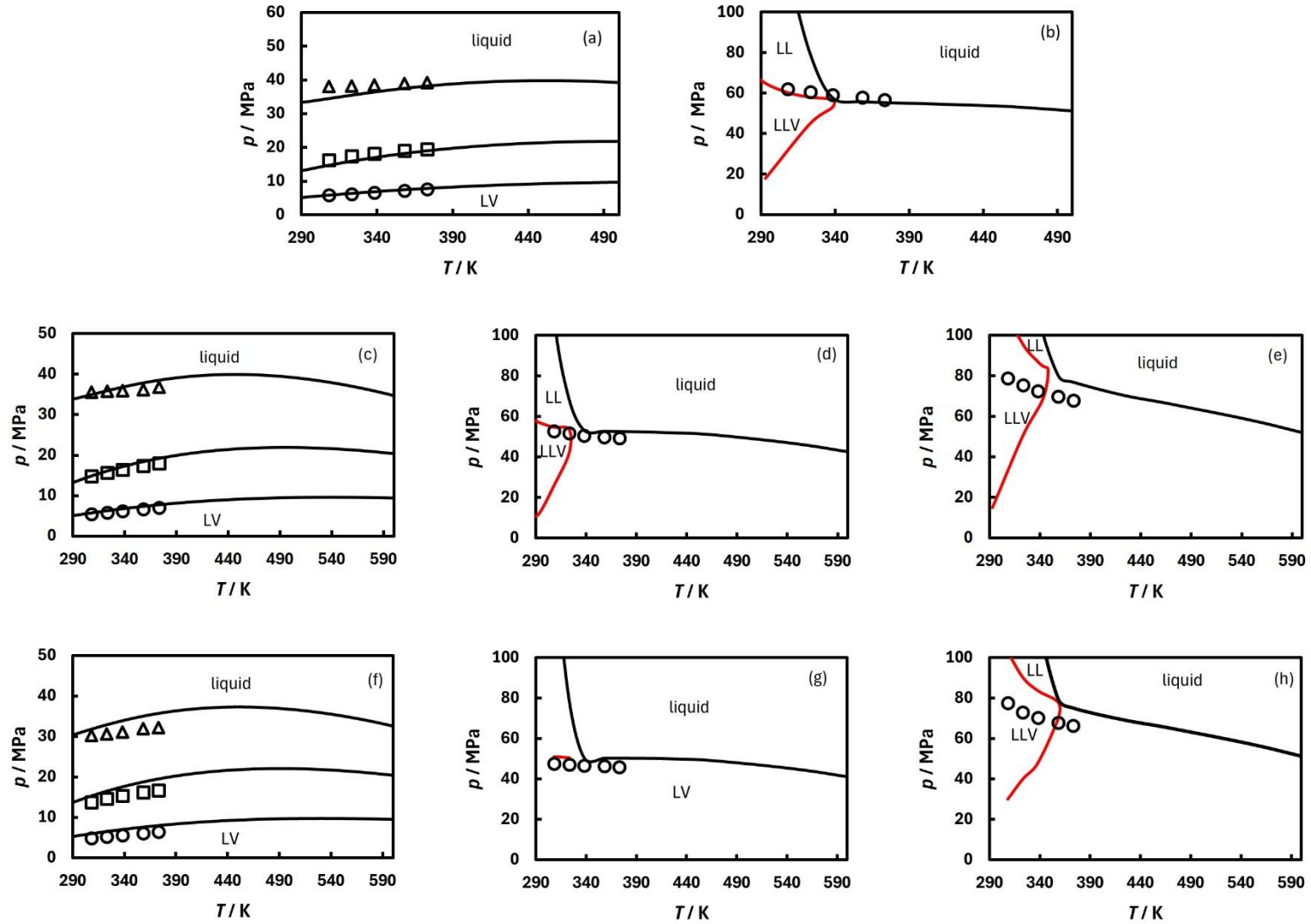
Figure 46. p-T diagram for mixture with gas-3 experimental (points) and PR EoS (continuous line); BPs-1 + gas-3 (a) z_{gas-3}= (23.36, 45.00, and 67.78) mol% and (b) z_{gas-3} = 74.11 mol%; BPs-2 + gas-3 (c) z_{gas-3} = (23.09, 45.08, and 64.80) mol%, (d) z_{gas-3} = 72.82 mol%, and (e) z_{gas-3} = 81.24 mol%; BPs-3 + gas-3 (f) z_{gas-3} = (23.49, 45.03, and 62.23) mol%, (g) z_{gas-3} = 71.32 mol%, and (h) z_{gas-3} = 80.57 mol%. biphasic (black line) and triphasic (red line) regions.
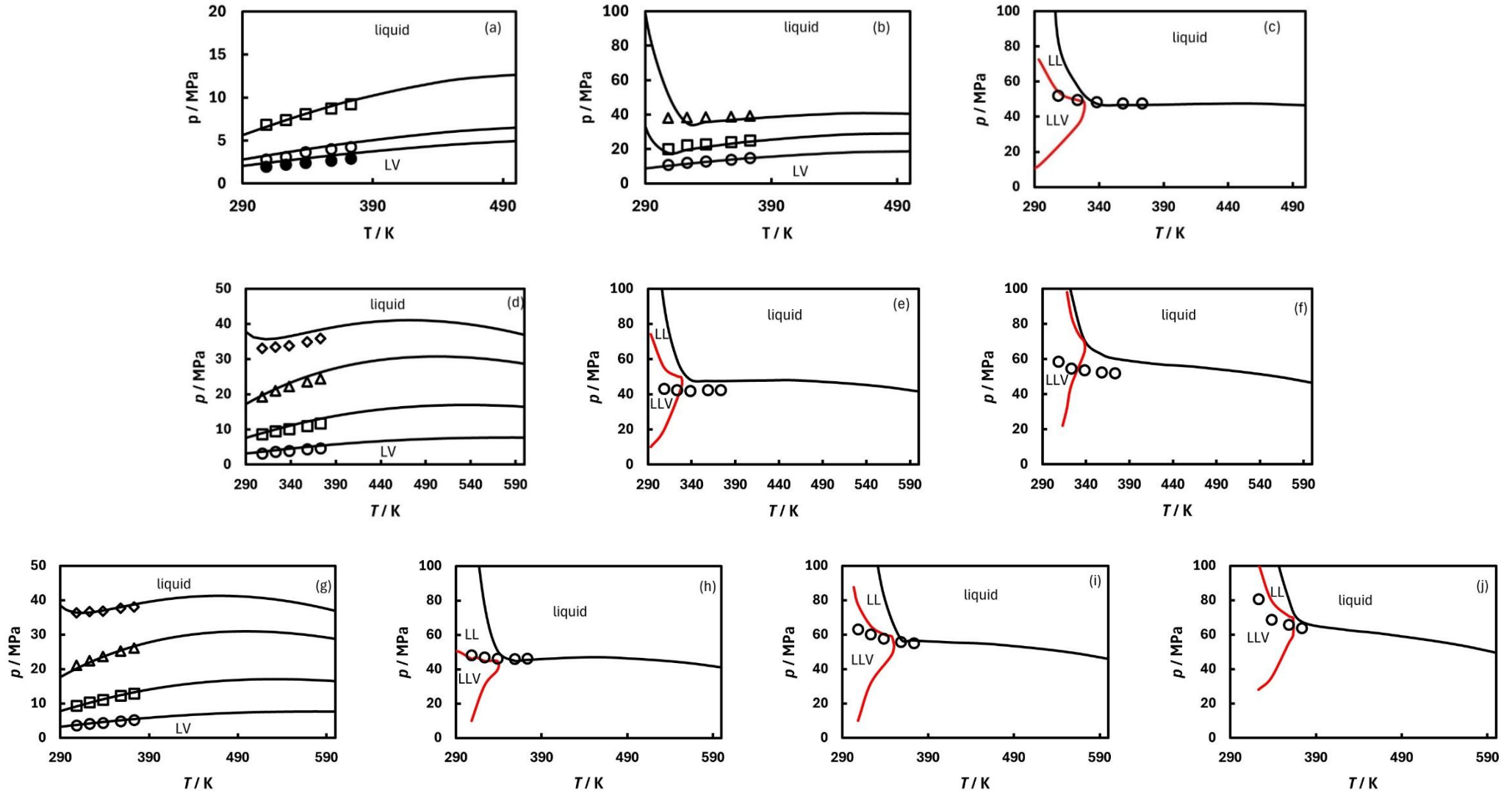
Figure 47. *p-T* diagram for mixture with gas-4 experimental (points) and PR EoS (continuous line); BPs-1 + gas-4. (a) z_{gas-4} = (13.43, 17.62, and 31.99) mol%, (b) z_{gas-4} = (43.42, 58.08, and 69.79) mol%, and (c) z_{gas-4} = 74.75 mol%; BPs-2 + gas-4 (d) z_{gas-4} = (19.96, 39.91, and 59.95) mol%, (e) z_{gas-4} = 74.95 mol% , and (f) z_{gas-4} = 79.76 mol%; BPs-3 + gas-4 (g) z_{gas-4} = (20.07, 40.00, 59.99, and 69.97) mol% , (h) z_{gas-4} = 74.99 mol%, (i) z_{gas-4} = 79.99 mol%, and (j) z_{gas-4} = 83.49 mol%. biphasic (black line) and triphasic (red line) regions.

Considering the high asymmetry and the complex phase behavior observed for the investigated mixtures, it can be pointed out that the modeling approach qualitatively describes all systems, especially the LL to LLV transition at high temperatures. Important insights can be obtained through thermodynamic modeling. Similar characteristics to those observed in the experimental results are present for the second liquid phase at high pressure and high temperature modelled by the PR EoS. This second liquid phase formation results from the asymmetry between the heavy hydrocarbon fraction (HCF) and gas molecules. The most revealing result was obtained by performing a multi-phase flash calculation, determining the LL loci for systems at the same temperature and a similar global composition as a reference. The flash calculation reveals that the LLE modelled for each crude oil presents one liquid phase close to the global composition and another mainly composed of the HCF fraction (near $x_{HCP} \approx 60$ mol%). This result suggests that the second liquid phase is formed by the demixing of the heavy fraction from the main liquid phase caused by excess gas addition in the system.

Furthermore, when the same analysis is performed for the highest global compositions studied, the molar composition of the HCF in the second phase smoothly decreases, which can be explained by the occurrence of a heavy bituminous-like phase. This suggests that the bituminous-like phase is formed practically by the HCF fraction. Figure 48 shows the second liquid phase profile composition obtained by the flash calculation for BPs-2 with gas-3 and gas-4 at $p = 55.0$ MPa and $T = 323.15$ K.
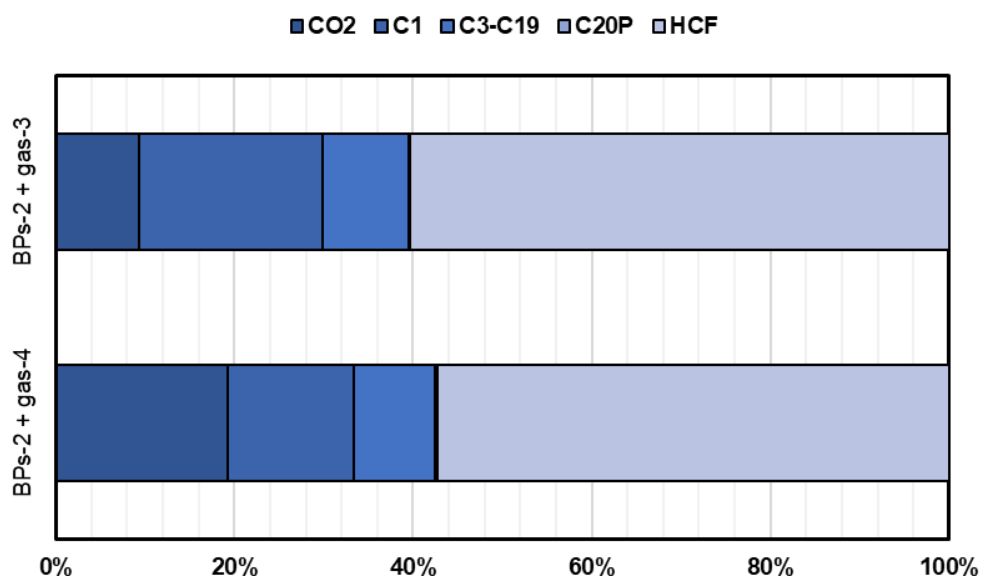
Figure 48. Composition profile of the second liquid phase at $p = 55.0$ MPa and $T = 323.15$ K for BPs-2 + gas-3 and BPs-2 + gas-4 with 74.95 mol% gas and 72.83 mol% gas, respectively.

5.3   Conclusion

This chapter assesses the fluid phase behavior of three pre-salt crude oil samples using a full-visibility SWIR inspection method. Several isopleths were investigated, and different phase transitions, such as LV, LL, and LLV, were experimentally measured. Interesting results were observed regarding the LLE and LLVE under high-pressure and high-temperature conditions. Given the higher complexity observed regarding LLE, the approach used to model all fluid-fluid transitions provided a good description with experimental data. Moreover, thanks to thermodynamic modeling, essential information was obtained regarding the molar composition of the phases. This information is crucial, as it cannot be obtained experimentally using a synthetic method that does not permit the sampling and analysis of the phases present at equilibrium. By associating experimental observations and thermodynamic modeling, it was possible to relate the occurrence of the dispersed liquid-liquid equilibrium observed in all the mixtures to the heavy fraction of crude oil and its asymmetry with the gases added to the system. Furthermore, the results obtained using a full-view PVT cell reinforce the experimental observations of chapters II and III by overlapping the considerations and limiting fluid inspection of the high-pressure microscope to indicate a multiphasic equilibrium condition.

6 CHAPTER V: FLUID PHASE BEHAVIOR OF ASYMMETRIC SYNTHETIC MIXTURE + GAS: EXPERIMENTAL AND MODELING STUDIES

Results published in: Fluid phase behavior of asymmetric synthetic mixture + gas: Experimental and modeling studies, The Journal of Supercritical Fluids, https://doi.org/10.1016/j.supflu.2025.106519

6.1 Introduction

Experimental data for fluid phase equilibria of multicomponent systems are scarce in the literature but are fundamental to reservoir engineering. Typically, to assess the phase behavior of reservoir fluid systems, a thermodynamic model should be employed to predict equilibrium properties and evaluate the gas's influence in the mixture. Generally, the parameters of these models are predicted using correlations and tuned using a limited set of experimental data. However, such required experimental data are scarce (Jaubert et al., 2020; Kontogeorgis et al., 2021).

Given the inherent complexity of petroleum fluids regarding their compositions, it is advantageous to investigate the fluid phase behavior of synthetic mixtures (Shariati; Peters; Moshfeghian, 1998a, 1998b) for developing or testing thermodynamic models. The approach involving study synthetic mixtures solves the problem of unknown composition regarding reservoir fluids. However, despite the availability of data on binary hydrocarbon + gas mixtures (Dohrn et al., 2024; Fonseca; Dohrn; Peper, 2011; Peper; Fonseca; Dohrn, 2019) there remains a shortage of phase equilibrium data for asymmetric mixtures containing very low-volatility molecules and heavy hydrocarbons, particularly polyaromatic, alkyl-naphthene, and branched-chain alkanes (Al Ghafri; Maitland; Trusler, 2014; Dohrn et al., 2024; Fonseca; Dohrn; Peper, 2011). Including such components may result in multiphase equilibria, such as solid-liquid-vapor, solid-liquid-liquid, and liquid-liquid-vapor equilibria, when mixed with a high gas content over a wide range of temperatures and pressures.

The last chapters focused on the investigation of fluid phase behavior in Brazilian pre-salt crude oil samples, highlighting the complexity of such systems. Precisely, the occurrence of a liquid-liquid and liquid-liquid-vapor equilibria under unconventional high-

pressure and high temperature conditions were experimentally measured using a combination of analytical techniques. Proper observation of these phase transitions was possible only due to SWIR inspection, especially when coupled with a full-view PVT measurement cell. By coupling the experimental observations with thermodynamic modeling results, the liquid-liquid immiscibility was attributed to the heavy hydrocarbon fraction. For modeling purposes, these fractions are represented by considering a pseudo-component reported by Yanes et al. (2020), which has specific properties such as low critical pressure and a high acentric factor. By using a pseudo component to represent this polyaromatic fraction, it was possible to model a second liquid phase with properties that agree with those observed experimentally.

In order to reproduce the complex phase behavior experimentally observed in the previous chapters, especially the LLE at high temperatures, this chapter aims to investigate the fluid phase equilibria of asymmetric synthetic mixtures consisting of a ternary liquid hydrocarbon blend with a gas mixture. This blend includes a branched-chain compound (2,2,4,4,6,8,8-heptamethylnonane), a naphthenic compound (dodecylcyclohexane), and a polyaromatic compound (*o*-terphenyl). The gas mixture, composed of methane, ethane, and propane, was introduced to mimic the light ends of live oil. Additionally, the effect of adding carbon dioxide to the gas mixture was examined. The motivation for this chapter stemmed from the need for a model capable of reproducing the complex phase behavior related to Brazilian Pre-Salt reservoir fluids, as discussed in previous chapters. The choice of such compounds is related to the solid-liquid line at high temperature and the high acentric factor of some compounds (Romero Yanes et al., 2020a, 2021b). Liquid hydrocarbon mixture was used to mimic the heavy fraction of crude oil.

In addition, and to meet the need for accurate modeling of Brazilian pre-salt fluids, the experimental data obtained from these model systems were compared to calculations performed using the predictive PPR78 model (Peng; Robinson, 1976). This model is based on the Peng-Robinson equation of state and includes a fully predictive mixing rule, enabling predictions of fluid phase equilibria for asymmetric mixtures containing both light and heavy components. It combines simplicity and versatility and has proven particularly suitable for predicting the phase behavior of the binary mixtures used as model systems in previous studies (Jaubert; Mutelet, 2004; Jaubert; Privat; Mutelet, 2010; Vitu et al., 2007). The aim here is to verify that its use can be extended to asymmetric multi component systems that could serve as model systems for pre-salt reservoir fluids from Brazilian fields, such as those in the Santos Basin.

6.2   Materials and methods

6.2.1   Materials and mixture preparation
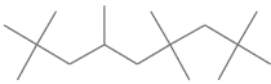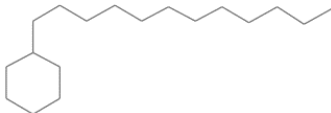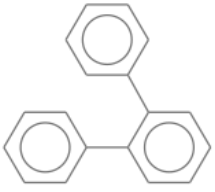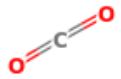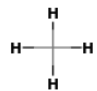
The purity and supplier of all components used in this study to formulate the studied mixtures are listed in Table 19. This includes both the pure liquid components, and the hydrocarbon gas mixture (HGM) formed by three lower molecular weight hydrocarbons, such as methane, ethane, and propane and which was prepared on request by the supplier. It is worth noting that all chemical compounds are used without further purification. The physical properties, such as molecular weight, melting temperature, and normal boiling point are given in Table 20. This chapter studied two different systems, which differed in the gas composition added to the synthetic ternary liquid mixture (TLM). The first system named PsB1 (PreSalt Blend 1) is formed by blending the hydrocarbon gas mixture and the ternary liquid mixture (HGM + TLM). The second system (PsB2) involves adding carbon dioxide to the first system, resulting in a gas blend with a 1:1 molar ratio between HGM and CO_2 in all the mixtures investigated so as it also corresponds to a pseudo gas-liquid binary system: HGM-CO_2 + TLM. Phase behavior measurements of the multicomponent system were conducted using the synthetic method, treating the systems as a pseudo binary gas-liquid mixture. Therefore, great care was taken during the synthesis of the mixtures to ensure the correct composition of the investigated isopleths. For this purpose, the liquid components were first blended in a large vessel to prepare the liquid mixture needed for all the investigated gas-liquid mixtures, ensuring the same liquid composition in all these mixtures. Such liquid mixture was prepared gravimetrically at atmospheric pressure and ambient temperature using an analytical balance with a precision of 0.0001 g. Afterward, the mixture was heated to $T = 323.15$ K and mixed to melt solid components and achieve a homogeneous liquid state in the reservoir tank. The composition of the obtained blend is provided in Table 21. This composition was based on the solubility of the polyaromatic compound in other hydrocarbons, since it has a high melting temperature at atmospheric pressure. Following its preparation, a sample of this liquid mixture was introduced into the PVT cell under vacuum. An analytical balance with a precision of 1 milligram (mg) was used to determine the exact amount of liquid transferred during this operation. Next, the gas was added by volumetric displacement under high pressure, performed using two Teledyne Isco 100D syringe pumps with a precision of 0.01 cm³. One pump was used for the hydrocarbon gas mixture, and the other for pure CO_2. In both pumps, pressure and temperature were monitored to maintain a constant density during gas injection. The density
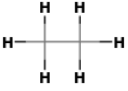
values needed to convert volume displacement into injected masses were taken from NIST REFPROP software (Linstrom; Mallard, 2001). According to these procedures, five global mole compositions were studied for PsB1, as follows: z_{HGM}= (19.98, 40.00, 59.81, 74.93) mol%; and seven global mole compositions were evaluated for the PsB2, as follows: $z_{HGM-CO2}$ = (20.09, 40.14, 60.00, 70.00, 74.97, 79.98) mol%. The combined uncertainty for the gas mole fraction (either HGM or HGM-CO$_2$) in the mixture preparation procedure was calculated using the following relation:

$$u_c(z_{HGM}) = z_{HGM}(1 - z_{HGM})\left(\frac{u^2(m_{HGM})}{m_{HGM}^2} + \frac{u^2(m_{TLM})}{m_{TLM}^2}\right)^{0.5} \tag{5.1}$$

where u_c denotes combined uncertainty if the global mole composition; $u(m_{HGM})$ and $u(m_{TLM})$ refer to the combined uncertainty associated with the mass of the hydrocarbon gas mixture (HGM or HGM-CO$_2$) and the ternary liquid mixture (TLM), respectively.

Table 19. CAS number, molecular structure, mass purity, and supplier of chemical compounds.

component	CAS number	molecular structure	mass purity, %	supplier
2,2,4,4,6,8,8 heptamethylnonane	4390-04-9		98.2	Sigma-Aldrich
Dodecylcyclohexane	1795-17-1		99.1	Tokyo Chemical Industry
o-terphenyl	84-15-1		99.9	Sigma-Aldrich
carbon dioxide	124-38-9		99.99	Linde
hydrocarbon gas mixture (HGM)				
methane	74-82-8		70.04	

| ethane | 74-84-0 | | 17.02 |
| propane | 74-98-6 | | 12.94 |

Table 20. Chemical molecular weight, normal boiling point (T_b), and melting temperature (T_m)[a].

component	molecular weight / g·mol^{-1}	T_b / K	T_m / K
2,2,4,4,6,8,8 heptamethylnonane	226.44	513.0	203.15
dodecylcyclohexane	252.48	588.0	282.3
o-terphenyl	230.30	610.2	331.0
carbon dioxide	44.01	-	-
hydrocarbon gas mixture			
methane	16.04	111.0	85.7
ethane	30.07	184.6	101
propane	44.10	231.1	85.5

[a]data recorded from NIST webbook.

Table 21. Mole composition of the three-component synthetic mixture used in this chapter.

compound	mole composition
2,2,4,4,6,8,8 heptamethylnonane	0.3998
dodecylcyclohexane	0.2010
o-terphenyl	0.3992

6.2.2 Experimental technique

The same experimental apparatus used in Chapter IV was applied in this chapter. Fluid-fluid and solid-fluid transitions were measured using a synthetic method (Dohrn et al., 2024; Fonseca; Dohrn; Peper, 2011; Peper; Fonseca; Dohrn, 2019). Although the system under study is transparent, a camera operating in the SWIR domain was applied (Figure 49). This SWIR camera was preferred over a camera which operates in the visual domain to detect the occurrence of possible liquid-liquid transitions leading to the formation of dispersions that are difficult to detect in visible light.
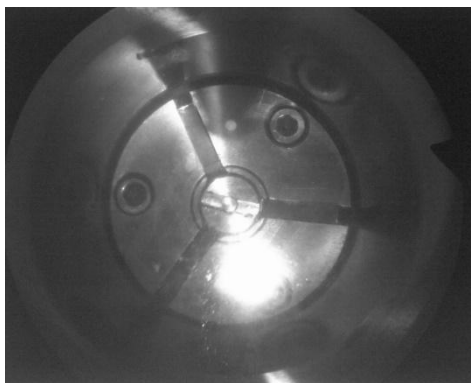
Figure 49. Snapshot of the front view of the high-pressure cell using the SWIR device.

Both systems studied in this chapter were investigated in a temperature range $T =$ (293.15 – 373.15) K. Once the desired temperature is reached, the pressure was slowly increased under constant stirring, until a homogeneous state is reached. After equilibration time, a controlled depletion was performed in a constant ramp equal to $p = 0.3$ MPa/min. The vapor occurrence was determined either visually or by determining a break the Y-factor versus pressure curve obtained during the constant mass expansion of the fluid. This procedure allowed to perform all fluid-fluid phase transition measurements. However, because of the steep slope regarding the melting line in the *pressure-Temperature* diagram, the solid-fluid transition is determined by the disappearance temperature in an isobar process (Pauly; Coutinho; Daridon, 2007). Solid-fluid boundaries were evaluated determining the solid phase disappearance temperature condition instead of its appearance because of the supersaturation processes. For that, the experiment starts from a solid-fluid region. It is stepwise heated at a fixed pressure using a maximum temperature change equal to 0.2 K/min between two steps. After the last crystal of solid had dissolved, the system pressure was increased to induce the formation of new solid crystals resulting from the interception of the melting line due to the positive slope of the melting line in the p,T diagram. This procedure was repeated until reaching elevated pressures. It allows the system to remain in equilibrium throughout the experiment and is particularly effective for compounds exhibiting high subcooling effects (Daridon et al., 2021; Pauly; Coutinho; Daridon, 2007; Yanes; Montel; Daridon, 2022a).

6.2.3 Thermodynamic modeling

All fluid-fluid and solid-fluid phase transition experimentally measured were modeled using the Peng-Robinson equation of state, as described in Chapter IV. Phase diagrams were modeled by the intermediate of a multiphase flash calculation based on the Michelsen tangent plane distance function (Michelsen, 1982a, 1982b). In this chapter a predictive approach was tested to modeling the phase behavior observed for both PsB-1 and PsB-2. This approach, known as PPR78, involves predicting the binary interaction parameters k_{ij} between the molecules "i" and "j, using a group contribution method. The PPR78 method was first proposed by Jaubert *et al.* and has since been extended to include various groups by different authors (Jaubert et al., 2013, 2005; Jaubert; Mutelet, 2004; Jaubert; Privat, 2010; Jaubert; Privat; Mutelet, 2010; Vitu et al., 2007; Vitu; Jaubert; Mutelet, 2006). It was used here to determine the k_{ij} for all possible pairs of components formed from the six or seven components in the mixtures, as it has proven to be well suited for representing the phase behavior of binary systems involving such components (Jaubert et al., 2005; Jaubert; Mutelet, 2004; Jaubert; Privat; Mutelet, 2010; Vitu et al., 2008a, 2008b, 2021; Vitu; Jaubert; Mutelet, 2006; Yanes; Montel; Daridon, 2022a, 2022b; Zid et al., 2022a, 2022b). Through this methodology, the k_{ij} is expressed as a function of temperature by the following relation:

$$k_{ij}(T) = \left\{ \left[-\frac{1}{2} \sum_{k=1}^{Ng} \sum_{l=1}^{Ng} (\alpha_{ik} - \alpha_{jk})(\alpha_{il} - \alpha_{jl}) A_{kl} \cdot \left(\frac{298.15}{T} \right)^{\left(\frac{B_{kl}}{A_{kl}} - 1 \right)} \right] - \left(\frac{\sqrt{a_i(T)}}{b_i} - \right. \right.$$

$$\left. \left. \frac{\sqrt{a_j(T)}}{b_j} \right)^2 \right\} \cdot \left(2 \frac{\sqrt{(a_i(T) \cdot a_j(T))}}{b_i b_j} \right)^{-1} \tag{5.1}$$

where, N_g is the total number of functional groups that compose the molecule, α_{ik} is the fraction of the group k present in the molecule i. $A_{kl} = A_{lk}$ and $B_{kl} = B_{lk}$ are constant. Currently, 21 functional groups are available for PPR78, and the A_{kl} and B_{kl} were obtained by fitting experimental binary vapor-liquid equilibrium data using the PR-EOS with a Soave (α) function (Soave, 1972). To obtain the parameters involved in the equation of state, the knowledge of critical temperature of components (Tc_i, Tc_j), critical pressure (Pc_i, Pc_j), and acentric factor (ω_i, ω_j) are needed. Table 22 provides the critical properties values used for all components studied in this chapter. For the heavy component these values were obtained from *NIST* database for the 2,2,4,4,6,8,8 heptamethylnonane and *o*-terphenyl. However, the critical properties of the

dodecylcyclohexane were estimated by using the Joback group contribution method (Joback; Reid, 1987) as no value was available in the *NIST* database (Linstrom; Mallard, 2001)or literature. The acentric factor (ω) of liquid hydrocarbons were calculated by using the Pitzer relation (Lee; Kesler, 1975), as follows:

$$\omega = \frac{-\ln(pc)-5.92714+6.09648\cdot\theta^{-1}+1.28862\cdot\ln(\theta)-0.169347\cdot\theta^6}{15.2518-15.6875\cdot\theta^{-1}-13.4721\cdot\ln(\theta)+0.43577\cdot\theta^6} \tag{5.2}$$

Table 22. Critical temperature (T_c), critical pressure (P_c), and acentric factor (ω) of pure components used in this study.

component	T_c / K	P_c / MPa	ω
methane	190.6	4.60	0.0115
ethane	305.4	4.88	0.0908
propane	369.8	4.25	0.1454
carbon dioxide	304.2	7.38	0.2250
2,2,4,4,6,8,8 heptamethylnonane	692.0[a]	1.57[a]	0.4825[c]
dodecylcyclohexane	756.3[b]	1.33[b]	0.7203[c]
o-terphenyl	857.0[a]	3.00[a]	0.5707[c]

*Obtained from NIST chemistry webbook; [b]obtained from Joback group contribution method using T_b present in Table 20; [c]calculated from Pitzer relation using T_b present in Table 20.

The *o*-terphenyl (ot) has a high melting temperature, and it can therefore crystallize in the synthetic systems in the temperature range of investigation. Because it does not belong to the same chemical family as the other heavy components and their chemical structures are very different, it is expected to form a pure solid (S) phase. In this case, the condition of solid-fluid equilibrium can be described in terms of fugacity as:

$$f_{ot}^{*,S}(T,p) = f_{ot}^{f}(T,p,x_{ot}^{f}) \tag{5.3}$$

where the fugacity of pure (*) *o*-terphenyl in the solid phase $f_{ot}^{*,S}$ can be related to its fugacity in the subcooled liquid state $f_{ot}^{*,L}$ from the Gibbs energy change Δg_{ot}^{SL} between the pure solid and subcooled liquid at the equilibrium temperature (Prausnitz; Lichtenhaler; De Azevedo, 1999). The thermal properties of *o*-terphenyl being well known at atmospheric pressure (Chang;

Bestul, 1972), Δg_{ot}^{SL} can be estimated without making any simplifying assumptions. Consequently, $f_{ot}^{*,S}$ can be readily obtained using the following relation:

$$\ln\left(\frac{f_{ot}^{*,S}(T,p_0)}{f_{ot}^{*,L}(T,p_0)}\right) = -\frac{\Delta g_{ot}^{SL}}{RT} = -\frac{\Delta h^m}{RTT^m}\Delta T + \frac{a_0^L - a_0^S}{RT}\left[\Delta T - T\ln\left(\frac{T^m}{T}\right)\right] + \frac{a_1^L - a_1^S}{2RT}(\Delta T)^2 \qquad (5.4)$$

where Δh^m and T^m are the enthalpy and temperature of melting, ΔT is the difference in temperature: $T^m - T$, and a_0^L, a_0^S and a_1^L, a_1^S are the parameters of the linear dependences for liquid and solid heat capacities versus temperature between T^m and T according to the following relation

$$c_P = a_0 + a_1 T \qquad (5.5)$$

The parameters a_0 and a_1 for both liquid and solid o-terphenyl were determined by fitting the heat capacity data reported by Chang and Bestul (1972). The obtained values are presented in Table 23, along with the Δh^m and T^m values used in eq. 5.4.

The influence of pressure on the solid fugacity of the o-terphenyl was obtained from those at atmospheric pressure by considering the Poynting correction:

$$\ln\left(\frac{f_{ot}^{*,S}(T,p)}{f_{ot}^{*,S}(T,p_0)}\right) = \int_{p_0}^{p} v^{*,S}\, dp \qquad (5.6)$$

in which the molar volume of the solid was expressed as a function of that in the liquid to avoid the integration in the Poynting correction as proposed by Pauly et al. (2000):

$$v^{*,S} = \beta v^{*,L} \qquad (5.7)$$

where $v^{*,L}$ denote the liquid molar volume, and β parameter was estimated to be equal to 0.91 from available literature data (Chang; Bestul, 1972; Naoki; Koeda, 1989). Using this approach, one can obtain the following relation that allows determining the effect of pressure on solid fugacity:

$$\ln \left(\frac{f_{ot}^{*,S}(T,p)}{f_{ot}^{*,S}(T,p_0)} \right) = \beta \int_{p_0}^{p} v^{*,L} \, dp = \beta \ln \left(\frac{f_{ot}^{*,L}(T,p)}{f_{ot}^{*,L}(T,p_0)} \right) \tag{5.8}$$

Finally, by replacing $f_{ot}^{*,S}(T, p_0)$ with its expression given by eq. 5.4 , the fugacity of o-terphenyl in the pure solid phase at a given temperature and pressure takes the following form, which enables the prediction of fluid-solid phase transitions using the Peng-Robinson equation of state with the classical quadratic and mixing rules for a and b parameters and by using PPR78 for predicting BIPs:

$$\ln\left(f_{ot}^{*,S}(p)\right) = \beta \ln\left(f_{ot}^{*,L}(p)\right) + (1 - \beta) \ln\left(f_{ot}^{*,L}(p_0)\right) - \frac{\Delta h^m \Delta T}{RTT^m} + (a_0^L - a_0^S) \frac{\Delta T - T \ln\left(\frac{T^m}{T}\right)}{RT} + \frac{a_1^L - a_1^S}{2RT}(\Delta T)^2 \tag{5.9}$$

Table 23. Solid-liquid phase change properties* of o-Terphenyl obtained from literature data (Chang; Bestul, 1972; Naoki; Koeda, 1989)

T^m / K	Δh^m / J.mol^{-1}	a_0^L / J.K^{-1}.mol^{-1}	a_1^L / J.K^{-2}.mol^{-1}	a_0^S / J.K^{-1}.mol^{-1}	a_1^S / J.K^{-2}.mol^{-1}	β
329.4	17200	177.4	0.644	-9.914	0.955	0.91

* a_0, a_1 are defined in eq. 5.5 and β in eq. 5.7.

6.3   Results

6.3.1   Phase boundary measurements

Sixty-nine (69) experimental points were measured for PsB1 (HGM + TLM), and all the obtained data were reported in Tables 24 and 25. Table 24 provides the fluid-fluid phase transitions experimentally observed and measured at a fixed temperature, whereas Table 25 gives the phase transitions involving a solid phase determined at a fixed pressure. Moreover, the solid-fluid boundaries for the ternary liquid mixture (TLM) without gas addition were included in Table 25.

Table 24. Pressure p and temperature T conditions of the fluid-fluid transition measured at a given temperature T at five different global compositions $z_{HGM} \pm U(z_{HGM})$ in mol% for PsB1 (HGM + TLM).

T / K	p / MPa	transition	T / K	p / MPa	transition
z_{HGM} = 19.98 ± 0.16 mol%			z_{HGM} = 40.00 ± 0.18 mol%		
314.65	3.97	L → LV	317.72	10.27	L → LV
317.36	4.03	L → LV	323.05	10.63	L → LV
323.22	4.20	L → LV	338.15	11.22	L → LV
337.85	4.49	L → LV	358.15	11.96	L → LV
357.62	4.77	L → LV	373.15	12.42	L → LV
373.15	5.02	L → LV			
z_{HGM} = 59.81 ± 0.26 mol%			z_{HGM} = 74.93 ± 0.21 mol%		
313.83	20.92	L → LV	313.08	34.15	L → LV
323.87	21.66	L → LV	323.34	34.80	L → LV
338.96	22.13	L → LV	337.99	34.86	L → LV
359.16	23.01	L → LV	357.79	35.15	L → LV
374.19	23.56	L → LV	372.92	35.37	L → LV
z_{HGM} = 80.00 ± 0.21 mol%					
313.04	39.89	L → LV			
323.02	39.58	L → LV			
338.65	39.43	L → LV			
357.87	39.37	L → LV			
373.01	39.41	L → LV			

[*]Standard uncertainty for u(T) = 0.1 K and u(p) = 0.02 MPa. Expanded uncertainty U(k = 2, confidence level = 0.95) for L→LV is $U(p)$ = 0.06 MPa.

Table 25. Pressure p and temperature T conditions of the solid-fluid transition measured at five different global compositions $z_{HGM} \pm U(z_{HGM})$ in mol% for PsB1 (HGM + TLM).

T / K	p / MPa	transition	T / K	p / MPa	transition	T / K	p / MPa	transition
$z_{HGM} = 0.00$ mol %			$z_{HGM} = 19.98 \pm 0.16$ mol%			$z_{HGM} = 40.00 \pm 0.18$ mol%		
318.00	0.10	SL → L	314.65	5.58	SL → L	311.43	6.58	SLV → LV
320.70	9.95	SL → L	317.92	16.59	SL → L	311.09	8.58	SLV → LV
323.00	19.20	SL → L	321.24	29.61	SL → L	313.16	19.59	SL → L
325.50	27.70	SL → L	323.77	39.62	SL → L	315.44	29.60	SL → L
327.10	33.20	SL → L	329.12	59.64	SL → L	317.62	39.61	SL → L
329.00	40.00	SL → L				320.10	49.63	SL → L
330.20	44.20	SL → L				322.18	59.56	SL → L
333.60	55.60	SL → L						
337.80	70.00	SL → L						
$z_{HGM} = 59.81 \pm 0.26$ mol%			$z_{HGM} = 74.93 \pm 0.21$ mol%			$z_{HGM} = 80.00 \pm 0.21$ mol%		
308.51	20.20	SL → SLV	293.15	28.77	SL → SLV	312.37	40.02	SL → L
303.35	19.88	SL → SLV	297.74	29.80	SL → SLV	313.46	59.94	SL → L
298.69	19.75	SL → SLV	303.17	31.01	SL → SLV	314.35	70.04	SL → L
309.50	20.99	SL → L	308.16	32.78	SL → SLV	298.46	32.87	SL → SLV
310.49	25.05	SL → L	310.25	33.85	SL → SLV	303.22	34.12	SL → SLV
313.16	40.08	SL → L	309.60	29.00	SLV → LV	307.86	36.12	SL → SLV
314.95	50.12	SL → L	308.08	19.59	SLV → LV	311.31	38.54	SL → SLV
316.73	59.64	SL → L	306.58	9.58	SLV → LV	311.18	38.01	SLV → LV
308.41	17.99	SLV→ LV	311.08	35.01	SL → L	308.80	30.02	SLV → LV
308.80	11.97	SLV→ LV	312.26	45.01	SL → L			
			313.26	55.03	SL → L			
			314.25	65.04	SL → L			

*Expanded uncertainty U(k = 2, level of confidence = 0.95) for solid disappearance temperature is $U(T) = 0.45$ K.

Figure 50 presents the solid-liquid boundary for various isopleths. For mixtures with a global composition of up to 59.80 mol%, the melting lines nearly show a linear shape in the p,T diagram. The curves shift to lower temperatures with gas addition while remaining parallel to the SL transition curve of the ternary liquid system. This observation shows that the SL curves are mainly translated due to the dissolution effect caused by adding new components that decrease the mole fraction of o-terphenyl in the liquid phase x_{ot}^L. For systems with 74.93 mol% HGM and beyond, the shape of the melting line smoothly changes at pressures above the bubble point. This highlights the influence of the change in compressibility at liquid-solid transition conditions in these systems with a high gas content, making them highly compressible.
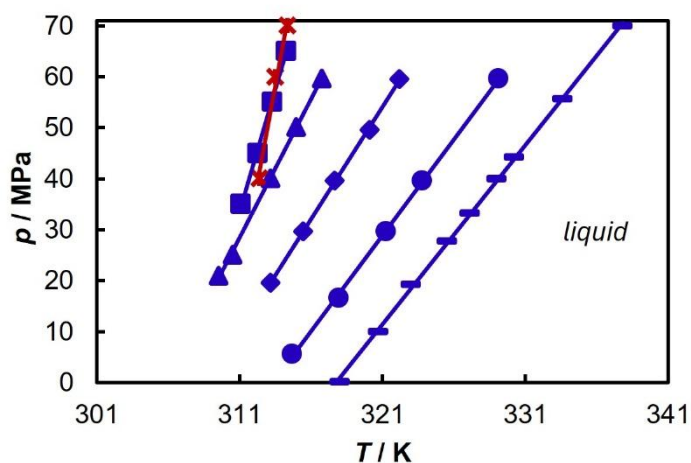
Figure 50. Solid-fluid phase transition (SL → L) measured at different HGM global mole compositions. blue line (—), z_{HGM} = 0 mol%; blue circle (●), z_{HGM} = 19.98 mol%; blue diamond (♦), z_{HGM} = 40.00 mol%; blue triangle (▲), z_{HGM} = 59.81 mol%; blue square (■), z_{HGM} = 74.93 mol%; and, red (x), z_{HGM} = 80.00 mol%.

Isopleth phase diagrams comprising the raw experimental data in Tables 24 and 25 were constructed and presented in Figure 51. Even by the occurrence of a solid phase, the PsB1 mixture behaves as a classic system presenting only a liquid (L) to liquid-vapor (LV) transition in all global compositions investigated, without the observation of a liquid-liquid equilibrium (LLE) in the conditions studied. For all mixtures, the occurrence of a vapor phase was easily detected by direct observation or by a regime change in the *Y-factor* curve about pressure. This result shows that the *Y-factor* curve is a good technique for measuring bubble point pressures when a precise visual method is available or when the fluid analyzed is darker.
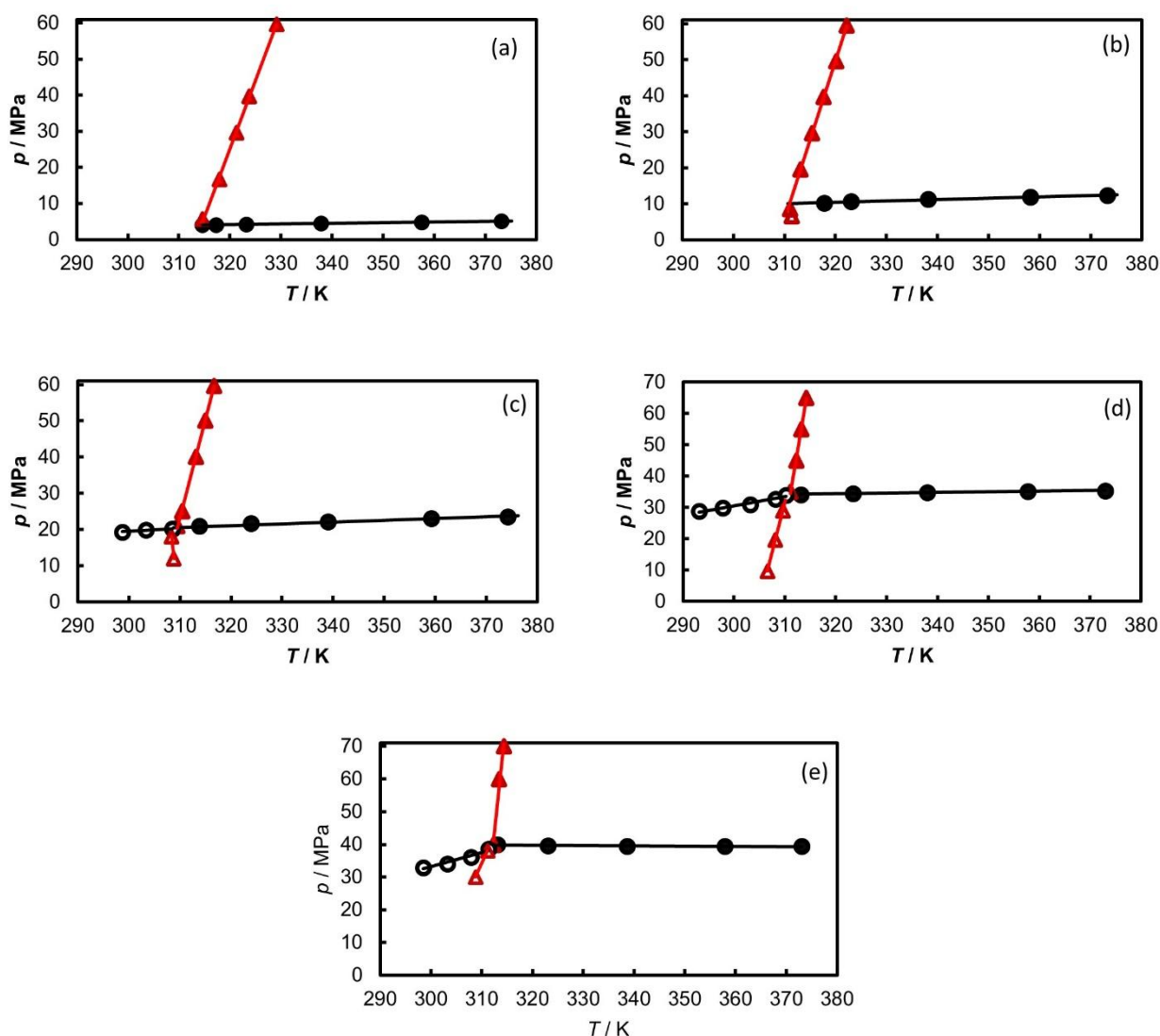
Figure 51. Observed phase transitions in the *p-T* diagram for different global mole compositions of HGM injected in the TLM; (a) z_{HGM} = 19.98 mol%, (b) z_{HGM} = 40.00 mol%, (c) z_{HGM} = 59.81 mol%, (d) z_{HGM} = 74.93 mol%, and (e) z_{HGM} = 80.00 mol%; L → LV (full circle, ●), SL → SLV (empty circle, ○), SL → L (full triangle, ▲), and SLV → LV (empty triangle, △).

At temperatures lower than the melting temperature, the solids formed in bulk tend to make the sample in the high-pressure cell misty, making it challenging to observe vapor phase formation in such two-phase liquid-solid systems. However, even in these conditions, a bubble point pressure can be indirectly determined through the break in the *Y*-factor curve during fluid depletion. By plotting all the bubble point pressures measured above and below the melting conditions in Figure 51, it can be pointed out that the bubble curve presents a discontinuity in

its slope at the solid appearance condition, as in the case of a binary system. In contrast, the three-phase solid-liquid-vapor (SLV) equilibrium domain differs from that of a binary system in the *p-T* projection (Pauly; Coutinho; Daridon, 2010, 2012, 2007) as it is no longer monovariant, demonstrating the multicomponent character of the mixture. In this case, the three-phase SLV equilibrium domain corresponds to an area in the *p-T* phase diagram, bounded at high temperatures and low pressures by the SLV → LV to transition curve and by the LS → SLV transition curve at higher pressures and lower temperatures, respectively.

The experimental phase transitions measured for the second mixture (PsB2) are listed in Table 26 and illustrated in Figure 52. Forty-nine experimental data points were collected for the PsB2 mixture. No liquid-liquid immiscibility was observed for the PsB2 mixture across all global compositions investigated, even for the lowest temperature studied, which is below the critical carbon dioxide temperature. Adding carbon dioxide to the mixture lowers the temperature conditions required for forming solid *o*-terphenyl, so no solid-fluid transition was observed under the experimental conditions with this second system.

Table 26. Pressure *p* and temperature *T* conditions of the fluid-fluid transition measured at a given temperature *T* at five different global compositions $z_{Gas-1} \pm U(z_{gas})$ in mol% for PsB2.

T / K	p / MPa	transition	T / K	p / MPa	transition	T / K	p / MPa	transition
$z_{HGM-CO2} = 20.09 \pm 0.12$ mol%			$z_{HGM-CO2} = 40.14 \pm 0.10$ mol%			$z_{HGM-CO2} = 60.00 \pm 0.09$ mol%		
293.15	2.49	L → LV	293.15	6.39	L → LV	293.22	12.00	L → LV
298.15	2.61	L → LV	298.15	6.57	L → LV	298.55	12.82	L → LV
308.15	2.85	L → LV	308.15	7.28	L → LV	308.14	13.93	L → LV
318.15	3.11	L → LV	318.15	7.83	L → LV	318.15	15.04	L → LV
323.15	3.23	L → LV	323.15	8.06	L → LV	323.24	15.59	L → LV
338.15	3.56	L → LV	338.15	8.89	L → LV	337.68	16.79	L → LV
358.15	3.97	L → LV	358.15	9.86	L → LV	358.00	18.55	L → LV
373.15	4.27	L → LV	373.15	10.52	L → LV	373.13	19.69	L → LV
$z_{HGM-CO2} = 74.97 \pm 0.06$ mol%			$z_{HGM-CO2} = 79.98 \pm 0.04$ mol%			$z_{HGM-CO2} = 84.98 \pm 0.04$ mol%		
293.33	21.10	L → LV	294.61	24.60	L → LV	292.95	30.09	L → LV
298.24	21.66	L → LV	308.15	26.40	L → LV	308.09	31.36	L → LV
308.43	23.33	L → LV	322.87	28.58	L → LV	324.00	32.39	L → LV
318.29	24.53	L → LV	337.72	30.06	L → LV	337.42	33.56	L → LV
323.15	25.10	L → LV	357.32	31.77	L → LV	356.85	34.91	L → LV
338.15	26.27	L → LV	372.70	32.81	L → LV	372.81	35.80	L → LV
357.88	28.04	L → LV						
373.15	29.21	L → LV						
$z_{HGM-CO2} = 87.00 \pm 0.03$ mol%								

309.30	32.57	L → LV
323.82	33.42	L → LV
337.72	34.41	L → LV
357.57	35.67	L → LV
372.13	36.49	L → LV

*Standard uncertainty u is $u(T) = 0.1$ K and $u(p) = 0.02$ MPa; Expanded uncertainty $U(p)_{L \to LV} = 0.06$ MPa.
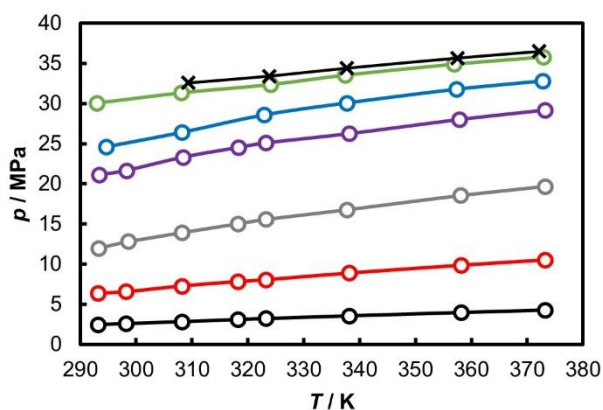
Figure 52. Observed L → LV phase transitions in the *p-T* diagram for different global mole compositions of HGM-CO_2 injected in the TLM. 20.09 mol% (black circle, ○), 40.14 mol% (red circle, ○), 60.00 mol% (gray circle, ○), 74.97 mol% (purple circle, ○), 79.98 mol% (blue circle, ○), 84.99 mol% (green circle, ○), and 86.92 mol% (black cross, x).

By comparing experiments carried out in PsB1 and PsB2, it can be noted that CO_2 addition in the PsB2 gas mixture significantly decreases the bubble point pressure compared with the PsB1 mixture in the same global mole composition. This decrease in the transition pressure makes it possible to study global molar compositions higher than those studied for the PsB1 system, for instance, a mixture with a global composition near 87 mol % HGM-CO_2. Additionally, no significant variation was observed in the bubble point measurement for the system with 86.92 mol% compared to the system with 84.98 mol% HGM-CO_2, suggesting that the mixture is close to the critical point at this gas content. This conclusion is further supported by experiments showing a long equilibration time for phase segregation just below the transition, allowing the observation of an interface between phases in equilibrium.

6.3.2 Thermodynamic modeling results

By comparing the melting temperature predicted at atmospheric pressure for the ternary liquid mixture to the experimental value, it was observed that the model underestimates the melting temperature of this system by around 10 K. Since no simplifying assumptions were made in the expression of Δg_{ot}^{SL} and the influence of temperature on the heat capacity was considered to obtain the solid fugacity at atmospheric pressure (eq. 5.4),the difference between the calculation of the melting temperature and the experiment only arises from the calculation of the fugacity of o-terphenyl in the liquid mixture. Generally, the binary interaction parameters are adjusted using vapor-liquid equilibrium data which influence the fluid phase isofugacity and, consequently, the ratio of fugacities f_i^L/f_i^V rather than the fugacity itself. As a result, achieving a good fit for fluid phase equilibria or employing predictive methods like PPR78, which is developed from VLE data, does not necessarily ensure an accurate representation of fugacities or other thermophysical properties when using a cubic equation of state. This understanding has led to the development of volume translation methods, which decouple liquid-vapor equilibrium optimization from volumetric property estimations (Jaubert et al., 2016; Péneloux; Rauzy; Fréze, 1982; Privat; Jaubert; Le Guennec, 2016). In liquid-solid equilibria, accurately predicting the liquid and vapor fugacities ratio is insufficient. Similarly, optimizing binary interaction parameters based on fluid phase equilibria measurements or using binary interaction parameter correlations derived from VLE data is often insufficient for accurately predicting liquid-solid equilibria. These insights highlight the limitations of relying solely on VLE data for parameter optimization of cubic equations of state and underscore the importance of incorporating additional data and methods to improve the accuracy of thermophysical property predictions. Using distinct models for the fluid and solid phases necessitates a reliable representation of the fugacities for each phase in equilibrium. Measuring the solid-fluid equilibrium conditions at atmospheric pressure allows for a precise determination of the fugacity of the precipitating compound using equilibrium eq. 5.3. This equation can be rewritten to incorporate the activity coefficient γ_{ot}^L of the o-terphenyl in the liquid phase:

$$f_{ot}^{*,S}(T,p_0) = \gamma_{ot}^L(T,p_0)\, x_{ot}^L\, f_{ot}^{*,L}(T,p_0) \tag{5.10}$$

Consequently, by measuring the temperature at which the solid disappears $T^{LS \rightarrow L}$ in the mixture formed by the three heavy components, it is possible to accurately determine the activity coefficient of o-terphenyl in this liquid mixture. Under these conditions, the composition of the liquid phase x_i^L becomes similar to the known global composition z_i^L of the ternary mixture and the activity coefficient can be calculated using the following relation:

$$\gamma_{ot}^{L,exp} = \frac{1}{z_{ot}^L} exp\left\{-\frac{\Delta h^m}{RTT^m}\Delta T + \frac{a_0^L-a_0^S}{RT}\left[\Delta T - T^{LS \rightarrow L}\ln\left(\frac{T^m}{T^{LS \rightarrow L}}\right)\right] + \frac{a_1^L-a_1^S}{2RT}(\Delta T)^2\right\} \quad (5.11)$$

where all the quantities come from experiments or literature data, as given in Table 23.

The activity of o-terphenyl obtained by this relation is $\gamma_{ot}^{L,exp} = 2.06$, whereas that calculated by the equation of state using Peng-Robinson equation of state with PPR78 mixing rule $\gamma_{ot}^{L,EOS} = 1.69$. This difference underestimates the temperature at which the o-terphenyl solid disappears. To correct this drawback, the binary interaction parameters (k_{ij}) between o-terphenyl and the two other heavy components were modified by multiplying by a correction factor α according to

$$k_{i,ot} = \alpha k_{i,ot}^{PPR78} \quad (5.12)$$

where i stands for 2,2,4,4,6,8,8 heptamethylnonane and dodecylcyclohexane. The correction parameter α was found to be 0.65 to ensure that $\gamma_{ot}^{L,EOS} = \gamma_{ot}^{L,exp}$. The others k_{ij}, particularly those involving light components and o-terphenyl, were kept unchanged to remain consistent with the PPR78 mixing rule developed to model fluid phase equilibria but not solid-liquid equilibria. The $k_{i,ot}$ modification between o-terphenyl and heavy components has an imperceptible effect on fluid phase equilibria but significantly influences predicted melting conditions. From this correction, the influence of adding gas on solid formation conditions of o-terphenyl in the multi-component system could be modelled. The results of the fluid-fluid and solid-fluid phase transition predicted for PsB1 are shown in Figure 53.

For the PsB1 mixture, a good agreement can be observed between the boundaries predicted for the L → LV and SL → L transitions and the experimental data, especially up to a global mole composition of 59.81 mol% HGM. However, for the mixtures with 74.93 mol% and 80.00 mol% HGM, the equation of state starts to predict an LLE formed by a liquid phase with a composition close to the global mixture composition ($z_i \approx x_i$) and a second phase predominantly composed of o-terphenyl ($x_{o-terphenyl} \approx 50$ mol%), which it is extending until temperature conditions equal to $T = 323.15$ K. A good description of the solid disappearance temperature is observed when comparing the modelled values with the experimental data, demonstrating the significant importance of the approach used for the binary interaction coefficient in modeling this system. It is important to note that apart from tuning α to the unique solid-liquid transition data at atmospheric pressure, the model is entirely predictive, and no experimental fluid phase equilibrium data fitting was performed. This result demonstrates the significant capability of the PPR78 mixing rule, which is highly effective in representing multicomponent systems for which no data are available for related binary systems.
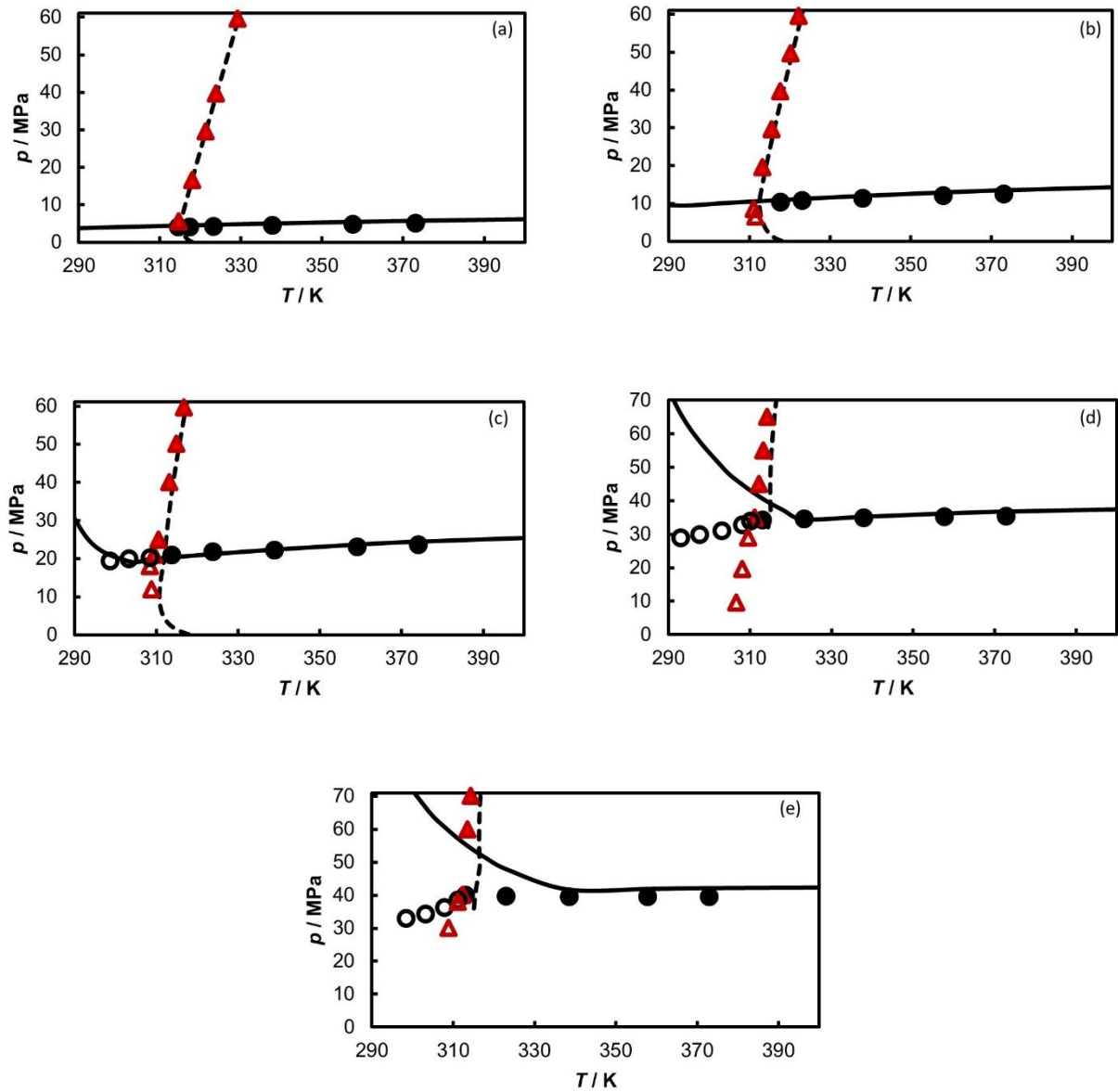
Figure 53. *p-T* phase diagram modeling for different global mole compositions of HGM injected in the TLM; (a) z_{HGM} = 19.98 mol%, (b) z_{HGM} = 40.00 mol%, (c) z_{HGM} =59.81 mol%, (d) z_{HGM} = 74.93 mol%, and (e) z_{HGM} = 80.00 mol%. Experimental data: L → LV (full circle, ●), SL → SLV (empty circle, ○), SL → L (full triangle, ▲), and SLV → LV (empty triangle, △); Fluid-fluid transition by PPR78 (continuous line, —) and solid-liquid transition by PPR78 (dashed line, - -).

The approach used for PsB1 was maintained for modeling the PsB2 mixture, and the predicted isopleths are shown in Figure 54. Similarly, a good agreement was achieved between the experimentally measured and predicted LV transitions for global mole compositions up to 60 mol% HGM-CO$_2$. For mixtures with 74.97 mol% HGM-CO$_2$ and beyond, the model presents an LL region at lower temperatures. Once again, the liquid-liquid phases formed are similar to those calculated for PsB1, with one liquid phase predominantly composed of o-terphenyl. This approach qualitatively agrees with the measured data for both liquid-vapor and solid-liquid transitions. Moreover, these results highlight the complexity of reproducing the experimentally observed phase transitions using classical models.
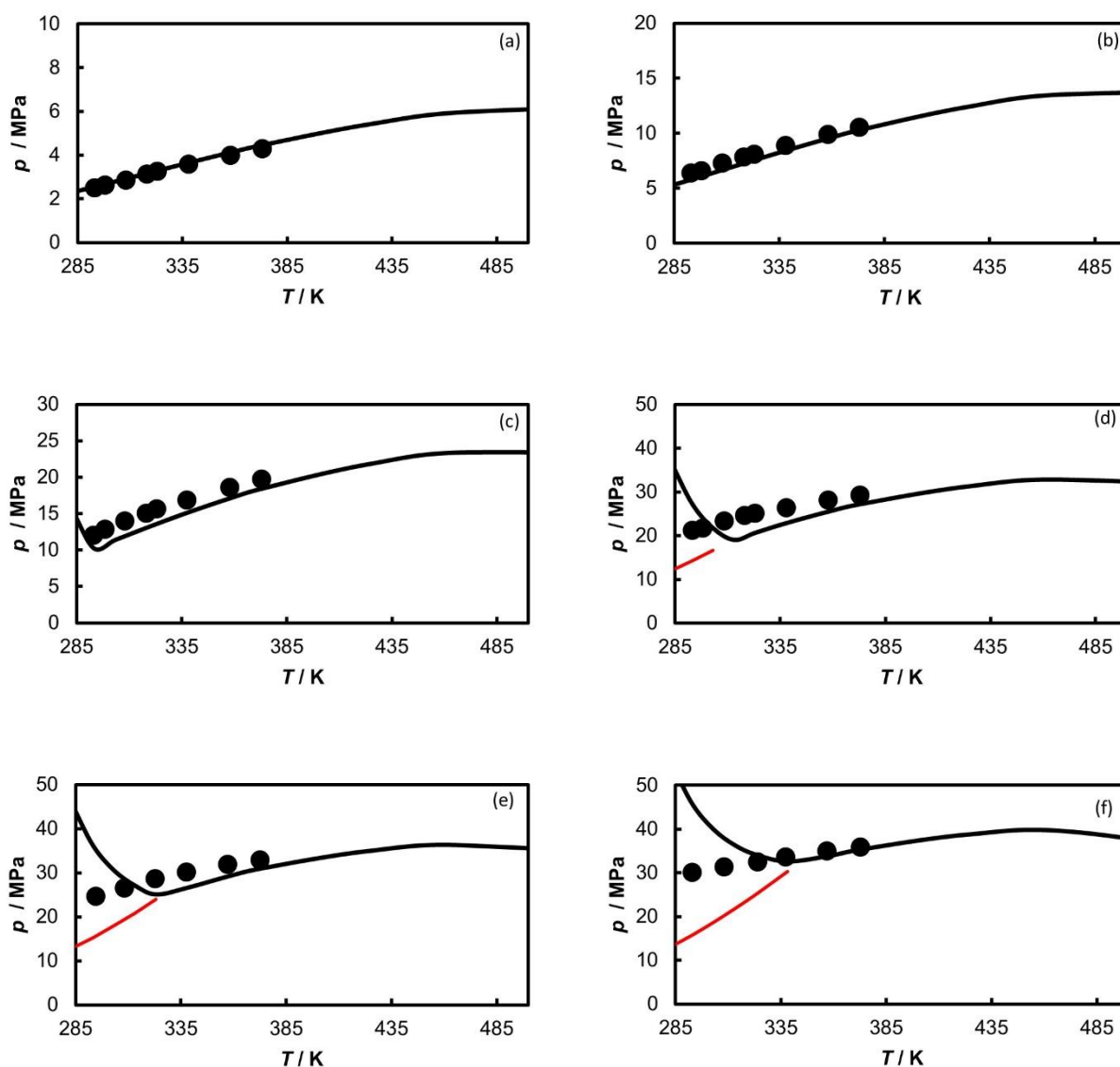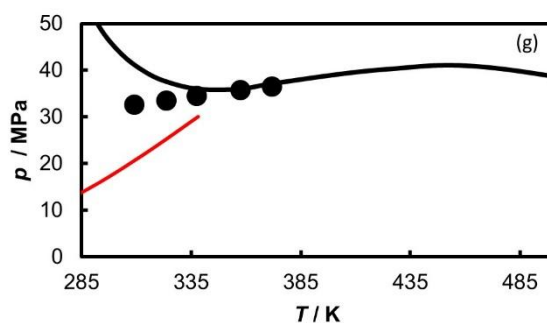
Figure 54. *p-T* phase diagram modeling for different global mole composition of HGM-CO_2 injected in the TLM; (a) z_{HGM} = 20.09 mol%, (b) z_{HGM} = 40.14 mol%, (c) z_{HGM} = 60.00 mol%, (d) z_{HGM} = 74.97 mol%, (e) z_{HGM} = 79.98 mol%; (f) z_{HGM} = 84.99 mol%, and (g) z_{HGM} = 86.92 mol%. Experimental liquid to liquid-vapor (black circles, ●), LVE by PPR78 (continuous black line, —), and LLVE by PPR75 (continuous red line, —).

Both synthetic systems experimentally investigated in this chapter cannot replicate the complex phase behavior observed in crude oil systems. However, these results do not necessarily disprove the hypothesis that the formation of a second liquid phase in reservoir fluids with high gas content is due to the separation of a heavy aromatic fraction. For instance, in the case of synthetic systems, the liquid composition strongly influences the appearance of a solid phase, which can overlap any potential LL loci. Moreover, the difficulty of reproducing such type of phase transition increases because there are no results in the literature reporting similar results for a dispersed liquid-liquid equilibrium for synthetic systems.

6.4   Conclusion

The primary aim of this chapter was to develop a mixture model system able to mimic the phase behavior of Brazilian pre-salt reservoir fluids experimentally observed in the last chapters, with a particular focus on capturing the occurrence of liquid-liquid phase separation at high temperatures, as observed in several studies. Despite the efforts of studying two multicomponent systems with and without carbon dioxide, attempts to mimic this behavior with the chosen model system were unsuccessful. This limitation underscores the complexity of Brazilian pre-salt oils.

The asphaltene fraction is a critical component of crude oils, particularly in Brazilian pre-salt reservoirs, where it significantly influences fluid phase behavior under high-temperature and high-pressure conditions. Due to their pivotal role in determining the thermodynamic properties of crude oils, developing synthetic model fluids that mimic the phase behavior of Brazilian pre-salt reservoir fluids appears challenging without including asphaltenes. Excluding asphaltenes would result in a model fluid that fails to capture key aspects of the real fluid's phase behavior, not only asphaltene deposition but also liquid-liquid phase separation. Therefore, future studies aiming to create representative synthetic model fluids for Brazilian reservoir fluids must incorporate asphaltenes. This inclusion is crucial to ensuring the model fluid accurately reflects the complex phase behavior and physicochemical properties observed in real-world conditions, enabling more reliable research, simulations, and decision-making in oil production and processing

On the other hand, the results obtained in this chapter revealed that the PPR78 model demonstrates considerable promise for predicting fluid phase equilibria in multicomponent systems. Notably, PPR78 has proven effective in modeling the phase behavior of synthetic mixtures with compositions approaching those of Brazilian pre-salt fluids. The insights gained from the application of PPR78 to represent correctly these model systems have significant implications. The ability of PPR78 to predict fluid phase equilibria with reasonable accuracy in systems that closely resemble Brazilian pre-salt fluids highlights its potential as a valuable tool for reservoir and flow assurance engineers.

7   GENERAL CONCLUSION

This Thesis aimed to study the fluid phase behavior of various Brazilian pre-salt crude oil samples under high-pressure and high-temperature conditions through recombination with pure gases or gas mixtures. The primary motivation for this study was the occurrence of complex phase transitions observed experimentally in this type of sample and the challenges posed by their high associated gas content, particularly carbon dioxide.

A liquid-liquid phase heterogeneity was experimentally detected in different Brazilian pre-salt crude oil samples under high-pressure and high-temperature conditions. Initially, it was speculated that this phase transition might be unique to certain fluids or induced by the high carbon dioxide content. However, liquid-liquid immiscibility was also observed when the crude oil samples investigated in Chapter IV were only mixed with methane. Moreover, this complex phase equilibrium exhibited similar qualitative characteristics across all samples investigated, including i) high dispersity without phase segregation, suggesting low interfacial tension and low-density contrast between phases; ii) occurrence when fluids reached a global gas mole composition above 70%; and iii) significant interaction with the asphaltenic phase.

The accurate delimitation of phase boundaries was only achievable by integrating and contrasting various analytical techniques, including light scattering, *p-V* curve analysis, *Y-factor* curve analysis, high-pressure microscopy, and a full-visibility cell. Specifically, a SWIR apparatus was essential for detecting dispersed liquid-liquid equilibrium in a high-pressure microscope or a full-visibility equilibrium cell. Furthermore, the combined results from these techniques indicate that this liquid-liquid equilibrium sometimes evolves into a liquid-liquid-vapor equilibrium. This last observation suggests that relying solely on conventional techniques could lead to misinterpretations regarding the accurate phase behavior of the samples.

By integrating all the experimental data obtained in this Thesis regarding crude oil samples, it was observed that the liquid-liquid equilibrium, whether in mixtures with carbon dioxide or methane, was associated with two main factors: i) a high gas content, indicating a high gas-oil ratio; and ii) significant system asymmetry due to the presence of low molecular weight gas molecules alongside the heavy hydrocarbon fraction, particularly asphaltenes. The thermodynamic modeling approach used in Chapter IV suggests that the formation of a second liquid phase is caused by the separation of a heavy hydrocarbon fraction resulting from the high

gas content added to the crude oil sample. Moreover, the results of both the experiments and the thermodynamic modeling reveal that both liquid phases in equilibrium at high temperature and high pressure exhibit a similar density.

This Thesis further highlighted the complexity of reservoir fluid studies by investigating a synthetic system. Only liquid-vapor, solid-liquid, and solid-liquid-vapor transitions were observed in this system. These findings underscore the intricate nature of studying the phase behavior of Brazilian pre-salt crude oil samples, making the reproduction of the liquid-liquid equilibrium in such systems challenging. Nevertheless, the valuable data obtained and the thermodynamic modeling approach applied to offer a promising framework for describing the phase behavior of multicomponent systems.

REFERENCES

ACEVEDO, Nelson *et al.* Understanding Asphaltene Fraction Behavior through Combined Quartz Crystal Resonator Sensor, FT-ICR MS, GPC ICP HR-MS, and AFM Characterization. Part I: Extrography Fractionations. Energy and Fuels, v. 34, n. 11, p. 13903–13915, 2020.

AGRAWAL, P. *et al.* Measurement and modeling of the phase behavior of solvent diluted bitumens. Fluid Phase Equilibria, v. 334, p. 51–64, nov. 2012.

AL GHAFRI, Saif Z.; MAITLAND, Geoffrey C.; TRUSLER, J. P. Martin. Experimental and modeling study of the phase behavior of synthetic crude oil+CO2. Fluid Phase Equilibria, v. 365, p. 20–40, mar. 2014.

ALBOUDWAREJ, H. *et al.* Sensitivity of Asphaltene Properties to Separation Techniques. Energy & Fuels, v. 16, n. 2, p. 462–469, 1 mar. 2002.

ALVES, Caiuã Araújo *et al.* Effect of Temperature on Asphaltenes Precipitation: Direct and Indirect Analyses and Phase Equilibrium Study. Energy & Fuels, v. 33, n. 8, p. 6921–6928, 15 ago. 2019.

AMANI, Mohammad J.; GRAY, Murray R.; SHAW, John M. Phase behavior of Athabasca bitumen+water mixtures at high temperature and pressure. The Journal of Supercritical Fluids, v. 77, p. 142–152, maio 2013.

ANDERSEN, Simon Ivar; BIRDI, Kulbir S. Aggregation of asphaltenes as determined by calorimetry. Journal of Colloid and Interface Science, v. 142, n. 2, p. 497–502, mar. 1991.

AQUINO-OLIVOS, A. *et al.* Investigations of Inhibition of Asphaltene Precipitation at High Pressure Using Bottomhole Samples. Energy & Fuels, v. 15, n. 1, p. 236–240, 1 jan. 2001.

ARAÚJO, C. B. K. *et al.* Phase behavior of Brazilian stock tank oil and carbon dioxide at reservoir conditions: experiments and thermodynamic modeling. Journal of Petroleum Exploration and Production Technology, v. 6, n. 1, p. 39–44, 7 mar. 2016.

BADAMCHI-ZADEH, A. *et al.* Phase Behaviour and Physical Property Measurements for VAPEX Solvents: Part I. Propane and Athabasca Bitumen. Journal of Canadian Petroleum Technology, v. 48, n. 01, p. 54–61, 1 jan. 2009a.

BADAMCHI-ZADEH, Amin *et al.* Phase Behaviour and Physical Property Measurements for VAPEX Solvents: Part II. Propane, Carbon Dioxide and Athabasca Bitumen. Journal of Canadian Petroleum Technology, v. 48, n. 03, p. 57–65, 1 mar. 2009b.

BENELLI, Federico E.; PISONI, Gerardo O.; CISMONDI-DUARTE, Martin. A classification of phase envelopes for reservoir fluids with asphaltene onset lines: Exploring topology transitions based on compositional changes. Fluid Phase Equilibria, v. 575, 1 dez. 2023.

BORGES, Gustavo R. *et al.* Near infrared spectroscopy applied for high-pressure phase behavior measurements. The Journal of Supercritical Fluids, v. 104, p. 221–226, set. 2015.

BRAGA, Arthur J. O.; TAVARES, Frederico W.; NDIAYE, Papa M. A new high-pressure cell for equilibrium measurements of systems with fluid and solid phases. The Journal of Supercritical Fluids, v. 179, n. September 2021, p. 105420, jan. 2022.

BROWN, T. S.; KIDNAY, A. J.; SLOAN, E. D. Vapor—liquid equilibria in the carbon dioxide-ethane system. Fluid Phase Equilibria, v. 40, n. 1–2, p. 169–184, out. 1988.

BRYANT, D. W.; MONGER, T. G. Multiple-Contact Phase Behavior Measurement and Application With Mixtures of CO2 and Highly Asphaltic Crude. SPE Reservoir Engineering, v. 3, n. 02, p. 701–710, 1 maio 1988.

CARDOSO, F. M. R. *et al.* CO 2 and Temperature Effects on the Asphaltene Phase Envelope As Determined by a Quartz Crystal Resonator. Energy & Fuels, v. 28, n. 11, p. 6780–6787, 20 nov. 2014.

CARDOSO, F. M. R. *et al.* Phase Behavior of CO2-Rich Live Oil Samples From High Pressure Reservoirs. *In:* OTC, 27 out. 2015. Rio de Janeiro, 2015, p. 431-442. Avaliable in : <https://onepetro.org/OTCBRASIL/proceedings/15OTCB/2-15OTCB/Rio de Janeiro, Brazil/77762> Access em: 27/05/2025

CARRIER, H. *et al.* Acoustic method for measuring asphaltene flocculation in crude oils. Journal of Petroleum Science and Engineering, v. 27, n. 3–4, p. 111–117, set. 2000.

CHANG, S. S.; BESTUL, A. B. Heat capacity and thermodynamic properties of o-terphenyl crystal, glass, and liquid. The Journal of Chemical Physics, v. 56, n. 1, p. 503–516, 1972.

CHEN, Li *et al.* Yen–Mullins Model Applies to Oilfield Reservoirs. Energy & Fuels, v. 34, n. 11, p. 14074–14093, 19 nov. 2020.

CHEN, Roger J. J.; CHAPPELEAR, Patsy S.; KOBAYASHI, Riki. Dew-point loci for methane-n-hexane and methane-n-heptane binary systems. Journal of Chemical & Engineering Data, v. 21, n. 2, p. 213–219, 1 abr. 1976.

CISMONDI, Martín *et al.* Phase Equilibria of CO 2 + n -Alkane Binary Systems in Wide Ranges of Conditions: Development of Predictive Correlations Based on Cubic Mixing Rules. Industrial & Engineering Chemistry Research, v. 51, n. 17, p. 6232–6250, 2 maio 2012.

COUTINHO, João A. P.; JØRGENSEN, Marianne; STENBY, Erling H. Predictions of three-phase regions in CO2-oil mixtures. Journal of Petroleum Science and Engineering, v. 12, n. 3, p. 201–208, jan. 1995.

CRUZ, Arley A. *et al.* CO2 influence on asphaltene precipitation. The Journal of Supercritical Fluids, v. 143, n. August 2018, p. 24–31, jan. 2019.

DA COSTA FRAGA, Carlos Tadeu *et al.* Brazilian Pre-Salt: An Impressive Journey from Plans and Challenges to Concrete Results. *In:* OTC, 4 maio 2015. Texas, 2015, p. 746-760. Avaliable in : <https://onepetro.org/OTCONF/proceedings/15OTC/All-15OTC/Houston, Texas, USA/77609> Access: 27/05/2025

DA SILVA, Vinicius M. *et al.* High pressure phase equilibria of carbon dioxide + n-alkanes mixtures: Experimental data and modeling. Fluid Phase Equilibria, v. 463, p. 114–120, 15 mai 2018.

DARIDON, J. L.; PAULY, J.; MILHET, M. High pressure solid–liquid phase equilibria in synthetic waxes. Phys. Chem. Chem. Phys., v. 4, n. 18, p. 4458–4461, 2002.

DARIDON, Jean Luc *et al.* Fluid-fluid and fluid-solid phase equilibria in carbon dioxide + waxy systems 1. CO2 + n-C17. Fluid Phase Equilibria, v. 538, p. 113023, 2021.

DARIDON, Jean Luc; ORLANDI, Ezequiel; CARRIER, Hervé. Measurement of bubble point pressure in crude oils using an acoustic wave sensor. Fluid Phase Equilibria, v. 427, p. 152–160, 2016.

DARIDON, Jean-Luc *et al.* Solid−Liquid−Vapor Phase Boundary of a North Sea Waxy Crude: Measurement and Modeling. Energy & Fuels, v. 15, n. 3, p. 730–735, 1 maio 2001.

DARIDON, Jean-Luc *et al.* Combined Investigations of Fluid Phase Equilibria and Fluid–Solid Phase Equilibria in Complex CO2–Crude Oil Systems under High Pressure. Journal of Chemical & Engineering Data, v. 65, n. 7, p. 3357–3372, 9 jul. 2020.

DARIDON, Jean-Luc; CARRIER, Hervé. Measurement of Phase Changes in Live Crude Oil Using an Acoustic Wave Sensor: Asphaltene Instability Envelope. Energy & Fuels, v. 31, n. 9, p. 9255–9267, 21 set. 2017.

DINI, Yoann; BECERRA, Mildred; SHAW, John M. Phase Behavior and Thermophysical Properties of Peace River Bitumen + Propane Mixtures from 303 K to 393 K. Journal of Chemical & Engineering Data, v. 61, n. 8, p. 2659–2668, 11 ago. 2016.

DOHRN, Ralf *et al.* High-pressure fluid-phase equilibria: Experimental methods, developments and systems investigated (2013–2016). Fluid Phase Equilibria, v. 579, n. September 2023, p. 113978, abr. 2024.

DURAN, J. A.; SCHOEGGL, F. F.; YARRANTON, H. W. Kinetics of asphaltene precipitation/aggregation from diluted crude oil. Fuel, v. 255, p. 115859, 1 nov. 2019.

EGHBALI, Sara; DEHGHANPOUR, Hassan. An Experimental and Modeling Study of Solvent-Bitumen Phase Behavior at Elevated Temperatures Using Cold Lake Bitumen. *In:* SPE, 9 out. 2017. San Antonio, 2015, p. 1-30. Avaliable in : <https://onepetro.org/SPEATCE/proceedings/17ATCE/3-17ATCE/San Antonio, Texas, USA/193271> Access: 27/05/2025

ENICK, R.; HOLDER, G. D.; MORSI, B. I. Critical and three phase behavior in the carbon dioxide/tridecane system. Fluid Phase Equilibria, v. 22, n. 2, p. 209–224, dez. 1985.

ESPINOZA MEJIA, Julia E.; LI, Xiaoli. Phase Behavior and Reversibility Mechanisms of Asphaltene Precipitation for High-Pressure High-Temperature CO 2 –Oil Systems. Industrial & Engineering Chemistry Research, v. 62, n. 8, p. 3747–3766, 1 mar. 2023.

ESTRERA, Susana S.; ARBUCKLE, Melanie M.; LUKS, Kraemer D. Solubility and partial miscibility of ethane in certain hydrocarbon liquids. Fluid Phase Equilibria, v. 35, n. 1–3, p. 291–307, set. 1987.

EYSSAUTIER, Joëlle; FROT, Didier; BARRÉ, Loïc. Structure and Dynamic Properties of Colloidal Asphaltene Aggregates. Langmuir, v. 28, n. 33, p. 11997–12004, 21 ago. 2012.

FALL, David J.; FALL, Jaimie L.; LUKS, Kraemer D. Liquid-liquid-vapor immiscibility limits in carbon dioxide + n-paraffin mixtures. Journal of Chemical & Engineering Data, v. 30, n. 1, p. 82–88, 1 jan. 1985.

FALL, David J.; LUKS, Kraemer D. Liquid-liquid-vapor phase equilibria of the binary system carbon dioxide + n-tridecane. Journal of Chemical & Engineering Data, v. 30, n. 3, p. 276–279, 1 jul. 1985.

FERREIRA, F. A. V. et al. Characterization, Pressure–Volume–Temperature Properties, and Phase Behavior of a Condensate Gas and Crude Oil. Energy & Fuels, v. 32, n. 4, p. 5643–5649, 19 abr. 2018.

FONSECA, José M. S.; DOHRN, Ralf; PEPER, Stephanie. High-pressure fluid-phase equilibria: Experimental methods and systems investigated (2005–2008). Fluid Phase Equilibria, v. 300, n. 1–2, p. 1–69, jan. 2011.

GONZALEZ, Doris L. et al. Modeling Study of CO2 -Induced Asphaltene Precipitation. Energy & Fuels, v. 22, n. 2, p. 757–762, 1 mar. 2008.

GOUAL, Lamia et al. On the formation and properties of asphaltene nanoaggregates and clusters by DC-conductivity and centrifugation. Fuel, v. 90, n. 7, p. 2480–2490, jul. 2011.

GUI, Xia et al. Measurement and Correlation of High Pressure Phase Equilibria for CO 2 + Alkanes and CO 2 + Crude Oil Systems. Journal of Chemical & Engineering Data, v. 62, n. 11, p. 3807–3822, 9 nov. 2017.

GUZMÁN, Roque et al. Methods for determining asphaltene stability in crude oils. Fuel, v. 188, p. 530–543, jan. 2017.

HAMMAMI, A. et al. Asphaltene Precipitation from Live Oils: An Experimental Investigation of Onset Conditions and Reversibility. Energy & Fuels, v. 14, n. 1, p. 14–18, 1 jan. 2000.

HOSEIN, R.; MAYRHOO, R.; MCCAIN, W. D. Determination of Bubble-Point and Dew-Point Pressure Without a Visual Cell. In: SPE, 9 jun. 2014. Trinidad, 2014, p. 9-11. Avaliable in : <https://onepetro.org/SPETTCE/proceedings/14TTCE/14TTCE/D021S007R004/220396> Access: 27/05/2025

HOTTOVY, John D.; KOHN, James P.; LUKS, Kraemer D. Partial miscibility behavior of the ternary systems methane-propane-n-octane, methane-n-butane-n-octane, and methane-carbon dioxide-n-octane. Journal of Chemical & Engineering Data, v. 27, n. 3, p. 298–302, 1 jul. 1982.

HOTTOVY, John D.; LUKS, Kraemer D.; KOHN, James P. Three-phase liquid-liquid-vapor equilibriums behavior of certain binary carbon dioxide-n-paraffin systems. Journal of Chemical & Engineering Data, v. 26, n. 3, p. 256–258, 1 jul. 1981.

HUIE, Nicholas C.; LUKS, Kraemer D.; KOHN, James P. Phase-equilibriums behavior of systems carbon dioxide-n-eicosane and carbon dioxide-n-decane-n-eicosane. Journal of Chemical & Engineering Data, v. 18, n. 3, p. 311–313, 1 jul. 1973.

IDEM, Raphael O.; IBRAHIM, Hussam H. Kinetics of CO2-induced asphaltene precipitation from various Saskatchewan crude oils during CO2 miscible flooding. Journal of Petroleum Science and Engineering, v. 35, n. 3–4, p. 233–246, ago. 2002.

IONIŢĂ, Mihaela *et al.* Phase behavior of carbon dioxide + 2,4-dimethylpentane binary system at high pressures. The Journal of Supercritical Fluids, v. 199, n. March, p. 105941, ago. 2023.

JAMALUDDIN, A. K. M. *et al.* Laboratory Techniques to Measure Thermodynamic Asphaltene Instability. Journal of Canadian Petroleum Technology, v. 41, n. 07, p. 44–52, 1 jul. 2002.

JAUBERT, Jean Noël *et al.* Reliability of the correlation allowing the kij to switch from an alpha function to another one in hydrogen-containing systems. Fluid Phase Equilibria, 2013.

JAUBERT, Jean Noël *et al.* Benchmark Database Containing Binary-System-High-Quality-Certified Data for Cross-Comparing Thermodynamic Models and Assessing Their Accuracy. Industrial and Engineering Chemistry Research, v. 59, n. 33, p. 14981–15027, 19 ago. 2020.

JAUBERT, Jean-Noël *et al.* Extension of the PPR78 model (predictive 1978, Peng–Robinson EOS with temperature dependent kij calculated through a group contribution method) to systems containing aromatic compounds. Fluid Phase Equilibria, v. 237, n. 1–2, p. 193–211, out. 2005.

JAUBERT, Jean-Noël *et al.* Note on the properties altered by application of a Péneloux–type volume translation to an equation of state. Fluid Phase Equilibria, v. 419, p. 88–95, 15 jul. 2016.

JAUBERT, Jean-Noël; MUTELET, Fabrice. VLE predictions with the Peng–Robinson equation of state and temperature dependent kij calculated through a group contribution method. Fluid Phase Equilibria, v. 224, n. 2, p. 285–304, out. 2004.

JAUBERT, Jean-Noël; PRIVAT, Romain. Relationship between the binary interaction parameters (kij) of the Peng–Robinson and those of the Soave–Redlich–Kwong equations of state: Application to the definition of the PR2SRK model. Fluid Phase Equilibria, v. 295, n. 1, p. 26–37, ago. 2010.

JAUBERT, Jean-Noël; PRIVAT, Romain; MUTELET, Fabrice. Predicting the phase equilibria of synthetic petroleum fluids with the PPR78 approach. AIChE Journal, v. 56, n. 12, p. 3225–3235, 11 dez. 2010.

JOBACK, K. G.; REID, R. C. Estimation of Pure-Component Properties from Group-Contributions. Chemical Engineering Communications, v. 57, n. 1–6, p. 233–243, 21 jul. 1987.

JOHNSTON A, Kimberly Adriane. Measurement and Modeling of Pentane-Diluted Bitumen Phase Behaviour. 2017. Thesis (Doctoral in Chemical and Petroleum Engineering) Chemical and Petroleum Engineering Department, University of Calgary, Calgary, 2017.

JOHNSTON, K. A. *et al.* Phase behavior of bitumen and n-pentane. Fluid Phase Equilibria, v. 442, p. 1–19, jun. 2017.

JUYAL, Priyanka *et al.* Study of Live Oil Wax Precipitation with High-Pressure Micro-Differential Scanning Calorimetry. Energy & Fuels, v. 25, n. 2, p. 568–572, 17 fev. 2011.

KABIR, C. Shah; JAMALUDDIN, A. K. M. Asphaltene Characterization and Mitigation in South Kuwait's Marrat Reservoir. SPE Production & Facilities, v. 17, n. 04, p. 251–258, 1 nov. 2002.

KESLER, MG; LEE, BI. IMPROVE PREDICTION OF ENTHALPY OF FRACTIONS. HYDROCARBON PROCESSG, v. 55, p. 153–158, 1976.

KEYVANI, Fatemeh; QAJAR, Jafar; AMANI, Mohammad Javad. Assessment of the applicability of binary mixture hypothesis to modeling the phase behavior of heavy oil/bitumen-solvent systems for EOR applications. Fluid Phase Equilibria, v. 566, n. November 2022, p. 113689, mar. 2023.

KHAN, S. A.; POPE, G. A.; SEPEHRNOORI, Kamy. Fluid Characterization of Three-Phase CO2/Oil Mixtures. *In:* Society of Petroleum Engineers, abr. 1992. Avaliable in : <http://www.spe.org/elibrary/servlet/spepreview?id=00024130> Access: 27/05/2025

KHARRAT, Abdel M. *et al.* Issues with comparing SARA methodologies. Energy and Fuels, v. 21, n. 6, p. 3618–3621, nov. 2007.

KOHN, J. P.; KIM, Yang Joo; PAN, Yi Chuan. Partial Miscibility Phenomena in Binary Hydrocarbon Systems Involving Ethane. Journal of Chemical & Engineering Data, v. 11, n. 3, p. 333–335, 1 jul. 1966.

KOKAL, S. L. *et al.* Measurement And Correlation Of Asphaltene Precipitation From Heavy Oils By Gas Injection. Journal of Canadian Petroleum Technology, v. 31, n. 04, 1 abr. 1992.

KOKAL, Sunil L.; SAYEGH, Selim G. Phase behavior and physical properties of CO2-saturated heavy oil and its constitutive fractions: Experimental data and correlations. Journal of Petroleum Science and Engineering, v. 9, n. 4, p. 289–302, jul. 1993.

KONTOGEORGIS, Georgios M. *et al.* Industrial requirements for thermodynamic and transport properties: 2020. Industrial and Engineering Chemistry Research, v. 60, n. 13, p. 4987–5013, 7 abr. 2021.

KORDIKOWSKI, Andreas; SCHNEIDER, Gerhard M. Fluid phase equilibria of binary and ternary mixtures of supercritical carbon dioxide with low-volatility organic substances up to 100 MPa and 393 K: c. Fluid Phase Equilibria, v. 90, n. 1, p. 149–162, set. 1993.

KUKARNI, Ajit A. *et al.* Phase-equilbriums behavior of system carbon dioxide-n-decane at low temperatures. Journal of Chemical & Engineering Data, v. 19, n. 1, p. 92–94, 1 jan. 1974.

KUMAR, Rajeev; VOOLAPALLI, Ravi Kumar; UPADHYAYULA, Sreedevi. Prediction of crude oil blends compatibility and blend optimization for increasing heavy oil processing. Fuel Processing Technology, v. 177, p. 309–327, ago. 2018.

LARSON, L. L. *et al.* Temperature Dependence of L1/L2/V Behavior in CO2/Hydrocarbon Systems. SPE Reservoir Engineering, v. 4, n. 01, p. 105–114, 1 fev. 1989.

LEE, Byung Ik; KESLER, Michael G. A generalized thermodynamic correlation based on three-parameter corresponding states. AIChE Journal, v. 21, n. 3, p. 510–527, maio 1975.

LEI, Hao *et al.* Experimental Investigation and Application of the Asphaltene Precipitation Envelope. Energy & Fuels, v. 29, n. 11, p. 6920–6927, 19 nov. 2015.

LI, Chuanxian *et al.* Effect of Asphaltene Polarity on Wax Precipitation and Deposition Characteristics of Waxy Oils. Energy & Fuels, v. 33, n. 8, p. 7225–7233, 15 ago. 2019.

LI, Ying-Hsiao; DILLARD, Kenneth H.; ROBINSON, Robert L. Vapor-liquid phase equilibrium for carbon dioxide-n-hexane at 40, 80, and 120 .degree.C. Journal of Chemical & Engineering Data, v. 26, n. 1, p. 53–55, 1 jan. 1981.

LIN, Yueh-Neu; HWANG, Shuen-Cheng; KOBAYASHI, Riki. Vapor-liquid equilibrium of the methane-toluene system at low temperatures. Journal of Chemical & Engineering Data, v. 23, n. 3, p. 231–234, 1 jul. 1978.

LINDELOFF, Niels *et al.* Investigation of Miscibility Behavior of CO2 rich Hydrocarbon Systems – With Application for Gas Injection EOR. *In:* SPE, 30 set. 2013. Louisiana, 2013, p. 2330-2343. Avaliable in : <https://onepetro.org/SPEATCE/proceedings/13ATCE/2-13ATCE/New Orleans, Louisiana, USA/172580> Access: 27/05/2025

LINSTROM, P. J.; MALLARD, W. G. NIST Chemistry WebBook, NIST Standard Reference Database. Gaithersburg MD: 2021.

MA, Mingxu; CHEN, Shengnan; ABEDI, Jalal. Predicting the multiphase equilibrium and density of bitumen with C2H6, C3H8 and CO2 using the simplified PC-SAFT Equation of State. Fuel, v. 181, p. 652–659, out. 2016.

MANCILLA-POLANCO, Adel *et al.* Phase Behavior of Heavy-Oil/Propane Mixtures. SPE Journal, v. 24, n. 02, p. 596–617, 11 abr. 2019.

MICHELSEN, Michael L. The isothermal flash problem. Part I. Stability. Fluid Phase Equilibria, v. 9, n. 1, p. 1–19, dez. 1982a.

MICHELSEN, Michael L. The isothermal flash problem. Part II. Phase-split calculation. Fluid Phase Equilibria, v. 9, n. 1, p. 21–40, dez. 1982b.

MMATA, Bella; ONYEKONWU, Mike. Measurement of the wax appearance temperature of a gas condensate using high pressure microscopy technique. *In:* SPE, 6 Aug. 2018. Lagos, 2018, p. SPE-193459-MS. Avaliable *In:* <https://onepetro.org/SPENAIC/proceedings-abstract/18NAIC/18NAIC/SPE-193459-MS/215722>

MOHAMMADI, Saber *et al.* Reversibility of Asphaltene Aggregation in Live Oils: Qualitative and Quantitative Evaluation. Journal of Chemical & Engineering Data, v. 60, n. 9, p. 2646–2654, 10 set. 2015.

NAOKI, Motosuke; KOEDA, Susumu. Pressure-volume-temperature relations of liquid, crystal, and glass of o-terphenyl: excess amorphous entropies, and factors determining molecular mobility. The Journal of Physical Chemistry, v. 93, n. 2, p. 948–955, 1 jan. 1989.

OKUNO, R.; XU, Z. Mass Transfer on Multiphase Transitions in Low-Temperature Carbon-Dioxide Floods. SPE Journal, v. 19, n. 06, p. 1005–1023, 17 dez. 2014.

ORR, F. M.; JENSEN, C. M. Interpretation of Pressure-Composition Phase Diagrams for CO2/Crude-Oil Systems. Society of Petroleum Engineers Journal, v. 24, n. 05, p. 485–497, 1 out. 1984.

ORR, F. M.; YU, A. D.; LIEN, C. L. Phase Behavior of CO2 and Crude Oil in Low-Temperature Reservoirs. Society of Petroleum Engineers Journal, v. 21, n. 04, p. 480–492, 1 ago. 1981.

PAIVA, Felipe L. *et al.* Wax Precipitation Temperature Measurements Revisited: The Role of the Degree of Sample Confinement. Energy & Fuels, v. 31, n. 7, p. 6862–6875, 20 jul. 2017.

PASO, K.; KALLEVIK, H.; SJÖBLOM, J. Measurement of Wax Appearance Temperature Using Near-Infrared (NIR) Scattering. Energy & Fuels, v. 23, n. 10, p. 4988–4994, 15 out. 2009.

PASSADE-BOUPAT, Nicolas *et al.* Could the Asphaltene Solubility Class Index Be Used as the "Wax Appearance Temperature" of Asphaltenes? Illustration through the Study of the Polydispersity of PetroPhase 2017 Asphaltenes. Energy & Fuels, v. 32, n. 3, p. 2760–2768, 15 mar. 2018.

PAULY, Jérôme *et al.* Prediction of solid-fluid phase diagrams of light gases-heavy paraffin systems up to 200 MPa using an equation of state-G(E) model. Fluid Phase Equilibria, v. 167, n. 2, p. 145–159, 2000.

PAULY, Jérôme; COUTINHO, João A. P.; DARIDON, Jean-Luc. High pressure phase equilibria in methane+waxy systems. 2. Methane+waxy ternary mixture. Fluid Phase Equilibria, v. 297, n. 1, p. 149–153, out. 2010.

PAULY, Jérôme; COUTINHO, João A. P.; DARIDON, Jean-Luc. High pressure phase equilibria in methane+waxy systems. 3. Methane+a synthetic distribution of paraffin ranging from n-C13 to n-C22. Fluid Phase Equilibria, v. 313, p. 32–37, jan. 2012.

PAULY, Jérôme; COUTINHO, Joao; DARIDON, Jean-Luc. High pressure phase equilibria in methane+waxy systems. Fluid Phase Equilibria, v. 255, n. 2, p. 193–199, jul. 2007.

PEDERSEN, Karen Schou; CHRISTENSEN, Peter L.; SHAIKH, Jawad Azeem. Phase Behavior of Petroleum Reservoir Fluids, 2015.

PÉNELOUX, André; RAUZY, Evelyne; FRÉZE, Richard. A consistent correction for Redlich-Kwong-Soave volumes. Fluid Phase Equilibria, v. 8, n. 1, p. 7–23, jan. 1982.

PENG, Ding Yu; ROBINSON, Donald B. A New Two-Constant Equation of State. Industrial and Engineering Chemistry Fundamentals, v. 15, n. 1, p. 59–64, 1976.

PEPER, Stephanie; FONSECA, José M. S.; DOHRN, Ralf. High-pressure fluid-phase equilibria: Trends, recent developments, and systems investigated (2009–2012). Fluid Phase Equilibria, v. 484, p. 126–224, abr. 2019.

PEREZ CLARO, Y. A. *et al.* Phase Behavior of Mixtures of Bitumen and n-Butane. Energy and Fuels, v. 33, n. 9, p. 8530–8543, 2019.

PETERS, C. J. *et al.* The search for tricriticality in binary mixtures of near-critical propane and normal paraffins. Fluid Phase Equilibria, v. 51, n. C, p. 339–351, nov. 1989.

PETERS, C. J.; DE ROO, J. L.; DE SWAAN ARONS, J. Phase equilibria in binary mixtures of propane and hexacontane. Fluid Phase Equilibria, v. 85, n. 1, p. 301–312, maio 1993.

PETERS, C. J.; DE ROO, J. L.; LICHTENTHALER, R. N. Measurements and calculations of phase equilibria in binary mixtures of ethane + eicosane. Fluid Phase Equilibria, v. 69, p. 51–66, dez. 1991.

POETTMANN, Fred H.; KATZ, D. L. Phase Behavior of Binary Carbon Dioxide-Paraffin Systems. Industrial & Engineering Chemistry, v. 37, n. 9, p. 847–853, 1 set. 1945.

PRAUSNITZ, John M.; LICHTENHALER, Rudiger N.; DE AZEVEDO, Edmundo Gomes. Molecular Thermodynamics of Fluid-Phase Equilibria. 3. ed. New Jersey: Pearson Education, 1999.

PRESTON, G. T.; FUNK, E. W.; PRAUSNITZ, J. M. Solubilities of hydrocarbons and carbon dioxide in liquid methane and in liquid argon. The Journal of Physical Chemistry, v. 75, n. 15, p. 2345–2352, 1 jul. 1971.

PRIVAT, Romain; JAUBERT, Jean-Noël; LE GUENNEC, Yohann. Incorporation of a volume translation in an equation of state for fluid mixtures: which combining rule? which effect on properties of mixing? Fluid Phase Equilibria, v. 427, p. 414–420, 15 nov. 2016.

QUINZIO, M. J. *et al.* Solid-fluid phase behaviour in binary mixtures: A new classification focused on paraffinic systems. Fluid Phase Equilibria, v. 573, p. 113867, 1 out. 2023.

REGUEIRA, Teresa *et al.* High pressure phase equilibrium of ternary and multicomponent alkane mixtures in the temperature range from (283 to 473) K. Fluid Phase Equilibria, v. 449, p. 186–196, 15 out. 2017.

RIAZI, Mohammad R.; DAUBERT, Thomas E. Characterization parameters for petroleum fractions. Industrial & Engineering Chemistry Research, v. 26, n. 4, p. 755–759, 1 abr. 1987.

ROBINSON, Donald B.; PENG, Ding-Yu. The characterization of the heptanes and heavier fractions for the GPA Peng-Robinson programs. Tulsa: Research Report (Gas Processors Association), 1978.

RODRIGUEZ-REARTES, S. B. *et al.* High-pressure phase equilibria of systems carbon dioxide + n-eicosane and propane + n-eicosane. The Journal of Supercritical Fluids, v. 50, p. 193–202, 2009.

ROMERO YANES, Jose F. *et al.* Study of Liquid–Liquid and Liquid–Liquid–Vapor Equilibria for Crude Oil Mixtures with Carbon Dioxide and Methane Using Short-Wave Infrared Imaging: Experimental and Thermodynamic Modeling. Energy & Fuels, v. 34, n. 11, p. 14109–14123, 19 nov. 2020a.

ROMERO YANES, José F. *et al.* Experimental phase behavior and solubility parameter for crude oil + methane [T = 311.15–373.15 K] and crude oil + methane + CO2 mixtures [T = 343.15–383.15 K]. Fuel, v. 288, n. October, p. 119675, mar. 2021a.

ROMERO YANES, Jose F. *et al.* Phase Behavior Investigation of a Live Presalt Crude Oil from Short-Wave Infrared Observation, Acoustic Wave Sensing, and Equation of State Modeling. Energy & Fuels, v. 35, n. 22, p. 18504–18517, 18 nov. 2021b.

ROMERO YANES, José Francisco *et al.* Paraffin effects on the stability and precipitation of crude oil asphaltenes: Experimental onset determination and phase behavior approach. Fluid Phase Equilibria, v. 474, p. 116–125, out. 2018.

ROMERO YANES, José Francisco *et al.* Experimental study of the phase behavior of methane and crude oil mixtures. Fuel, v. 255, p. 115850, nov. 2019a.

ROMERO YANES, José Francisco *et al.* Experimental study of the phase behavior of methane and crude oil mixtures. Fuel, v. 255, n. July, p. 115850, nov. 2019b.

ROMERO YANES, José Francisco *et al.* Phase Behavior for Crude Oil and Methane Mixtures: Crude Oil Property Comparison. Energy & Fuels, v. 34, n. 5, p. 5188–5195, 21 maio 2020b.

ROMERO YANES, José Francisco *et al.* Measurement of Fluid Phase Equilibria for High Gas Ratio Mixtures of Carbon Dioxide, Methane, and Brazilian Presalt Crude Oil. Journal of Chemical & Engineering Data, v. 66, n. 3, p. 1356–1366, 11 mar. 2021c.

SAIDOUN, Mohamed *et al.* Revisiting asphaltenes instability predictions by probing destabiliztion using a fully immersed quartz crystal resonator. Fuel, v. 251, p. 523–533, set. 2019.

SCHABRON, John F. *et al.* Waxphaltene Determinator Method for Automated Precipitation and Redissolution of Wax and Asphaltene Components. Energy & Fuels, v. 26, n. 4, p. 2256–2268, 19 abr. 2012.

SCHNEIDER, G. *et al.* Phasengleichgewichte und kritische Erscheinungen in binären Mischsystemen bis 1500 bar, CO2 mit n-Octan, n-Undecan, n-Tridecan und n-Hexadecan. Chemie Ingenieur Technik - CIT, v. 39, n. 11, p. 649–656, 24 jun. 1967.

SEBASTIAN, Herbert M. *et al.* Vapor-liquid equilibrium in binary mixtures of carbon dioxide + n-decane and carbon dioxide + n-hexadecane. Journal of Chemical & Engineering Data, v. 25, n. 2, p. 138–140, 1 abr. 1980.

SHADMAN, M. M. *et al.* The Effect of Inhibitors on Asphaltene Precipitation in Crude Oil Using the Viscometric Method. Energy Sources, Part A: Recovery, Utilization, and Environmental Effects, v. 34, n. 9, p. 827–838, 29 fev. 2012.

SHARIATI, A.; PETERS, C. J.; MOSHFEGHIAN, M. Bubble-Point Pressures of Some Selected Methane + Synthetic C 6+ Mixtures. Journal of Chemical & Engineering Data, v. 43, n. 2, p. 280–282, 1 mar. 1998a.

SHARIATI, Alireza; PETERS, Cor J.; MOSHFEGHIAN, Mahmood. Bubble Point Pressures of Some Selected Carbon Dioxide + Synthetic C 6+ Mixtures. Journal of Chemical & Engineering Data, v. 43, n. 5, p. 785–788, 1 set. 1998b.

SHAW, J. M.; BÉHAR, E. SLLV phase behavior and phase diagram transitions in asymmetric hydrocarbon fluids. Fluid Phase Equilibria, v. 209, n. 2, p. 185–206, jul. 2003.

SHELTON, J. L.; YARBOROUGH, L. Multiple Phase Behavior in Porous Media During CO2 or Rich-Gas Flooding. Journal of Petroleum Technology, v. 29, n. 09, p. 1171–1178, 1 set. 1977.

SIMONCELLI, Ana P. P. *et al.* Phase behavior of systems with high CO2 content: Experiments and thermodynamic modeling. Fluid Phase Equilibria, v. 515, p. 112574, jul. 2020.

SOAVE, Giorgio. Equilibrium constants from a modified Redlich-Kwong equation of state. Chemical Engineering Science, v. 27, n. 6, p. 1197–1203, jun. 1972.

SOEDARMO, Auzan A. *et al.* Microscopic Study of Wax Precipitation—Static Conditions. Energy & Fuels, v. 30, n. 2, p. acs.energyfuels.5b02653, 22 jan. 2016.

TUREK, Edward A.; METCALFE, Robert S.; FISHBACK, Robert E. Phase Behavior of Several CO2/West-Texas-Reservoir-Oil Systems. SPE Reservoir Engineering, v. 3, n. 02, p. 505–516, 1 maio 1988a.

TUREK, Edward A.; METCALFE, Robert S.; FISHBACK, Robert E. Phase Behavior of Several CO2/West-Texas-Reservoir-Oil Systems. SPE Reservoir Engineering, v. 3, n. 02, p. 505–516, 1 maio 1988b.

VERDIER, Sylvain *et al.* Study of Pressure and Temperature Effects on Asphaltene Stability in Presence of CO 2. Energy & Fuels, v. 20, n. 4, p. 1584–1590, jul. 2006.

VERDIER, Sylvain; DUONG, Diep; ANDERSEN, Simon I. Experimental Determination of Solubility Parameters of Oils as a Function of Pressure †. Energy & Fuels, v. 19, n. 4, p. 1225–1229, jul. 2005.

VITU, Stéphane *et al.* Bubble and Dew Points of Carbon Dioxide + a Five-Component Synthetic Mixture: Experimental Data and Modeling with the PPR78 Model. Journal of Chemical & Engineering Data, v. 52, n. 5, p. 1851–1855, 1 set. 2007.

VITU, Stéphane *et al.* Phase equilibria measurements of CO2+methyl cyclopentane and CO2+isopropyl cyclohexane binary mixtures at elevated pressures. The Journal of Supercritical Fluids, v. 44, n. 2, p. 155–163, mar. 2008a.

VITU, Stéphane *et al.* High-pressure phase behaviour of the binary system {CO2+cis-decalin} from (292.75 to 373.75)K. The Journal of Chemical Thermodynamics, v. 40, n. 9, p. 1358–1363, set. 2008b.

VITU, Stéphane *et al.* Experimental determination and modelling of high-pressure phase behavior for the binary system CO2 + cyclooctane. The Journal of Supercritical Fluids, v. 174, n. March, p. 105249, ago. 2021.

VITU, Stéphane; JAUBERT, Jean-Noël; MUTELET, Fabrice. Extension of the PPR78 model (Predictive 1978, Peng–Robinson EOS with temperature dependent kij calculated through a group contribution method) to systems containing naphtenic compounds. Fluid Phase Equilibria, v. 243, n. 1–2, p. 9–28, maio 2006.

WILLIAMS, John M. Why Y? *In:* SPE, 30 out. 2011. Denver, 2011, p. SPE 146394. Avaliable in : <https://onepetro.org/SPEATCE/proceedings/11ATCE/11ATCE/SPE-146394-MS/148460> Access: 27/05/2025.

YANES, J. F. Romero; MONTEL, F.; DARIDON, J. L. Fluid phase equilibria in asymmetric model systems. Part I: CO2+ diphenylmethane. The Journal of Supercritical Fluids, v. 186, n. March, p. 105585, jul. 2022a.

YANES, J. F. Romero; MONTEL, F.; DARIDON, J. L. Fluid phase equilibria in asymmetric model systems. Part II: CO2 + 2,2,4,4,6,8,8-heptamethylnonane. The Journal of Supercritical Fluids, v. 189, n. August, p. 105721, out. 2022b.

YONEBAYASHI, Hideharu *et al.* Determination of Asphaltene-Onset Pressure Using Multiple Techniques in Parallel. SPE Production & Operations, v. 33, n. 03, p. 486–497, 13 ago. 2018.

ZHANG, Yechun *et al.* Modeling the phase behaviour of bitumen/n-alkane systems with the cubic plus association (CPA) equation of state. Fluid Phase Equilibria, v. 486, p. 119–138, 1 maio 2019.

ZID, Sarra *et al.* Fluid phase equilibria for the CO2 + 2,3-dimethylbutane binary system from 291.9 K to 373.1 K. The Journal of Supercritical Fluids, v. 179, n. August 2021, p. 105387, jan. 2022a.

ZID, Sarra *et al.* High-Pressure Phase Equilibria Measurements of the Carbon Dioxide + Cycloheptane Binary System. Journal of Chemical & Engineering Data, v. 67, n. 1, p. 176–181, 13 jan. 2022b.

ZOU, Xiang-Yang; SHAW, John M. Dispersed Phases and Dispersed Phase Deposition Issues Arising in Asphaltene Rich Hydrocarbon Fluids. Petroleum Science and Technology, v. 22, n. 7–8, p. 759–771, 2 jan. 2004.

ZOU, Xiangyang; ZHANG, Xiaohui; SHAW, John M. Phase Behavior of Athabasca Vacuum Bottoms + n-Alkane Mixtures. SPE Production & Operations, v. 22, n. 02, p. 265–272, 19 maio 2007.

ZUO, Mingsheng *et al.* Effects of CO2 injection volume and formation of in-situ new phase on oil phase behavior during CO2 injection for enhanced oil recovery (EOR) in tight oil reservoirs. Chemical Engineering Journal, v. 452, n. October 2022, p. 139454, jan. 2023.

APPENDIX I: UNCERTAINTIES

This section of the Thesis presents the calculation procedure used to determine the uncertainty associated with mixture preparation and experimentally determined phase transitions.

Global mole composition uncertainty

The mixture preparation procedure used in all chapters of this Thesis consists of two steps: i) liquid injection (crude oil or pure hydrocarbon mixture) by vacuum suction, and ii) gas injection. However, the method used to precisely measure the amount of injected liquid and gas varies across chapters. Different approaches were implemented over the course of the Thesis to reduce uncertainty.

For Chapters I and II the mass crude oil injected was determined by using an analytical scale with resolution of 0.001 g, whereas the amount of gas injected into the PVT was determined by the volume displaced from a syringe pump resolution of 0.01 mL. The following equation was used to calculate combined global mole composition:

$$u_c\left(z_{gas}\right) = z_{gas}\left(1 - z_{gas}\right)\left(\frac{u^2(m_{gas})}{m_{gas}^2} + \frac{u^2(m_{oil})}{m_{oil}^2}\right) \tag{8.1}$$

In this procedure, expanded uncertainty regarding both mass of oil and gas introduced were estimated to be better than 0.01g.

For Chapters II and III, the same Equation 8.1 was applied. However, in these sections, the expanded uncertainty associated with the mass of the liquid (oil or TML) and gas (CO_2, CH_4, CO_2 + CH_4, and HGM) introduced into the equilibrium cell was estimated to be better than 0.01 g and 0.005 g, respectively. It is worth noting that, since density values are required to estimate the combined uncertainty of the global mixture composition, these values were obtained from the REFPROP software for given temperature and pressure conditions to

convert the injected volume into injected mass. To do so, a standard uncertainty of 0.5% was assumed for the density values.

Phase transition uncertainties

Uncertainties regarding phase transition experimentally measured in this Thesis are estimated by using the same equation, as follows:

$$u^2\left(p^{transition}\right) = u^2\left(p^{gauge}\right) + u^2\left(p^{repeatability}\right) + \left[\frac{dp^{transition}}{dT} \cdot u(T^{gauge})\right]^2 \tag{8.2}$$

Since different high-pressure measurement cells were used to carry out the experiments, different values regarding the standard uncertainty for the pressure transducers $u(p^{gauge})$ and the repeatability of the pressure transition measurement $u\left(p^{repeatability}\right)$ are used. However, these values differ slightly, and for Chapter I and II, $u(p^{gauge})$ and $u(p^{repeatability})$ were taken as 0.10 MPa and 0.20 MPa, respectively. In contrast, for Chapter III and IV, the values of $u(p^{gauge})$ and $u(p^{repeatability})$ were considered to be 0.02 MPa and 0.10 MPa, respectively. The derivative part of the equation 8.2 was determined by using a numerical derivative procedure by using the data experimentally measured. The equation 8.2 was used to estimate the expanded uncertainty for all fluid-fluid (liquid-vapor, liquid-liquid, and liquid-liquid-vapor) phase transition at a level confidence of 95% (k=2).

About Chapter IV, the standard uncertainty considered regarding the solid-liquid phase transition was $u(T^{repeatability}) = 0.2$ K and the temperature transducers $u(T^{gauge}) = 0.1$ K. Therefore, the following equation was used to estimate the expanded uncertainty for solid disappearance temperature:

$$u^2(T^{SL-L}) = u(T^{gauge}) + u^2\left(T^{repeatability}\right) + \left[\frac{dT^{SL-L}}{dp} \cdot u(p^{gauge})\right]^2 \tag{8.3}$$

Equation 8.3 was used to estimate used to estimate the expanded uncertainty for T^{SL-L} measurement at a level confidence of 95% (k=2).